Quantum critical matter: Casimir pairing, emergent orders and topological defects

Yaroslav Kharkov

Supervisor:

Prof. Oleg Sushkov

UNSW
AUSTRALIA

The thesis is submitted in fulfilment of the requirements for the degree of Doctor of Philosophy in Physics

28 August 2017

ORIGINALITY STATEMENT

‘I hereby declare that this submission is my own work and to the best of my knowledge it contains no materials previously published or written by another person, or substantial proportions of material which have been accepted for the award of any other degree or diploma at UNSW or any other educational institution, except where due acknowledgement is made in the thesis. Any contribution made to the research by others, with whom I have worked at UNSW or elsewhere, is explicitly acknowledged in the thesis. I also declare that the intellectual content of this thesis is the product of my own work, except to the extent that assistance from others in the project's design and conception or in style, presentation and linguistic expression is acknowledged.’

Signed …….....

Date …….....

THE UNIVERSITY OF NEW SOUTH WALES
Thesis/Dissertation Sheet

Surname or Family name: Kharkov

First name: Yaroslav

Other name/s:
PhD

Abbreviation for degree as given in the University calendar:

School: School of Physics

Faculty: Science

Title:
Quantum critical matter: Casimir pairing, emergent orders and topological defects

Abstract 350 words maximum: (PLEASE TYPE)

In this thesis we address a few problems on critical phenomena in two- and three dimensional quantum materials. Specifically we consider high temperature superconductors, dimerized quantum magnets and frustrated magnets.

First, motivated by the recent discovery of a magnetic quantum critical point in hole-doped cuprates, we study the influence of the criticality on the superconducting pairing. We consider a fermion-fermion interaction in a 2D system at a quantum critical point. We found a new physical mechanism of fermion pairing by quantum critical fluctuations, that is similar to a Casimir effect. The Casimir pairing mechanism has conceptual similarities with chiral bag models in quantum chromodynamics and is generic for a wide class of quantum phase transitions.

Second, we consider an impurity screening problem in a 3D magnet close to a quantum critical point. We show that a local magnetic moment of the impurity becomes screened by the cloud of critical magnons and we calculate the distribution of a magnetization in the cloud. Our results show that adding a small concentration of impurities can significantly affect critical properties of the system.

Next, we perform a phenomenological study of incommensurate charge density wave (CDW) in cuprates. Proceeding with a combined analysis of recent experimental data on the CDW, we find the amplitude and the spatial pattern of the CDW. From nuclear magnetic resonance data we extract the s, s' and d-wave amplitudes of the CDW and rule out the checkerboard pattern of the CDW. We show that data potentially rules out a wide class of theoretical models of the CDW.

Finally, we consider topological defects (skyrmions and merons) in frustrated magnets which are in the vicinity of a phase transition from a collinear to a spiral magnetic state.
We show that isolated metastable skyrmions can exist in the absence of an external magnetic field in frustrated magnets with an easy-axis/easy-plane anisotropy. We found exotic skyrmion states with a large topological charge: skyrmion rings and meron rings.
In the systems with easy-plane spin anisotropy we demonstrated that at the critical point a skyrmion with a unit topological charge ``fractionalizes'' into a pair of merons.

Declaration relating to disposition of project thesis/dissertation

I hereby grant to the University of New South Wales or its agents the right to archive and to make available my thesis or dissertation in whole or in part in the University libraries in all forms of media, now or here after known, subject to the provisions of the Copyright Act 1968. I retain all property rights, such as patent rights. I also retain the right to use in future works (such as articles or books) all or part of this thesis or dissertation.

I also authorise University Microfilms to use the 350 word abstract of my thesis in Dissertation Abstracts International (this is applicable to doctoral theses only).

…… …… ……

Signature Witness Signature Date

The University recognises that there may be exceptional circumstances requiring restrictions on copying or conditions on use. Requests for restriction for a period of up to 2 years must be made in writing. Requests for a longer period of restriction may be considered in exceptional circumstances and require the approval of the Dean of Graduate Research.

FOR OFFICE USE ONLY Date of completion of requirements for Award:

Abstract

In this thesis we address a few problems on critical phenomena in two- and three dimensional materials. Specifically we consider high temperature superconductors, dimerized quantum magnets and frustrated magnets.

Motivated by the recent discovery of a magnetic quantum critical point in hole-doped cuprates (at the doping $p \approx 0.1$), we study the influence of the criticality on the superconducting pairing. We consider fermion-fermion pairing in a two-dimensional system at quantum critical point. We found a new physical mechanism of fermion pairing by quantum critical fluctuations, that is similar to a Casimir effect. The Casimir pairing mechanism has conceptual similarities with chiral bag models in quantum chromodynamics and is generic for a wide class of quantum phase transitions.

Doping quantum critical system by impurities can significantly affect the "critical" properties of the system. We consider an impurity problem in a 3D magnet close to a quantum critical point, e.g. $TlCuCl_3$. By analogy with a Kondo effect in normal metals this problem is called "Bose-Kondo" problem. We show that local magnetic moment of the impurity becomes screened by the cloud of critical magnons. Moreover, we show that the screening can be interpreted as a "spin-charge separation" in a 3D quantum critical system. Interestingly, our results show that adding a small concentration of impurities can shift position of a QCP, that agrees with experimental data for doped 3D quantum magnets.

Among various types of emergent orders that exist in cuprates, a charge density wave (CDW) phase attracted a lot of attention over the last few years. Despite of a numerous experimental and theoretical work on the subject, some key information about CDW state is still missing. One of the main unanswered questions is

the amplitude and the spatial pattern of CDW. To resolve the questions in phenomenology of CDW, we perform a combined analysis of available experimental data: nuclear magnetic resonance (NMR), resonant inelastic X-ray scattering and hard X-ray diffraction. We extract from NMR data the s, s' and d-wave amplitudes of CDW and rule out the checkerboard pattern of CDW. We show that data potentially rules out a wide class of theoretical models of CDW.

Finally, we consider topological defects (skyrmions and merons) in frustrated magnets which are in the vicinity of a Lifshiz point separating collinear and spiral states. We show that isolated metastable skyrmions can exist in the absence of external magnetic field in frustrated magnets with an easy-axis/easy-plane anisotropy. We found exotic skyrmion states with large topological charge: skyrmion rings. In the systems with easy-plane spin anisotropy we demonstrated that at the critical point a skyrmion with a unit topological charge "fractionalizes" into a pair of merons - half-skyrmions.

Contents

Acknowledgments

First of all, I would like to thank my supervisor, Prof. Oleg Sushkov, for providing such interesting and fruitful projects for me to work on, and for the help, guidance, and support over my years at UNSW. I was always astonished by Oleg's physical intuition and his ability to get to the root of any problem. Furthermore, I express a huge gratitude to Oleg and his wife Tamara for their constant support and help outside of science.

I would like to thank my co-authors: Ivan Terekhov and Maxim Mostovoy. It was very instructive to work with them side by side, and I am grateful for the knowledge and experience they shared with myself.

I thank M. Vojta, B. Rosenow, F. Mila, J. Schmalian for inviting me to visit their research groups in Dresden Technical University, Leipzig University, École Polytechnique Fédérale de Lausanne, Karlsruhe Institute of Technology, as well as for their hospitality and the financial support during my visit in Europe. I would also to acknowledge the UNSW Graduate Research School for the financial support that allowed me to attend the conference "Spectroscopies in Novel Superconductors" in Stuttgart, Germany (2016). I also thank my supervisor O. Sushkov for providing funds for me, including attendance of Summer School VSSUP14 at Swinburne University, Melbourne, and Annual Condensed Matter Meetings (Weiheke Island, New Zealand and Wagga-Wagga, Australia). I thank A. Milstein, V. Kotov, A. Chubukov, G. Khaliullin, B. Normand, A. Macdonald for very insightful discussions during their visit to Sydney. I thank M.-H. Julien for providing us unpublished data, that were very important for our analysis.

I thank Harley Scammell for our exciting collaborative work as well as for project related discussions. Also I thank H. Scammell and Dima Miserev for the

physics/math problem solving sessions and brainstorms next to the blackboard. I thank our group members and other PhD students: T. Li, S. Bladwell, G. Vionnet, B. Lackenby, B. Roberts, A. Kozlov, Y. Stadnik for interesting physics and non-physics talks over a cup of coffee.

I want to express a special gratitude to Amy Geddes for the encouragement and her enormous emotional support on an uneasy track of a PhD life. Finally, I would like to thank my friends from Russia, my family for their always present support.

Units and notations

Except for where explicitly stated, we use the following units: $\hbar = k_B = 1$.
Abbreviations - The following abbreviations, which are also defined upon their first use in each Chapter, are used frequently throughout this thesis:

- **QPT/QCP** - Quantum phase transition / Quantum critical point,
- **2D/3D** - Two-dimensional / Three-dimensional,
- **NMR** - Nuclear magnetic resonance,
- **NQR** - Nuclear quadrupole resonance,
- **AFM/FM** - Antiferromagnet / Ferromagnet,
- **CDW** - Charge density wave,
- **SCBA** - Self-Consistent Born approximation,
- **RG** - Renormalization group,
- **SCS** - Spin - charge separation,
- **SkX** - Skyrmion crystal.
- **NLσ** - Nonlinear sigma model

Publications

Work from this thesis has been published in:

1. Y. A. Kharkov and O. P. Sushkov, *Casimir effect mechanism of pairing between fermions in the vicinity of a magnetic quantum critical point*, Phys. Rev. B **91**, 235105 (2015)

2. Y. A. Kharkov, I. S. Terekhov, and O. P. Sushkov, *Impurity-induced magnetization in a three-dimensional antiferromagnet at the quantum critical point*, Phys. Rev. B 92, 155122 (2015)

3. Y. A. Kharkov and O. P. Sushkov, *The amplitudes and the structure of the charge density wave in YBCO* , Scientific Reports **6**, 34551 (2016)

4. Y. A. Kharkov, O. P. Sushkov and M. Mostovoy, *Bound states of skyrmions and merons near the Lifshitz point*, arXiv:1703.09173, submitted to Phys. Rev. Lett.

The results from this thesis have been presented at several international conferences:

- Gordon Godfrey workshop *"Spins and Strong Electron Correlations"* (Sydney, Australia, 2013).
- Annual Condensed Matter Meeting (Weiheke Island, New Zealand, 2014).
- Gordon Godfrey workshop *"Spins and Strong Electron Correlations"* (Sydney, Australia, 2015).
- Annual Condensed Matter Meeting (Wagga Wagga, Australia, 2015).

- Annual Condensed Matter Meeting (Wagga Wagga, Australia, 2016).
- Conference *"Spectroscopies in Novel Superconductors"* (Stuttgart, Germany, 2016).

Chapter 1

Introduction

In this Chapter we outline the background information on studies of quantum critical phenomena in condensed matter systems. We provide a brief overview of high Tc superconductivity in cuprates, emergent magnetic and charge orders in quantum critical systems and topological spin excitations in classical critical systems.

1.1 What is a quantum phase transition?

Phase transitions and critical phenomena play a very important role in various branches of physics, from statistical physics and condensed matter physics to cosmology and particle physics. Numerous examples of critical phenomena include melting of ice into water, demagnetization of ferromagnetic iron above the Curie temperature, onset of superfluidity in ^4He below the lambda point $T_\lambda = 2.17$K, superconductivity in metals, baryongenesis in the early Universe and generation of quark-gluon plasma in collisions of heavy nuclei. These are examples of thermal phase transitions, that occur at a certain critical temperature T_c due to thermal fluctuations.

Recently a new class of phase transitions, so called quantum phase transitions, attracted a lot of attention in the context of condensed matter physics [1]. In contrast to thermodynamical phase transitions, the quantum phase transitions are driven by quantum fluctuations due to Heisenberg's uncertainty principle. Let us imagine a physical system at zero temperature, that is controlled by some external

parameter g. The parameter g can correspond to a hydrostatic pressure, magnetic field, chemical doping, etc. (but not temperature !) and it plays a role of a tuning "handle" for our system. Upon varying the parameter g at some particular value g_c a dramatic transformation of the system's ground state may occur. The phase transition across the critical point $g = g_c$ is called a "quantum phase transition" (QPT) and g_c is called a "quantum critical point"(QCP).

A QCP separates the two ground states at $g < g_c$ and $g > g_c$, that are referred as ordered and quantum disordered phases. The properties of the two phases are characterized by an order parameter similarly to the conventional thermodynamical phase transitions. While an order parameter vanishes in a disordered phase it takes non-zero values in the ordered phase. Hereafter we will consider only "continuous QPTs", where the order parameter is a continuous function of the tuning variable g.

An order parameter can be a scalar, vector or tensor or a group element of a symmetry group such as $SO(N)$, $SU(N)$ etc. The transformation properties of an order parameter are dictated by the symmetry group of the system's ground state. The order parameter symmetry group is crucial in determining the quantum critical behaviour of the system. The symmetry considerations are very powerful for analysis of critical phenomena, that allow to classify QPTs in generic universality classes. We will discuss the universality classes in more details later in the present Chapter.

Usually an order parameter is expressed as an expectation value of a local in space and time operator. Such order parameter $\phi(\boldsymbol{R}_i, t)$ ($\boldsymbol{R}_i$ are the coordinates of a crystal lattice sites) is associated with a local physical observable $\mathcal{O}(R_i, t)$, e.g. magnetization, charge density, superconducting gap etc. If the observable oscillates in space (as in the case of AFM ordering), the order parameter has to be defined as corresponding an envelope function

$$\langle \mathcal{O}(\boldsymbol{R}_i, t) \rangle = \mathrm{Re}\{\phi(\boldsymbol{R}_i, t) e^{i\boldsymbol{Q}\boldsymbol{R}_i}\}, \tag{1.1}$$

where $\boldsymbol{Q}$ is the ordering wave vector. We will assume that the order parameter is a slowly varying function of $\boldsymbol{R}_i$ and $\phi(\boldsymbol{R}_i)$ can be replaced by a continuous field $\phi(\boldsymbol{r})$.

A few common examples of order parameters with a different number of compo

nents are listed below. (i) A density wave order (e.g. a charge density wave in the 1D Peierls transition), where the density parameter $\rho(\boldsymbol{R}_i, t) = \rho_0 + \mathrm{Re}\{e^{i\boldsymbol{Q}\boldsymbol{R}_i}\phi_\rho(\boldsymbol{R}_i, t)\}$ oscillates around the average value ρ_0, is described by the scalar real order parameter ϕ_ρ ($O(N)$, $N = 1$). (ii) A magnetic QPT (e.g. AFM - paramagnet QPT) is characterized by a vector order parameter. In the case of an isotropic system with the full rotational invariance in the spin space, the corresponding symmetry group of the order parameter is $O(3)$. In the presence of a strong easy-plane or easy-axis spin anisotropy, the symmetry group reduces to the $O(2)$ group of in-plane rotations (e.g. XY or XXZ model). The magnetic order parameter ϕ_s^α is expressed via local spin vector S_α as

$$S^\alpha(\boldsymbol{R}_i, t) = \mathrm{Re}\{\phi_s^\alpha(\boldsymbol{R}_i, t)e^{i\boldsymbol{Q}\boldsymbol{R}_i}\}, \quad \alpha = x, y, z. \tag{1.2}$$

The ordering vector for a ferromagnetic state $\boldsymbol{Q} = 0$, therefore the order parameter ϕ_s^α coincides with the local spin orientation S^α. The ordering vector for an AFM state is $Q = (\pi, \pi, \ldots)$ (assuming hypercubic lattice with a unit spacing) and the order parameter $\phi_s^\alpha \propto (-)^i S_i^\alpha$ represents a staggered magnetization. The order parameter ϕ_s^α in the both cases of FM/AFM states is real valued. Furthermore, Eq. (1.2) describes non-collinear spin-spiral order, when the ordering vector $\boldsymbol{Q}$ is incommensurate. (iii) Conventional s-wave superconducting phase in metals and a superfluid phase in ^4He are described by a complex-valued order parameter with the $U(1)$ gauge symmetry [2].

A typical phase diagram of a continuous QPT is shown in Fig. 1.1 (a,b) (see Ref. [3]). The panel (a) corresponds to two-dimensional quantum systems and the panel (b) correspond to three-dimensional systems. At zero temperature the QPT phase diagram is separated by the QCP in ordered and quantum disordered phases. According to Mermin-Wagner theorem [4] a long-range order in $2D$ systems ($D = 2 + 1$) with a continuous symmetry group exists only at zero temperature. At $T > 0$ the long-range order is destroyed by thermal fluctuations (at the distances larger then the correlation length ξ) and the "quantum ordered phase" transforms to a "thermally disordered" phase, see Fig. 1.1a. On the other hand in $3D$ systems ($D = 3 + 1$) the ordered phase persists at non-zero temperatures up to a critical

temperature $T_c(g)$, where the melting into a thermally disordered state occurs, see Fig. 1.1b. The critical temperature $T_c(g)$ has a meaning of Curie (Neel) temperature for a ferromagnetically (antiferromagnetically) ordered state. The transition at $T_c(g)$ is essentially a classical thermal phase transition, since thermal fluctuations are much stronger then the quantum fluctuations in the vicinity of the critical line ("classical critical" region in Fig. 1.1b).

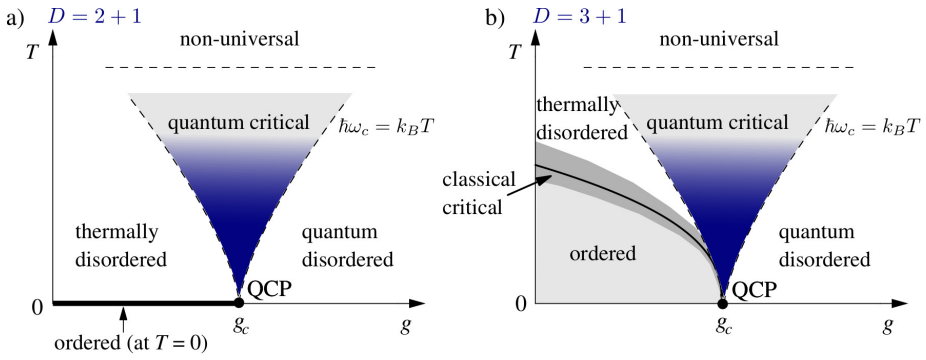

Figure 1.1: A phase diagram for a QPT separating ordered and quantum disordered phases in (a) $D = 2$ (+ time), (b) $D = 3$ (+ time) systems.

Physical observables, such as the order parameter correlation length ξ, excitation gap Δ and magnetic susceptibility susceptibility χ exhibit non-analytical dependence on the tuning parameter g in the vicinity of the QCP [1]. For instance, the correlation length diverges at the QCP at $T = 0$, $\xi(g) \propto |g - g_c|^{-\nu}$, where ν is the critical exponent. The characteristic excitation gap in the vicinity of the QCP scales as $\Delta \propto 1/\xi \propto |g - g_c|^{-\nu}$ and exactly vanishes at the QCP. All observables have power law dependences on the external parameters g, T. The set of corresponding exponents (critical indexes) completely describe the particular QPT.

The region near the QCP, that spreads over nonzero temperatures, is called "quantum critical" domain, see Fig. 1.1. The "quantum critical" region boundary on the phase diagram is determined by comparing the typical energy of long-distance order parameter fluctuations $\Delta = \hbar\omega_c \propto 1/\xi$ and the thermal energy T: $T > \hbar\omega_c \propto |g - g_c|^{\nu}$. In this region the system "looks critical" with respect to the tuning parameter g_c, but is driven away from criticality by thermal fluctuations. The main feature of this region is the absence of conventional quasiparticle-like excitations: the quasiparticles become over-damped. Universal critical behavior persists in the

vicinity of the QCP, i.e. when the correlation length is much larger than microscopic length scales. A quantum critical behavior is cut off at high energies/temperatures, i.e. when T exceeds characteristic microscopic energy scales in the system ("non-universal" region). In quantum magnets the "ultraviolet" cutoff is set by the typical Heisenberg exchange energy.

The critical index ν for a quantum system in $D = d + 1$ dimensions coincides with the corresponding critical exponent for a classical second order thermal phase transition, $\xi(T) \propto |T - T_c|^{-\nu}$, in $D = d$ spatial dimensions [1]. Similarly, other critical indexes characterizing QPTs coincide with their classical counterparts. This provides a deep relation between QPTs and classical PTs, a "classical-quantum correspondence". The quantum-classical mapping can be understood in terms of analytical continuation of response functions from real to imaginary (Matsubara) time/frequency.

In order to illustrate the quantum-classical analogy we consider an order parameter correlation function $G \sim \langle \phi\phi \rangle$ at the critical point. In the classical d-dimensional system the correlation function typically has a power-law dependence on the momentum

$$G(q) \propto q^{-2+\eta_d}, \tag{1.3}$$

where η_d is a corresponding critical exponent. For a QPT at $T = 0$ in $d+1$ space-time dimension the retarded Green's function can be obtained by analytical continuation of Eq. (1.3):

$$G^R(q, \omega) \propto (q^2 - \omega^2 + i0)^{(-2+\eta_{d+1})/2}. \tag{1.4}$$

This examples shows the specific character of the excitation spectrum at a QCP: G^R does not show a conventional quasiparticle pole, but instead a branch cut for $\omega > q$, corresponding to a continuum of critical excitations.

One of the most remarkable features of continuous phase transitions is their universality. Since in the vicinity of a QCP the correlation length $\xi \to$ diverges, the critical system does not have an internal length scale. The theory describing a QPT becomes scale invariant and the essential physics is determined by long range order parameter fluctuations. Therefore, the microscopic details of the system are unimportant at QCP and the quantum critical physics is universal. The universality

classes are determined only by the symmetries of the order parameter and by the space dimensionality of the system [5]. The values of critical exponents are fixed for a given class of phase transitions which may occur in very different physical systems. This implies that the critical properties of a phase transition occurring in nature can be determined by investigating any simple model system belonging to the same universality class.

QPTs are successfully described in terms of of quantum field theory models. The cornerstone of the theory of phase transitions is a so called ϕ^4 model. This model represents the standard Landau-Ginzburg-Wilson approach to the theory of phase transitions and it can be applied to a variety of physical systems [2, 6]. For example, a QPT in $D = d + 1$ dimensional system belonging to $O(N)$ universality class can be modelled by an action

$$S = \int dt d^d x \left[\frac{(\partial_t \phi_\mu)^2}{2} - \frac{(\nabla \phi_\mu)^2}{2} - \frac{(g - g_c)}{2} \phi_\mu \phi^\mu - \alpha \frac{(\phi_\mu \phi^\mu)^2}{4!} \right], \qquad (1.5)$$

where ϕ_μ is a N-component real field. The action (1.5) is invariant with respect to global $O(N)$ rotations. In the quantum disordered phase, $g > g_c$ (symmetric phase), the expectation value of the order parameter is zero $\langle \phi_\mu \rangle = 0$. In the symmetric phase there are N degenerate massive excitations. In the ordered phase at $g < g_c$ the $O(N)$ symmetry of the ground state is spontaneously broken, $\langle \phi_\mu \rangle \neq 0$. The spontaneous symmetry breaking generates $N - 1$ massless Goldstone modes [7] and a massive Higgs mode.

The critical indexes for a QPT can be calculated on the basis of the ϕ^4 theory using renormalization group (RG) technique [8]. RG is a very powerful tool for the scaling analysis of local field theories, which is designed to determine the asymptotic low-energy, long-wavelength characteristics of a system. In the momentum-shell formulation, the RG procedure leads to an elimination of high-energy degrees of freedom and results in a low energy effective theory with renormalized parameters. The low-energy theory is obtained via iteratively integrating out the order parameter fluctuations with large momentum/frequency. The one-loop RG result for the correlation length and correlation function critical indices in the $O(N)$ symmetric

theory reads [9]

$$\nu^{-1} = 2 - \frac{N+2}{N+8}\epsilon + \ldots, \quad \eta_d = \frac{N+2}{2(N+8)^2}\epsilon^2 + \ldots. \tag{1.6}$$

Here $\epsilon = 4 - D$ and the expressions (1.6) are obtained within so-called ϵ-expansion around the upper critical dimension $D_c^+ = 3 + 1$. The upper-critical dimension defined as a certain dimension D_c^+, above which critical fluctuations become irrelevant, i.e. the critical indexes coincide with their mean-field values, e.g. $\nu = 1/2$, $\eta_d = 0$. Above the upper critical dimension quantum fluctuations do not affect physical observables, since the fixed point of the RG flow corresponds to non-interacting theory, $\alpha \to 0$. Below the upper-critical dimension, $D < D_c^+$, the critical fluctuations strongly renormalize the theory, and the physical observables demonstrate power-law dependences on the tuning parameters (e.g. g, T) with nontrivial critical exponents. The critical behaviour below the upper critical dimension is determined by a Wilson-Fisher fixed point of the RG flow, where the system effectively become strongly interacting [10]. If the system's dimension is equal to upper critical dimension, $D = D_c^+$, the effect of critical fluctuations is marginal, and the renormalization of physical observables instead of power-law becomes only logarithmic. With reducing the dimensionality of the system the role of quantum critical fluctuations becomes more important.

Quantum phase transitions have been found in many condensed matter systems, including cuprates [11, 12, 13], iron pnictides [14], heavy fermion compounds [15, 16, 17], two-dimensional electron gases [20, 21], rear earth magnetic insulators [18], ruthenates [19] and dimerized quantum magnets [22, 23]. Study of quantum phase transitions is important for a search of new materials with desired quantum properties is vital for future technology development.

Below we discuss some aspects of quantum critical phenomena in quantum magnets and cuprates.

1.2 Quantum phase transitions in quantum magnets

Pressure driven QPTs have been observed in spin dimer compounds, such as $TlCuCl_3$ [22, 23], $KCuCl_3$ [24] and $CsFeCl_3$ [25]. These compounds are three dimensional magnetic insulators, at an ambient pressure the ground state of the system is paramagnetic. By applying a hydrostatic pressure at some critical pressure $p = p_c$ the system undergoes through a QPT from paramagnetic to a long-range ordered Neel state.

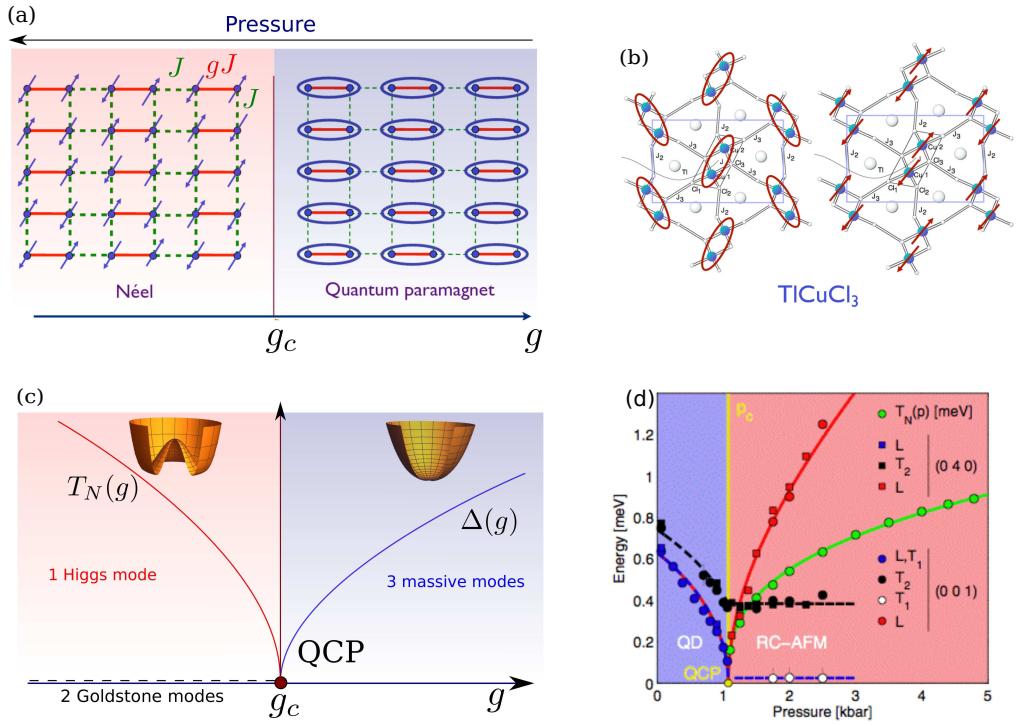

Figure 1.2: (a) A toy model of a $O(3)$ QPT in a dimerized antiferromagnet. The QCP separates a Neel magnetic phase ($g < g_c$) and a quantum paramagnetic phase ($g > g_c$). The ellipses show dimer bonds. (b) Crystal structure of a spin dimer quantum magnet $TlCuCl_3$. (c) The spin excitation gap versus tuning parameter g near a QCP. (d) Excitation gaps and Neel temperature in $TlCuCl_3$ as measured in inelastic neutron scattering [23].

In order to illustrate the physics of QPT in quantum magnets, let us consider a model shown in Fig. 1.2a. The model is represented by a Heisenberg antiferromagnet with two types of exchange coupling constants: the strong coupling inside of each

dimer (gJ) and the weak interdimer (J) coupling. In the limit $g \to \infty$ the spins inside of each dimer form a spin-dimer "atom" with total spin zero. The ground state of the system at $g \gg 1$ is a "quantum paramagnet" - system of weakly interacting singlet dimers. Deeply in the disordered phase of a structurally dimerized magnet the wave function of each dimer reads

$$|\psi\rangle = \prod_{\{i,j\}} \frac{1}{\sqrt{2}} \left(|\uparrow\rangle_i |\downarrow\rangle_j - |\downarrow\rangle_i |\uparrow\rangle_j \right), \tag{1.7}$$

where $\{i, j\}$ are the lattice sites in a dimer and the expectation value of a local spin at any lattice site is $\langle \boldsymbol{S}_i \rangle = 0$. On the other hand, in the case $g \to 1$ the system is a Neel antiferromagnet. Therefore, should exists a critical value g_c of the tuning parameter, a quantum critical point, where the QPT from disordered to Neel phase takes place.

In structurally dimerized compounds, such as $TlCuCl_3$ (see Fig. 1.2c), external pressure affects the exchange interaction between electrons in each dimer. The tuning parameter of quantum criticality g has a meaning of inverse pressure. The elementary spin excitations in the paramagnetic phase are gapped: there are three degenerate excitation modes (called "triplons"), that correspond to a singlet-triplet transition at the site of a dimer. The triplon gap vanishes at the QCP, see Fig. 1.2b. On the other side from the QCP, in the Neel phase, the spin excitations are an amplitude ("Higgs") mode and the two spin-wave (Goldstone) modes. The triplon, Higgs and Goldstone modes were unambiguously measured in $TlCuCl_3$ with inelastic neutron scattering [23]. One of the two Goldstone modes has a small gap due to a weak spin anisotropy present in $TlCuCl_3$ (see e.g. [26]). Quantum critical properties of $TlCuCl_3$ can be explained on the basis of $O(3)$ ϕ^4 continuous field theory in $D = 3 + 1$ dimensions [27].

1.3 Critical phenomena in high Tc superconductors

The discovery of superconductivity by Bednorz and Müller in the perovskite compound $La_{2-x}Ba_xCuO_{4+\delta}$ ($T_c = 35K$) [28] initiated the era of high temperature superconductivity. Within a few years after the discovery, high temperature superconductivity was found in various copper oxide materials, including $YBa_2Cu_3O_{6+x}$ (YBCO) with the critical temperature of the order of 100K.

While dozens of cuprate superconductors are known, they all share main common features. (i) Cuprates have layered structure consisting of weakly coupled CuO_2 planes, see Fig. 1.3a. The physics of cuprates is essentially "two-dimensional" and constrained in the copper oxide planes. (ii) Parent cuprate compounds are Mott insulators with the Neel ground state. The electron spins at the planar Cu sites aligned antiferromagnetically, the electron spin is $S = 1/2$ per Cu site. (iii) The Cu-O planes are "doped" by chemical substitution of atoms in "charge-reservoir" layers so that electrons are removed (hole-doped) or added (electron-doped) to the copper oxide planes. The value of doping dramatically affects cuprates properties and acts as a "tuning parameter" driving the system through a number of quantum phases. (iv) Superconductivity (SC) exist in a finite doping range $p_{min} < p < p_{max}$. The superconducting region on the $T - p$ phase diagram has a dome-like shape with the maximum T_c at an optimal doping $p = p_{opt}$, see Fig. 1.3b. (v) Cuprates are "highly correlated materials" due to strong onsite Coulomb repulsion of holes (electrons) in the Cu-O layers. (vi) The superconducting order has d-wave pairing symmetry.

The doping range $p < p_{opt}$ correspond to underdoped cuprates and cuprates with the doping $p > p_{opt}$ are called overdoped. To be specific we will discuss only hole-doped systems, such as YBCO. The $T - p$ phase diagram for hole-doped cuprates is shown in Fig. 1.3.

The phase diagram for cuprates is quite complex and consist of a number of exotic quantum phases. In the underdoped region the phase diagram is represented by AFM, SC and "pseudogap" phase. The "pseudogap" phase is characterised by an unusual hole Fermi-surface with open topology, called Fermi-arcs [29, 30]. Pseudogap region persists in the temperature range $T_c < T < T^*$, the phase boundary

line near T^* (dashed yellow line in Fig. 1.3) is not well defined and rather corresponds to a finite temperature crossover. In the optimally doped region above T_c is referred as "strange metal". The pseudogap and strange metal phases are still poorly understood, their distinct feature is the absence of well defined quasiparticle excitations. The overdoped region is characterized by large hole Fermi surface and can be described as a normal Fermi liquid [11].

Recently two novel phases were found in the underdoped cuprates: incommensurate spin spiral (green dashed line in Fig. 1.3b) and incommensurate charge density wave (red dashed line in Fig. 1.3b). Below we will discuss these two phases in more detail.

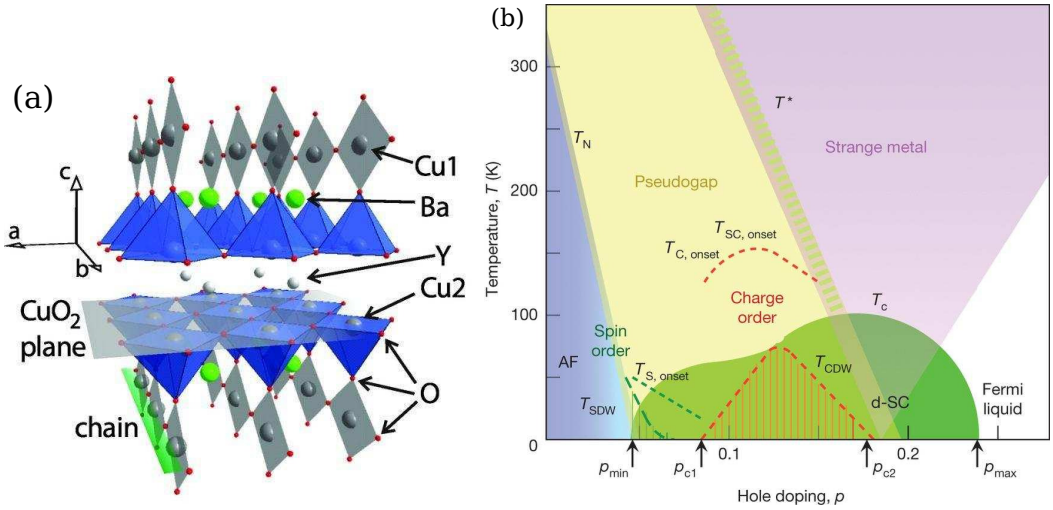

Figure 1.3: (a) Crystal structure of a high temperature superconductor YBCO (from [35]). (b) Generic phase diagram (temperature versus doping) for hole-doped cuprates (from [13]).

1.3.1 Magnetic quantum critical point in cuprates

Undoped and lightly doped cuprates posses collinear AFM order. On the other hand, optimally doped and overdoped cuprates do not have any static magnetic order. In the underdoped region a new type of magnetic order - an incommensurate spin spiral - has been detected recently near the boundary between AFM and SC phases, see Fig. 1.3.1a. The existence of static incommensurate magnetic order ("spin density wave", SDW) in YBCO has been established in neutron scattering

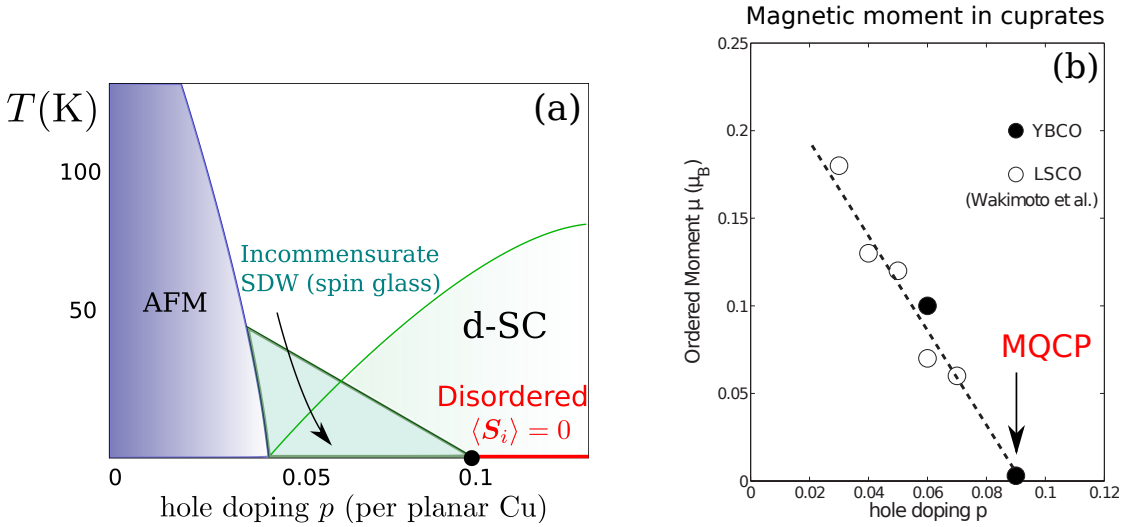

Figure 1.4: (a) Phase diagram for YBCO (zoomed in) near the magnetic QCP (MQCP) at $p \approx 0.09$ [33]. The MQCP separates incommensurate spin spiral phase and magnetically disordered phase. (b) Magnetic moment at low temperature as a function of doping in cuprate compounds YBCO and LSCO [31]. The magnetic moment in YBCO vanishes at the MQCP.

and muon spin rotation (μSR) experiments at low temperatures [31, 32, 33].

The incommensurate SDW is believed to be a universal phenomenon for hole doped cuprates, below we will refer specifically to YBCO. The wave vector of the SDW ordering $\boldsymbol{Q}_{SDW} = (\pi \pm \delta_{SDW}, \pi)$ is close to the AFM wave vector $\boldsymbol{Q}_{AF} = (\pi, \pi)$. The SDW order in YBCO persists in the doping range $0.05 < p < 0.09$, the incommensurability δ_{SDW} increases with p. The wave vector of the spin spiral is aligned along the main crystallographic axis a, see Fig. 1.3a. The spiral order is two-dimensional and is constrained within CuO planes. The SDW is unidirectional, it breaks underlying discrete symmetry group C_4 invariance of the unit cell of a CuO plane and reduces it to a two-fold rotational symmetry C_2. That is why the SDW is also called "electron nematic" phase [32].

At doping level $p \approx 0.09$ the static local magnetic moment at Cu sites vanishes, $\langle \boldsymbol{S}_i \rangle \to 0$, see Fig. 1.3.1b. The melting of the local magnetic moment indicates the presence of a QCP that separates the incommensurate phase from magnetically disordered phase. At larger doping after crossing the QCP the (quasi-) static magnetic ordering vanishes and becomes fully dynamic. The transition into the incommensurate SDW phase is of the "spin freezing" type [32], since the incommensurate SDW

phase has features of a "spin glass" state. The characteristic frequency of electronic spin fluctuations is reduced with decreasing temperature. Upon further cooling, the spin system gradually freezes into an ensemble of slowly fluctuating, finite-sized domains. The magnetic QCP is well pronounced in YBCO, however it is smeared by an intrinsic disorder in LSCO.

The spin excitations are gappless in the SDW phase. In the magnetically disordered phase the spin gap opens. The magnetic QCP separating these two regions was theoretically predicted at the doping $p \approx 0.1$, that agrees well with the experimentally found position of the QCP [34].

1.3.2 Charge density wave in cuprates

Incommensurate charge density wave (CDW) order has been recently discovered in underdoped cuprates in bulk sensitive measurements, such as resonant inelastic x-ray scattering (RIXS) [35, 36, 37], resonant X-ray scattering [38], hard X-ray diffraction (XRD) [39] and nuclear magnetic resonance (NMR) [41, 42, 43]. The surface scanning tunnelling microscopy (STM) confirms the presence of the CDW state in cuprates [44, 45]. The CDW order has been found in YBCO and other cuprate families [45, 46], below we will specifically refer to YBCO. Note, that the incommensurate CDW phase is distinct [35] from the well known commensurate charge ordered phase in La based cuprates at $p = 1/8$ [47, 48].

The first direct observation of incommensurate CDW comes from RIXS [35], the X-ray photon energy was tuned to Cu $2p \rightarrow 3d$ transition. RIXS technique probes a spatial charge distribution of the valence electrons. An anomalous peak was detected at incommensurate wave vector $Q_{CDW} = 0.31$ of reciprocal lattice units (r.l.u.), see Fig. 1.3.2, the period of the modulation is $1/Q_{CDW} = 3.2$ lattice spacings. The CDW peak appears below the critical temperature $T_{CDW} \approx 150$ K, the intensity of the RIXS signal grows with decreasing of temperature. The anomalous peak in RIXS corresponds to the spatial modulation of electron density, the wave vector of the CDW lies in the CuO planes. The CDW peaks are located at the wave vectors $\boldsymbol{Q}_{CDW} = (Q, 0)$ and $\boldsymbol{Q}_{CDW} = (0, Q)$, the both peaks have equal RIXS intensity. This data are consistent with two possible spatial patterns of the CDW:

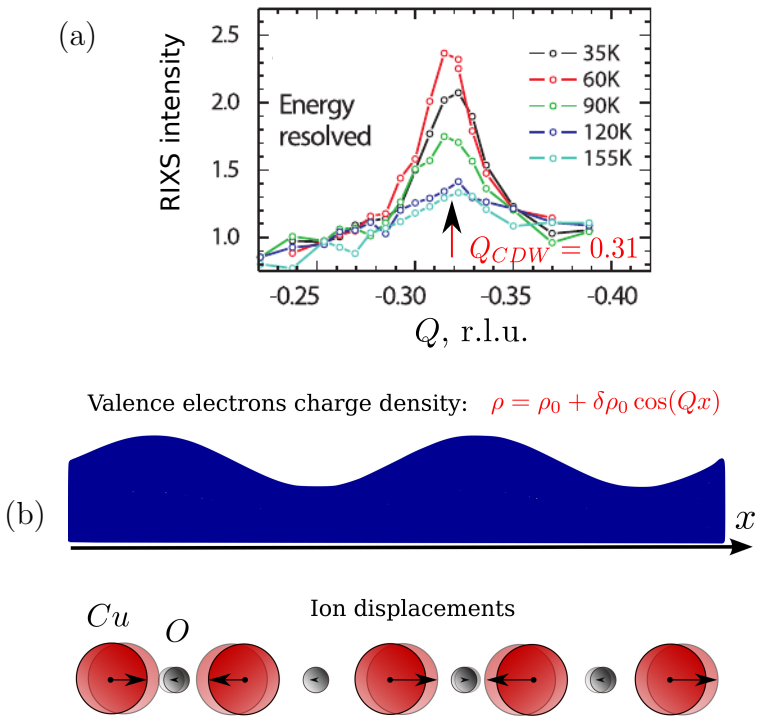

Figure 1.5: (a) Incommensurate CDW in YBCO ($p = 0.11$) at the wave vector $Q = 0.31$ r.l.u. as measured by RIXS [35]. (b) Schematic illustration of CDW modulation in the CuO plane of cuprates.

(i) a biaxial (checkerboard) CDW with coexisting $(Q, 0)$ and $(0, Q)$ modulations, (ii) statistically equivalent domains with a uniaxial (stripe-like) CDW, the wave vector in each domain is either $(Q, 0)$ or $(0, Q)$.

A supporting evidence for the CDW order comes from XRD measurements. XRD technique probes inner core electrons, therefore XRD is sensitive to ionic displacements. XRD data also shows the presence of anomalous peak at the same incommensurate wave vector Q_{CDW} [39], that corresponds to CDW induced modulation of ions displacements (see Fig. 1.3.2). XRD experiments identify both inplane and out of plane components of Cu and oxygen ions displacements [40]. The CDW wave vector is almost independent on doping [37].

At the temperatures below superconducting temperature T_c, the CDW amplitude decreases [35, 39]. This phenomenon has interpreted as a result of competition between SC and CDW orders. Interestingly, the position of the dip in SC dome at

$p \sim 0.11$ coincides with the maximum of T_{CDW} on the $T-p$ phase diagram, see Fig. 1.3, that supports scenario of competing SC and CDW orders.

The observation of CDW modulation by RIXS and XRD preceded by NMR measurements [41]. The analysis of quadrupole satellites in the NMR spectrum allows to extract information about about the electron charge spatial distribution in a CuO plane. Electron density modulation results in additional inhomogeneous broadening of the Cu and oxygen NMR quadrupole satellites at $T < T_{CDW}$. This approach of measuring charge distribution in a crystal is analogous to zero-field nuclear quadrupole resonance technique (NQR). NQR probes electric field gradient at the Cu/O nucleus site created by surrounding electrons. Since NMR/NQR measurements do not provide information about the spatial periodicity of the CDW modulation, additional evidences (e.g. from RIXS/XRD) were required to identify charge ordered phase in cuprates.

1.4 Impurities at quantum criticality and emerging orders

A particularly elegant strategy to study strongly correlated materials is to introduce a small concentrations of well-characterized impurities in a pure sample. Impurities can induce charge and spin textures that can be detected experimentally using NMR, elastic/inelastic neutron scattering, STM and etc. [49]. Such experiments provide a valuable information about the properties of the ground state / low energy excitations of the system. Experimental studies of the effects of nonmagnetic impurities have been performed in quasi-1D spin-gapped insulators [50, 51], cuprate high-Tc superconductors [52, 53, 54, 55] and 3D spin-dimerized magnets [56, 57, 58]. These experiments have motivated theoretical studies of impurity-induced effects in antiferromagnets [59, 60, 61, 62], superconductors [63], as well as in quantum magnets near QCP [64, 65, 66].

Impurities can be introduced in a system by a chemical substitution. For example, substituting in a cuprate compound YBCO magnetic Cu ion with a nonmagnetic ion Zn^{2+} or Mg^{2+} creates a vacancy with uncompensated spin 1/2 (see Fig. 1.4).

Another example is a spin-dimerized compound $TlCuCl_3$: a substitution of Cu ion to Zn ion breaks a singlet dimer bond; the remaining unpaired Cu spin acts as an effective spin 1/2 impurity. The missing magnetic moment disturbs the local spin alignment of the neighbouring spins and creates a magnetization cloud around the impurity site, see Fig. 1.4. The radius of the cloud is determined by the spin correlation length ξ. The spatial distribution of magnetization in the cloud can be probed e.g. by analysing NMR response of Cu nuclei. In particular, magnetization cloud induced by an impurity leads to inhomogeneous NMR line broadening and results in an additional spatially modulated Knight shift [54, 64].

An interplay between disorder and quantum criticality is a particularly interesting problem. The physics of quantum critical systems in the presence of impurities/disorder is quite complex and there is a little understanding/progress in this area. Experimental studies in 2D and 3D systems show that nonmagnetic impurities can significantly influence properties of quantum magnets near QCP: impurities can induce order in the macroscopic volume of the crystal ("order from disorder" mechanism) and shift the position of a QCP [56, 57, 58]. In the vicinity of a QCP the role of impurities becomes especially important: the characteristic radius of the magnetization cloud around impurities $\xi \sim 1/\Delta \to \infty$ diverges at QCP (Δ is the spin excitation gap), as well as various response functions (e.g. magnetic susceptibility) exhibit unusual power-law behaviour characterized by anomalous exponents [64]. In the regime of a sufficiently large density of impurities (but below the percolation limit) a transition into a Mott/Bose glass phase can occur [67, 68, 88, 70].

Impurity's spin/charge can become screened by the surrounding electrons. The classical example is a Kondo screening of a magnetic moment of an impurity by a Fermi sea of electrons [71]. In the present thesis we will be interested in the screening problem of an impurity's spin by bosonic (magnon) excitations. This class of problems are called Bose-Kondo problems [3]. The minimal coupling model of an impurity with a vector bosonic bath reads

$$\mathcal{L}_{int} \sim \phi^{\alpha}(r,t) S^{\alpha}_{imp}(r,t), \quad \alpha = x,y,z. \tag{1.8}$$

We assume that the only dynamical degree of freedom of the impurity is a Berry

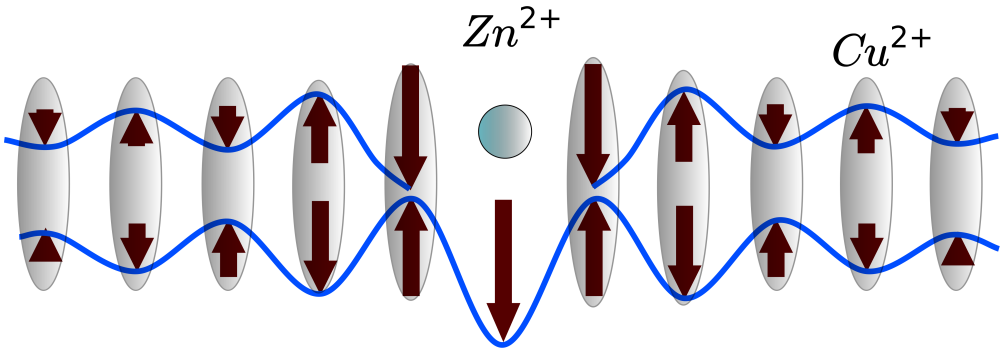

Figure 1.6: Staggered moments (arrows) of Cu ions around a single nonmagnetic Zn impurity in a spin-dimer AFM (e.g. $SrCu_2O_3$ [51] or $TlCuCl_3$). The staggered magnetizaion is induced on a characteristic length $\xi \sim 1/\Delta$ (Δ is a spin excitation gap). The size of each arrow represents the value of the magnetic moment.

phase, associated with the orientation of the effective spin $S_{imp} = 1/2$ of the impurity. It is worth emphasizing that $\mathcal{L}_{int}$ is to be viewed as a long-wavelength theory and requires some interpretation when applied to lattice models. In particular when a nonmagnetic impurity replaces a spin-1/2 ion, there is clearly no spin degree of freedom directly at the impurity site. In this case by $\boldsymbol{S}_{imp}$ we assume the orientation of the spin at the Cu ions very close to the vacancy site. The spin $\boldsymbol{S}_{imp}$ measures the instantaneous orientation of the collective spin polarization which is centered on a nonmagnetic Zn site, and the Berry phase is the net uncompensated contribution obtained by summing over the Berry phases of all the spins on the neighboring Cu ions.

1.5 Topological defects in magnets: skyrmions and merons

Topological defects play a profound role in cosmology, particle physics and condensed matter physics. Examples of such defects include dislocations, disclinations, domain walls, cosmic strings, vortices, skyrmions and merons. In the present section we discuss topological defects (skyrmions and merons) in magnetic systems.

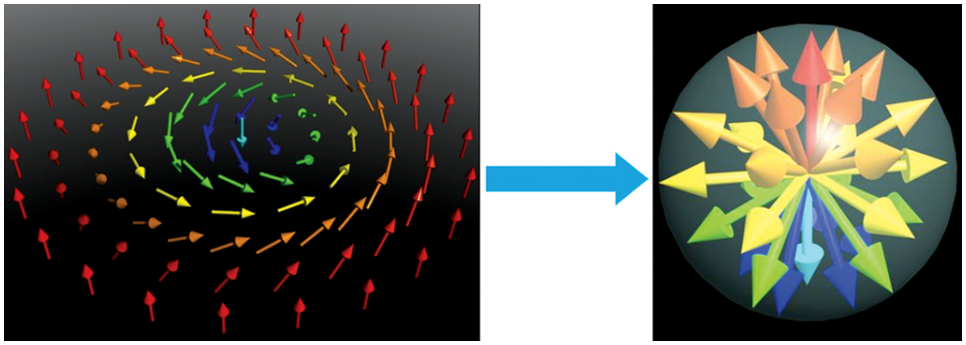

Figure 1.7: A skyrmion as a mapping of 2D plane onto unit sphere $R^2 \to S^2$ (from [73]). The topological charge $Q = 1$ represents a number of wraps of the spin vector around the sphere.

1.5.1 Skyrmions

A skyrmion is a hedgehog-like vector soliton with a nontrivial topological charge. Skyrmion was originally proposed by T. Skyrme [72] in the context of nuclear physics as a model describing baryons and mesons. Skyrmions and skyrmion phases have been predicted and realized in the context of condensed matter in Quantum Hall states of a two-dimensional electron gas [75], spinor Bose-Einstein condensates [76], chiral liquid crystals [77] and chiral magnets [78, 79, 80, 84].

A skyrmion in two spatial dimensions is a noncomplanar configuration of a vector field (e.g. spin, magnetic moment) $\boldsymbol{n}(x, y)$ that wraps around a sphere an integer number of times. Skyrmion corresponds to a mapping $R^2 \to S^2$. Here R^2 refers to $\{x, y\}$ plane and S^2 refers to a unit 2-sphere ($\boldsymbol{n}^2 = 1$), see Fig. 1.7. The mapping $S^2 \to S^2$ between a point on the 2-sphere and an orientation of vector $\boldsymbol{n}$ can be classified by an integer Q referred as a topological number or a topological charge. Topological charge Q has a meaning of a degree of the mapping $S^2 \to S^2$ and represents number of times the unit vector $\boldsymbol{n}$ spans around the unit sphere [81]:

$$Q = \frac{1}{4\pi} \int d\Omega = \frac{1}{4\pi} \int d^2r \; \boldsymbol{n} \cdot [\partial_x \boldsymbol{n} \times \partial_y \boldsymbol{n}]. \tag{1.9}$$

The density of topological charge $\rho_Q(x, y) = \frac{1}{4\pi} \boldsymbol{n} \cdot [\partial_x \boldsymbol{n} \times \partial_y \boldsymbol{n}]$ is a Jacobian of the mapping $R^2 \to S^2$. Note, that for any continuous transformation of a vector field the skyrmion topological charge remains invariant. This results in so-called topological protection of skyrmions.

The skyrmion field configuration in spherical coordinates can be represented as

$$\boldsymbol{n}(\boldsymbol{r}) = (\sin\Theta(\boldsymbol{r})\cos\Phi(\boldsymbol{r}),\ \sin\Theta(\boldsymbol{r})\cos\Phi(\boldsymbol{r}),\ \cos\Theta(\boldsymbol{r})), \tag{1.10}$$

where $\Theta(\boldsymbol{r})$ and $\Phi(\boldsymbol{r})$ are the spherical angles that parametrize a point on S^2 sphere. Let us define the center of a skyrmion as $\boldsymbol{r} = 0$ and introduce the polar coordinates $\{r\phi\}$ on the 2D plane. The boundary conditions corresponding to a skyrmion solution can be fixed as follows:

$$\Theta(r)\big|_{r=0} = \pi, \quad \Theta\big|_{r\to\infty} = 0, \tag{1.11}$$

i.e. the spin points down at the center of the skyrmion and point up at the infinity. Considering for simplicity a skyrmion with azimuthal symmetry we can write $\Phi(\boldsymbol{r}) = \Phi(\phi)$. Due to the periodicity condition the only possible form of the function Φ reads $\Phi(\phi) = N\phi + \chi$, where N is integer and $\chi \in [0, 2\pi]$ is an arbitrary angle. The parameter N is called "vorticity" and the angle χ is called "helicity". For example, for the skyrmion in Fig. 1.7 the vorticity and helicity are $N = 1$, $\chi = \pi/2$. As the result, the topological charge of the skyrmion reads

$$Q = \frac{1}{4\pi}\int d\cos\Theta(\boldsymbol{r})d\Phi(\boldsymbol{r}) = \frac{1}{4\pi}\left[\cos\Theta(r)\right]\Big|_0^\infty \left[\Phi(\phi)\right]\Big|_0^{2\pi} = N, \tag{1.12}$$

so the topological charge equals to the vorticity.

Skyrmions are topological solutions of corresponding nonlinear field equations. The simplest theoretical model supporting skyrmion solutions is a classical $O(3)$ nonlinear sigma model (NLσ), that describes 2D Heisenberg ferromagnet at zero temperature [82]. The elastic energy of the spin field in NLσ model reads

$$E = \frac{\rho_s}{2}\int d^2r\ (\partial_i n_\mu)^2, \quad i = x, y, \quad \mu = 1, 2, 3, \tag{1.13}$$

where $\rho_s > 0$ is a spin stiffness coefficient. The lowest energy ($E = 0$) field configuration for the model (1.13) is a uniform ferromagnetic (FM) state, e.g. $\boldsymbol{n} = \boldsymbol{e_3}$. The FM ground state is topologically trivial, since the topological charge $Q = 0$, see Eq.

(1.9). The expression (1.13) can be equivalently preseneted in the form [83]

$$E = 4\pi\rho_s|Q| + \frac{\rho_s}{4}\int d^2r\ \left[\partial_i \boldsymbol{n} \pm \epsilon_{ij}(\boldsymbol{n}\times\partial_j\boldsymbol{n})\right]^2 \geq 4\pi\rho_s|Q|. \tag{1.14}$$

The energy (1.14) is bounded from below in the sector with a fixed topological charge Q. The minimum $E = 4\pi\rho_s|Q|$ of the energy (1.14) is achieved when the expression in brackets $[\ldots]$ is equal to zero. The positive (negative) sign in (1.14) correspond to a skyrmion, $Q > 0$ (antiskyrmion, $Q < 0$) solution. The equation $[\ldots] = 0$ for 3 spin components n_μ can be equivalently represented as the Cauchy-Riemann conditions for a complex valued function $w(z)$ defined via stereographic projection mapping

$$w(z) = \frac{n_1 + in_2}{1 + n_3}, \quad z = x + iy. \tag{1.15}$$

A solution for the Cauchy-Riemann equations is a meromorphic function $w(z)$ of the complex argument z. The skyrmion solution with a topological charge $Q < 0$ reads [83]

$$w(z) = \alpha\prod_{k=1}^{|Q|}\frac{1}{z-\beta_k}. \tag{1.16}$$

An elementary skyrmion with $Q = -1$ is parametrized by two complex parameters (α, β). The position of the skyrmion center is defined as $\beta = \beta' + i\beta''$ on the complex plane z. Parameter $\alpha = |\alpha|e^{-i\chi}$ determines the radius of the skyrmion $R = |\alpha|$ and the helicity angle χ. The solution (1.16), (1.15) corresponds to a minimum energy configuration of $O(3)$ NLσ model (1.13) in the sector with topological charge Q and is called Belavin-Polyakov skyrmion. Note that the energy of a Belavin-Polyakov skyrmion

$$E_{sk} = 4\pi\rho_s|Q| \tag{1.17}$$

does not depend on the skyrmion radius R due to the conformal invariance of the model (1.13). The skyrmion energy also does not depend on helicity χ due to unbroken $O(2) \subset O(3)$ symmetry of global inplane spin rotations.

Belavin-Polyakov skyrmion is a simple mathematical model for topological solutions in a 2D ferromagnet. However, experimental realization of a Belavin-Polyakov skyrmion in real materials is somewhat problematic due to a few reasons: (i) Belavin-

Polyakov skyrmions exist only as excitations and have a positive energy $E_{sk} > 0$ compared to the energy of the uniform ferromagnetic state (ii) the conformal invariance of NLσ model breaks down by subleading spin-spin interaction terms, e.g. next-neighbour Heisenberg coupling.

Skyrmions in magnetic materials can exist not only as isolated topological defects, but they can condense in a new ground state: skyrmion lattice/skyrmion crystal (SkX). SkX phase has been theoretically predicted ~ 30 years ago by Bogdanov and Yablonsky in Dzyaloshinskii-Morya (DM) magnets with broken inversion symmetry [78]. The energy of DM magnet in the continuous limit reads

$$E_{DM} = \int d^3r \left(\frac{\rho_s}{2} (\nabla \boldsymbol{S})^2 + D\boldsymbol{S} \cdot [\nabla \times \boldsymbol{S}] - \boldsymbol{B} \cdot \boldsymbol{S} \right), \tag{1.18}$$

where D is a DM constant, $\boldsymbol{B}$ is the external magnetic field (hereafter we put $g\mu_B = 1$). In a zero magnetic field the ground state of DM magnet is a spin spiral with incommensurate wave vector $Q = D/\rho_s$. At sufficiently large magnetic fields B the ground state is a collinear FM with the magnetization vector oriented along $\boldsymbol{B}$. In the intermediate range of magnetic fields $B_{c1} < B < B_{c2}$ and a finite temperature range the SkX state forms. The SkX is analogous to the mixed phase in type-II superconductors - system of Abrikosov vortices - which exist in intermediate range of magnetic fields between lower and upper critical fields [2]. Skyrmions in SKX state are arranged in a triangular superlattice structure (analogous to triangluar lattice of Abrikosov vortexes), the skyrmions repel each other on short distances. The typical $B-T$ phase diagram of a DM magnet is shown in Fig. 1.8c and contains FM, spiral and SkX phases.

SkX state was observed for the first time in DM material MnSi in 2009 [80] via neutron scattering measurements, see Fig. 1.8a,b, (the material was theoretically proposed in Ref. [79]). Shortly after the discovery SkX was found in a number of DM magnets (3D crystals and 2D films), including $Fe_{1-x}Co_xSi$ [84, 85], FeGe [86, 88], Cu_2OSeO_3 [89]. The SkX has been recently detected on the interfaces of transitional-metal-based magnetic films [93], where skyrmions are stabilized by interfacial DM interactions. The examples include bilayer interfaces Pd/Fe on Ir(111) substrate [95] and interfaces in multilayer thin film stacks [90].

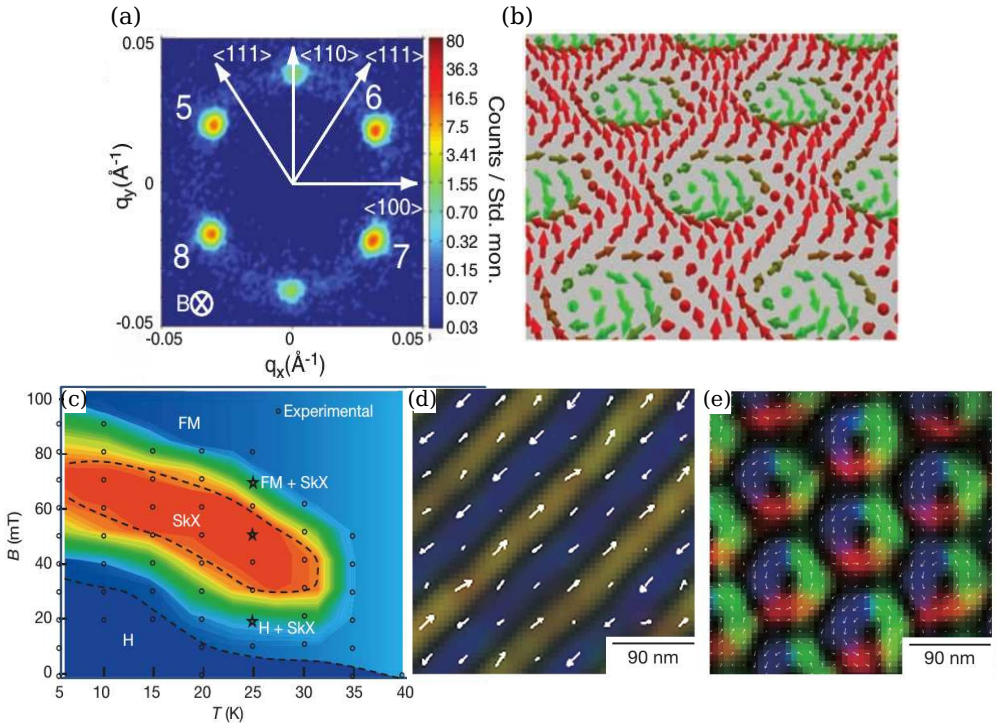

Figure 1.8: (a,b) First experimental obseravation of SkX in DM magnets (MnSi crystal) via elastic neutron scattering [80]. (a) Spin structure factor in momentum space $\boldsymbol{q} = (q_x, q_y)$. The six peaks in the structure factor indicate triangular lattice SkX state. (b) Reconstructed real space spin configuration. (c,d,e) Real space observation of SkX state via Lorentz electron transmission spectroscopy in $Fe_{0.5}Co_{0.5}Si$ film [84]. (c) $B - T$ phase diagram, showing ferromagnetic (FM), spiral/helicoidal (H) phase, skyrmion crystal (SkX) states. (d,e) real space spin configurations: (d) spiral state, (e) SkX state (color indicates direction/magnitude of the inplane spin component).

Magnetic skyrmion has a number of unique properties. Skyrmions are stable with respect to perturbations, since a finite amount of energy is needed to change the topological charge and destroy the skyrmion. Skyrmion phases in DM thin films and multilayer materials are robust up to room temperatures [86, 88, 90, 91, 92]. Moving skyrmions are subjected to an effective Magnus force, that curves the trajectory of the skyrmion ("skyrmion Hall effect") [103, 104]. In the presence of a skyrmion a spin polarized electron current is deflected that results in a "topological Hall effect" [101, 102]. Besides multi-skyrmion SkX phases, single isolated skyrmions have been proven to be stable in FM phase of chiral magnets [96, 98, 99, 97]. Individual skyrmions can be created, manipulated, processed, readout and destroyed [106, 107,

109, 110, 108]. These features make skyrmions attractive for developing low power consumption skyrmion-based magnetic memory and data processing devices.

The search of new skyrmionic materials is an active area in condensed matter physics. In spite of significant progress in the experimental and theoretical frontiers, magnetic skyrmions have been found only in a handful of materials. These materials are DM magnets with noncentrosymmetric B20 cubic crystal structure and the interfaces of transitional-metal-based magnetic films. The key mechanism that drives formation of skyrmions in these materials is DM interaction. For future practical applications it is important to extend number of skyrmionic materials and find new physical mechanisms stabilizing skyrmions. Frustrated magnets can be considered as a new skyrmionic material candidate. The competing spin-spin interactions in frustrated magnets can favour noncollinear ground states, e.g. spin spiral state.

The idea to search for skyrmion states in frustrated magnets was first proposed in Ref. [111]. Using classical Monte Carlo simulations it was shown that a SKX phase can be stabilized in a frustrated magnet - 2D Heisenberg ferromagnet on triangular lattice with next nearest neighbour AFM couplings, see Fig. 1.9a. SkX state can be equivalently considered as a superposition of three spiral states with the wave vectors ($\boldsymbol{q}_1$, $\boldsymbol{q}_2$, $\boldsymbol{q}_3$) that add up to zero, see Fig. 1.8a. This is why SKX is also called a "triple q-state". The triple-q phase persists in finite range of temperatures and magnetic fields: the minimal critical temperature and magnetic field are non-zero, see phase diagram in Fig. 1.9b. The formation of the SkX state is driven by thermal fluctuations, which lead to softening of long-wavelength spin excitations at finite temperatures and result in energetic stability of a skyrmion phase.

SkX and other exotic spiral phases can exist in frustrated magnets even at zero temperature, however the presence of a uniaxial spin anysotropy is required [112]. For example, let us consider a model system of a frustrated ferromagnet with AFM next-neighbouring Heisenberg exchange couplings. The energy of the frustrated magnet with uniaxial spin anysotropy reads

$$E = -J_1 \sum_{\langle i,j \rangle} \mathbf{S}_i \cdot \mathbf{S}_j + J_2 \sum_{\langle\langle i,j \rangle\rangle} \mathbf{S}_i \cdot \mathbf{S}_j + J_3 \sum_{\langle\langle\langle i,j \rangle\rangle\rangle} \mathbf{S}_i \cdot \mathbf{S}_j - \frac{K}{2} \sum_i (S_i^z)^2 - B \sum_i S_i^z. \quad (1.19)$$

Here $J_{1,2,3}$ are the Heisenberg exchange couplings, where J_1 is ferromagnetic and

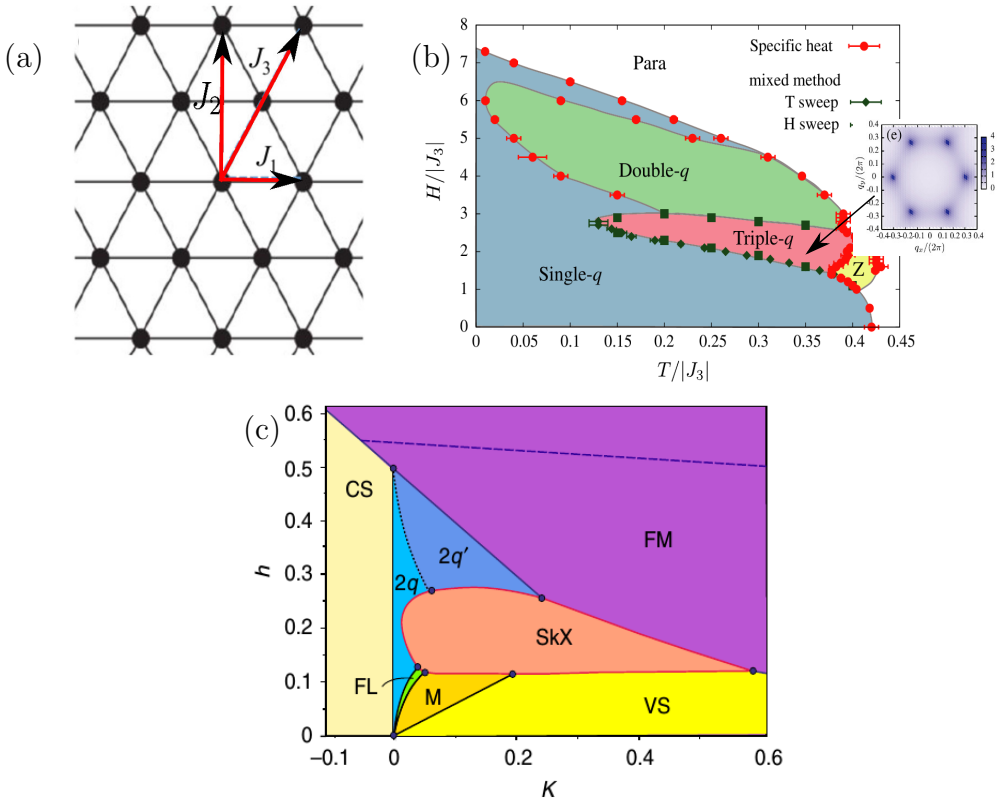

Figure 1.9: (a) Heisenberg model on a triangular lattice. (b) $B-T$ phase diagram for a 2D classical frustrated Heizenberg model on a triangular lattice ($J_2 = K = 0$) [111]. The triple-q region on the diagram corresponds to the SkX phase. (c) Zero temperature $B-K$ phase diagram of a frustrated magnet on a triangular lattice ($J_1 - J_2 - J_3 - K$ model) [112]. The skyrmion crystal phase is denoted as SkX. Here K is a single ion spin anisotropy: $K > 0$ corresponds to easy axis anisotropy, $K < 0$ corresponds to an easy plane anisotropy ($J_1 = 1$).

$J_{2,3}$ are antiferromagnetic couplings ($J_{1,2,3} > 0$). The coefficient K characterizes the single ion spin anisotropy and originates from spin-orbit coupling. Positive (negative) K corresponds to the case of easy-axis (easy-plane) spin anisotropy. Notation $\langle i,j\rangle$, $\langle\langle i,j\rangle\rangle$ and $\langle\langle\langle i,j\rangle\rangle\rangle$ in Eq. (1.19) denotes summation over the nearest, next nearest and next-next nearest neighbour sites. The single ion anisotropy K plays an important role in stabilizing nontrivial spiral and SkX phases, see phase diagram in Fig. 1.9c.

Skyrmions in frustrated magnets have a number of peculiar properties that make them different from skyrmions in DM magnets [74, 112, 113]. (i) The typical size of a skyrmion in frustrated magnets is expected to be a few lattice constants, since the

competing Heisenberg couplings J_i are usually comparable to each other. The size of DM skyrmions on the other hand is larger by at least one order of magnitude because of the smallness of DM constant D. (ii) The energy of skyrmions in frustrated magnets is degenerate with respect to the helicity of a skyrmion and therefore χ is an additional degree of freedom of the skyrmions. On the contrary, the helicity of skyrmions is fixed in DM magnets, $\chi = \pm\pi/2$, where the sign of χ is determined by the sign of D. (iii) Skyrmion-skyrmion interaction for DM skyrmions is repulsive. On the other hand in frustrated magnets the skyrmion-skyrmion interaction potential is a sign-changing oscillating function of the distance r and has regions of attraction and repulsion [112, 113].

1.5.2 Merons

A skyrmion with a unit topological charge can formally be represented as a bound state of two merons - "half-skyrmions" with a topological charge $Q = 1/2$ per meron [122]. A meron is a vortex-like vector field configuration, that wraps around a half of the unit sphere, see Fig. 1.10. Due to their fractional topological charge merons can exist only in pairs and they are tightly confined within the radius of a skyrmion. The concept of merons originates in QCD, where merons have been found as topological solutions of Yang-Mills equations [120] and were proposed to describe quark confinement in hadrons [121, 122].

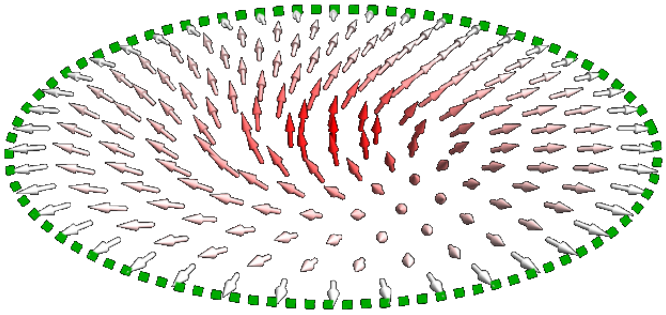

Figure 1.10: A "half-skyrmion" with a topological charge $Q = 1/2$ - meron.

Merons were predicted to have many manifestations in condensed matter systems, such as meron phases in quantum Hall systems [123], bilayer graphene [124], Bose-Einstein condensates [126] and chiral magnets[125, 127]. Single isolated merons

have been experimentally observed in the system of coupled magnetic nanodisks [128, 129, 130], where the merons are stabilized by the boundary of the disks.

Let us consider merons as isolated compact topological defects in 2D systems. The boundary conditions for a single meron can be chosen as follows $S^z(r=0)=1$ and $\boldsymbol{S}(r\to\infty)\to\boldsymbol{e}_{\boldsymbol{r}}$, see Fig. 1.10. The energy of an isolated meron logarithmically diverges with the system size. In the $O(3)$ NLσ model (1.13) the energy of a single meron is $E_{1mer}\sim 2\pi\rho_s\ln(L/a)$, where L is the characteristic system size and a is the radius of a meron. Therefore, isolated merons are energetically unfavourable and merons "prefer" to form pairs.

The density of topological charge for the pair of point-like merons reads

$$\rho_Q(\boldsymbol{r})=\frac{1}{2}\delta^{(2)}(\boldsymbol{r}-\boldsymbol{r}_1)+\frac{1}{2}\delta^{(2)}(\boldsymbol{r}-\boldsymbol{r}_1). \tag{1.20}$$

The total energy of a meron pair reads [122]

$$E_{2mer}\sim 4\pi\rho_s+2\pi\rho_s\ln\left(\frac{R}{\sqrt{a_1a_2}}\right), \tag{1.21}$$

where $R=|\boldsymbol{r}_1-\boldsymbol{r}_2|$ is the distance between the centers of merons located at $\boldsymbol{r}=\boldsymbol{r}_{1,2}$ and $a_{1,2}$ are the radii of the two merons. The formula (1.21) is valid only in the limit of well separated merons: $R\gg a_{1,2}$. In other words, it is valid in the limit of point-like merons $a_{1,2}\to 0$, whereas the distance between the merons is kept fixed. The logarithmic interaction potential between two merons (1.21) at $R\gg a_{1,2}$ has the form of Coulomb potential energy between point-like charges in two spatial dimensions. The constant term $4\pi\rho_s$ in r.h.s. of Eq. (1.21) corresponds to energy of $Q=1$ Belavin-Polyakov skyrmion, see (1.17). The interaction potential in Eq. (1.21) indefinitely grows with the meron-meron separation distance R and has a meaning of meron confinement potential.

1.6 Organisation of the Thesis

In Chapter 2 we consider a problem of fermion-fermion pairing in the vicinity of a magnetic QCP, motivated by the recent discovery of a magnetic QCP in hole-doped

cuprates. We address this problem proposing a toy model of two immobile fermions interacting by exchanging critical magnons. This model contains all the essential physics of the problem: a low number of fermions strongly interacting with quantum critical spin excitations. We consider the limit of low number of fermions (two-fermion problem!) to emphasise the physics of a small Fermi surface in underdoped cuprates. In order to make our calculations specific, we consider interaction of two holes embedded into a bilayer antiferromagnet, which is tuned to a QCP. We report a new mechanism of fermion pairing by quantum critical fluctuations, due to multi-magnon exchange processes, the attraction mechanism is similar to a Casimir effect. In order to calculate the Casimir interaction energy we developed a new method, that we call "Lamb-shift" technique. The Casimir interaction provides a long-range power law attraction between fermions. The Casimir pairing mechanism at QCP is generic.

In Chapter 3 we consider a magnetic screening of an impurity in a quantum critical 3D antiferromagnet. The screening problem is conceptually similar to the Kondo effect. The impurity's magnetic moment in AFM is screened by a cloud of magnon excitations (Bose-Kondo problem), in contrast to a screening by mobile electrons in case of the usual Kondo effect. We explicitly calculate the spatial distribution of the nonlocal magnetization in the magnon cloud. The delocalization of the impurity's magnetic moment at a quantum critical point leads to a spatial separation of the spin and the charge of impurity. This phenomenon can be interpreted as a spin-charge separation in a 3D system. We show that the induced by impurities Neel order decays only as a power law. Our results show that a quite small concentration of impurities can significantly influence quantum critical properties of a 3D AFM.

In Chapter 4 we perform a phenomenological analysis of various experimental data on CDW phase in cuprates. Analysing nuclear magnetic resonance data we extract an amplitude of the charge density wave in YBCO cuprate. From the analysis of NMR lineshapes we rule out checkerboard pattern of the CDW and conclude that the CDW has stripe-like spatial structure. Relying on the copper and oxygen NMR data we find the amplitudes of s, s' and d-wave components of intra unit cell charge distribution in the CDW. Moreover, analysing the phonon softening data in YBCO, we rule out a wide class of theoretical microscopic models of the CDW in cuprates.

In Chapter 5 we analyse isolated topological defects: skyrmions and merons in a nearly critical two-dimensional frustrated magnet. The critical point separates collinear and spin spiral phases, we disregard quantum fluctuations and consider a classical model of a frustrated magnet. We show that in frustrated magnets metastable topological defects can exist in the absence of external magnetic field. We found that skyrmions in frustrated magnets can attract each other and form exotic configurations with a large topological charge - skyrmion/meron rings. We demonstrate that in the vicinity of the critical point the interaction potential between merons becomes finite at large distances and merons become separable ("deconfined"). The supplementary calculations/details are presented in Appendix 5.7.

Chapter 2

Casimir pairing between fermions at a quantum critical point

In Chapter 2 we consider a novel mechanism for superconducting pairing of fermions near a magnetic quantum critical point. We demonstrate that in two dimensional systems a magnetic quantum criticality results in a strong long range attraction between the fermions. The mechanism of the enhanced attraction is similar to the Casimir effect and corresponds to multi-magnon exchange processes between the fermions. The results presented in the Chapter 2 are quite generic for a wide class of quantum critical systems. The problem is originally motivated by recent establishment of magnetic QCP in hole doped cuprates under the superconducting dome at doping of about 10%. We suggest the mechanism of magnetic critical enhancement of pairing in underdoped cuprates.

2.1 Introduction

In the present Chapter we study interaction between fermions mediated by magnetic fluctuations in a vicinity of a magnetic quantum critical point. To address this generic problem we consider a specific model of two holes injected into the bilayer antiferromagnet. The results presented below demonstrate that critical magnetic fluctuations lead to the long range Coulomb-like attraction between the holes.

Our interest to this problem is motivated by cuprates. Lying at the center of

the debate of high-T_c superconductivity is whether it originates from a Fermi liquid or from a Mott insulator. Recent experimental data including Angle-Resolved Photoemission Spectroscopy (ARPES) support Mott insulator scenario in underdoped cuprates and show transition from a small to large Fermi surface in the hole doping range $0.1 < x < 0.15$, see Refs. [131, 132, 133] Magnetic quantum oscillations (MQO) in underdoped $YBa_2Cu_3O_{6+y}$ also support the small pocket scenario [134], in contrast to the large Fermi surface observed on the overdoped side [135]. Besides that an existence of hole pockets is consistent with the picture of dilute gas of holes dressed by spin fluctuations based on doping a Mott insulator [136].

It is widely believed that superconducting pairing in cuprates is driven by a magnetic mechanism. The most common approach is based on the spin-fermion model in the frame of normal Fermi liquid picture (large Fermi surface). Within this approach electrons interact via exchange of an antiferromagnetic (AF) fluctuation (paramagnon). [137] The lightly doped AF Mott insulator approach, instead, necessarily implies small Fermi surface. In this case holes interact/pair via exchange of the Goldstone magnon. [138] Due to the strong on-site Hubbard repulsion both approaches result in the d-wave pairing of fermions.

Optimally doped and overdoped cuprates do not have any static magnetic order. On the other hand, the underdoped cuprates possess a static incommensurate magnetic order at zero temperature. A magnetic QCP separating these two regions is located at the doping $x \approx 0.1$ (see Chapter 1, Section 1.3.1).

Magnetic criticality can significantly influence superconducting pairing. This idea has been recently considered by Wang and Chubukov [139] in a context of electron doped cuprates. There are also some earlier works referenced in Ref. [140]. However, to the best of our knowledge all the previous works imply a normal liquid with large Fermi surface. This might be a reconstructed Fermi surface which emulates small hole pockets [141], but still in the essence this is a weak coupling normal Fermi liquid like approach. A large Fermi surface to a significant extent reduces importance of the magnetic criticality for the pairing.

In this work we consider two holes injected in the 2D "rigid" Mott insulator, so in our approach implies the small Fermi surface. Using a somewhat intuitive language one can say that there are few holes in this regime and many more virtual

magnons. In this case influence of the magnetic criticality on the coupling between two fermions is the most dramatic and the Casimir bag physics can fully manifest itself. As the Mott insulator host we use the bilayer antiferromagnet with magnetic fluctuations driven by the interlayer coupling. We consider the bilayer model for the sake of performing a controlled calculation. However, we believe that conceptually our conclusions are equally applicable to the single-layer and multi-layer cuprates. The model presented here has only a commensurate magnetic ordering, so we put aside the magnetic incommensurability in underdoped cuprates.

The model under consideration demonstrates a spin-charge separation at the QCP [142]. The term spin-charge separation in this context means a delocalization of the hole spin due to a dressing by a divergent magnon cloud. The effect of spin-charge separation points out to the nontriviality of the pairing problem. We are not aware of any other models of fermion pairing that incorporate physics of spin-charge separation.

In order to probe the interaction between two fermions we consider spin fluctuations in the system, keeping the fermions to be immobile and spatially localized, just as magnetic impurities. In the very end of the Chapter we argue that mobility of fermions does not influence our conclusions, at least as soon as fermion hopping amplitude is sufficiently small. Our calculations show that the single magnon exchange becomes irrelevant close to the QCP. Instead, we obtain strong inter-fermion attraction in the singlet and triplet spin channels due to the Casimir effect [143]. Each of the fermions (holes) builds up a "bag" of quantum magnetic fluctuations. The fermions attract each other, sharing a common bag and reducing the energy of the magnetic fluctuations inside of the bag. A "spin-bag" mechanism of attraction in the antiferromagnetic Neel phase was suggested by Schrieffer, Wen, and Zhang [144] in the context of high-T_c superconductivity. Another mechanism of Casimir magnetic attraction was proposed by Pryadko, Kivelson, Hone [145], but this suggestion is more a "van der Waals magnetic force" than a bag. Our model/mechanism is significantly different from previous suggestions, it is a real bag significantly based on the magnetic criticality. To make the semantics more clear we underline the following points: (i) in the conventional single magnon exchange mechanism there is one magnon per two fermions, (ii) in the van der Waals like Casimir mechanism

there are two magnons per two fermions, (iii) In the bag mechanism there are very many magnons per two fermions. It is worth noting that the spin bag model has conceptual similarity to QCD bag models for nucleon binding such as MIT [146] and chiral bags [147] that have being extensively studied from 1970's till now.

The structure of the Chapter is following. In the Section 5.2 we introduce bilayer $J - J_\perp$ antiferromagnet, which is simple but instructive model and contains all the essential physics of a magnetic criticality. In Section 2.2.1 we characterize magnetic quantum critical point driven by interlayer coupling $J_\perp/J$ and describe magnon excitations for undoped AFM in the disordered phase in the frame of a spin-bond mean field theory. Next, in Section 2.2.2 we move to the hole-doped $J - J_\perp$ model and show how holes interact with magnons. In the Section 2.3, which is the main content of the Chapter, we consider a hole-hole pairing problem at the QCP. Next, we map the original problem defined on the bilayer lattice to a generic quantum field theory model in 2D. In the same Section we show that pairing can not be described in terms of one-magnon exchange. In Section 2.3.1 we develop an effective theory for Casimir interaction of the fermions, considering a double-fermion "atom" which can be either in a singlet or triplet state. In Section 2.3.2 we present results of solution to Dyson's equations for the singlet and triplet Green's functions and finally show how the binding energy in the both spin channels depends on the inter-fermion distance r. Finally, we draw our conclusions in Section 2.4.

2.2 Model

Our model system is $J - J_\perp$ square lattice bilayer Heisenberg antiferromagnet at zero temperature, where magnetic fluctuations are driven by interlayer coupling $J_\perp$ (see Fig. 2.1). The Hamiltonian of the undoped host AF reads

$$\begin{aligned} H_{J,J_\perp} &= J\sum_{\langle i,j\rangle}(\mathbf{S}_i^{(1)}\cdot\mathbf{S}_j^{(1)} + \mathbf{S}_i^{(2)}\cdot\mathbf{S}_j^{(2)}) + \\ & J_\perp\sum_i \mathbf{S}_i^{(1)}\cdot\mathbf{S}_i^{(2)}, \end{aligned} \tag{2.1}$$

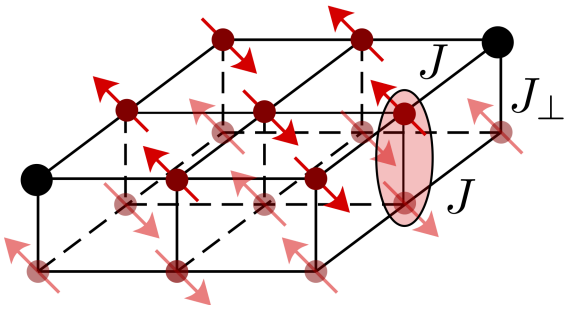

Figure 2.1: Bilayer $J - J_\perp$ antiferromagnet model. Two black dotes on the top layer represent holes.

The superscripts (1), (2) in Eq. (2.1) indicate the layers, $\langle i, j \rangle$ denotes summation over the nearest neighbour sites. Here $\mathbf{S}_i^{(1)} = \frac{1}{2} c_{i\mu,1}^\dagger \boldsymbol{\sigma}_{\mu\nu} c_{i\nu,1}$ is a spin of an electron at site i on the top plane and $c_{i\sigma,1}^\dagger / c_{i\sigma,1}$ is a creation/annihilation operator of an electron with a spin $\sigma = \uparrow, \downarrow$ at site i, $\boldsymbol{\sigma}_{\mu\nu}$ are Pauli matrices. The Hamiltonian describes the antiferromagnetic coupling in the each layer as well as between the two layers. The Hamiltonian $H_{J,J_\perp}$ preserves global $O(3)$ invariance with respect to rotations of spins. It is known that without holes (half-filling) the model has an $O(3)$ magnetic QCP at $J_\perp/J = 2.525$ (see Refs. [148, 149, 150, 151]) separating the AF ordered and the magnetically disordered phase of spin dimers. Note that since we consider zero temperature case, the magnetic ordering in the AF phase is consistent with the Mermin-Wagner theorem. We dope the first layer with two holes. For simplicity we set hopping integrals equal to zero, therefore the holes are immobile. The holes interact with each other via magnetic fluctuations of the spins, i.e. exchanging by magnons.

In subsections 2.2.1 and 2.2.2 of the current section we will briefly present a formalism, which describes magnon excitations and a hole-magnon interaction on the basis of the bilayer model. For more detailed explanations see [142]; a reader which is not interested in these technical details can go directly to the Section 2.3.

2.2.1 Magnons at QCP

Magnetic excitations in the magnetically disordered phase are magnons, which are also in literature called triplons. In the present Chapter we will use terms magnons and triplons as synonyms. To describe the magnons we employ the spin-bond op-

erator mean field technique. This approach has been previously applied to quantum disordered systems such as bilayer antiferromagnets, spin chains, spin ladders, Kondo insulators etc. [155, 156, 157, 152, 153, 154]. It is known [153, 154] that this simple technique gives the position of the QCP at $(J_\perp/J)_c \approx 2.31$, which is close to the exact value $(J_\perp/J)_c = 2.525$ known from Quantum Monte Carlo calculations [148, 149], series expansions [150], and involved analytical calculations with the use of the Brueckner technique [151]. The spin-bond technique being much simpler than the Brueckner technique has sufficient accuracy for our purposes.

The bond-operator representation describes the system in a base of pairs of coupled spins on a rung, which can either be in a singlet or triplet (triplon) state. So, we define the singlet $s_i^\dagger$ and triplet $(t_{ix}^\dagger, t_{iy}^\dagger, t_{iz}^\dagger)$ operators that create a state at site i with spin zero and spin one, which is polarized along one of the axes (x, y, z). The four types of bosons obey the bosonic commutation relations. To restrict the physical states to either singlet or triplet, the above operators are subjected to the constraint

$$s_i^\dagger s_i + \sum_\alpha t_{i\alpha}^\dagger t_{i\alpha} = 1. \tag{2.2}$$

In terms of these bosons, the spin operators in each layer $\mathbf{S}_i^{(1)}$ and $\mathbf{S}_i^{(2)}$ can be expressed as

$$S_{i\alpha}^{(1,2)} = \frac{1}{2}(\pm s_i^\dagger t_{i\alpha} \pm t_{i\alpha}^\dagger s_i - i\epsilon_{\alpha\beta\gamma} t_{i\beta}^\dagger t_{i\gamma}), \tag{2.3}$$

see Ref. [158]. Substituting the bond-operator representation of spins defined in Eq. (2.3) into the $H_{J,J_\perp}$ in Eq. (2.1) we obtain

$$
\begin{aligned}
H_{J,J_\perp} &= H_1 + H_2 + H_3 + H_4, \\
H_1 &= J_\perp \sum_i \left(-\frac{3}{4} s_i^\dagger s_i + \frac{1}{4} t_{i\alpha}^\dagger t_{i\alpha} \right), \\
H_2 &= \frac{J}{2} \sum_{\langle i,j \rangle} (s_i^\dagger s_j^\dagger t_{i\alpha} t_{j\alpha} + s_i^\dagger s_j t_{i\alpha} t_{j\alpha}^\dagger + h.c.), \\
H_3 &= \frac{J}{2} \sum_{\langle i,j \rangle} i\epsilon_{\alpha\beta\gamma} (t_{j\alpha}^\dagger t_{i\beta}^\dagger t_{i\gamma} s_j + h.c.), \\
H_4 &= \frac{J}{2} \sum_{\langle i,j \rangle} (t_{i\alpha}^\dagger t_{j\beta}^\dagger t_{i\beta} t_{j\alpha} - t_{i\alpha}^\dagger t_{j\alpha}^\dagger t_{i\beta} t_{j\beta}).
\end{aligned}
\tag{2.4}
$$

The Hamiltonian (2.4) contains quadratic, cubic and quartic terms in magnon operators t. The most important for us are the quadratic terms, because they provide quantum criticality. The only effect due to the nonlinear terms H_3 and H_4 is a renormalization of parameters near the QCP, such as the position of the QCP, magnon velocity, magnon gap and etc. This does not affect physics at the QCP, and therefore we will neglect these terms in further considerations.

The next step for treating the Hamiltonian (2.4) is to account for the hard-core constraint (2.2). It could be done by introducing an infinite on-site repulsion of triplons; however, this technique is quite involved. Another, more simple, way is to employ a mean-field approach, accounting for the constraint (2.2) via a Lagrange multiplier μ in the Hamiltonian

$$
H_{J,J_\perp} \to H_{J,J_\perp} - \mu \sum_i (s_i^\dagger s_i + t_{i\alpha}^\dagger t_{i\alpha} - 1). \tag{2.5}
$$

Further analysis is straightforward. We replace singlet operators by numbers, $\langle s_i^\dagger \rangle = \langle s_i \rangle = \bar{s}$ (Bose-Einstein condensation of spin singlets); and diagonalize the quadratic in t Hamiltonian by performing the usual Fourier and Bogoliubov transformations

$$
t_{i\alpha} = \sqrt{\frac{1}{N}} \sum_{\boldsymbol{q}} e^{i\boldsymbol{q}\boldsymbol{r_i}} \left(u_q b_{q\alpha} + v_q b_{-q\alpha}^\dagger \right). \tag{2.6}
$$

Here N is the number of spin dimers in the lattice; the diagonalized Hamiltonian reads

$$H_m(\mu, \bar{s}) \;\; = \;\; E_0(\mu, \bar{s}) + \sum_{\boldsymbol{q}} \omega_q b^\dagger_{q\alpha} b_{q\alpha}, \tag{2.7}$$

where $\omega_q = \sqrt{A_q^2 - 4B_q^2}$ and coefficients $A_q = \frac{J_\perp}{4} - \mu + 2J\bar{s}^2\gamma_q$, $B_q = J\bar{s}^2\gamma_q$. Here we define

$$\gamma_q = \frac{1}{2}\left(\cos(q_x) + \cos(q_y)\right). \tag{2.8}$$

The lattice spacing is set to unity. The ground state energy

$$E_0(\mu, \bar{s}) = N\left(-\frac{3J_\perp s^2}{4} - \mu\bar{s}^2 + \mu \right) + \frac{3}{2}\sum_{\boldsymbol{q}} (\omega_q - A_q) \tag{2.9}$$

just shifts energy scale, and therefore is irrelevant for our purposes. The Bogoliubov coefficients u_q and v_q are given by

$$u_q = \sqrt{\frac{A_q}{2\omega_q} + \frac{1}{2}}, \quad v_q = -\mathrm{sign}(B_q)\sqrt{\frac{A_q}{2\omega_q} - \frac{1}{2}}. \tag{2.10}$$

The parameters μ and $\bar{s}$ are determined by the saddle point equations: $\partial E_0(\mu, \bar{s})/\partial\mu = \partial E_0(\mu, \bar{s})/\partial\bar{s} = 0$. Solution to these equations gives position of the QCP at $J_\perp/J = 2.31$ and values of "chemical potential" $\mu = -2.706$ and singlet density $\bar{s} = 0.906$. We see that even at the QCP $\bar{s}$ is close to unity, which again justifies a smallness of the nonlinear terms H_3 and H_4 in the Hamiltonian.

The dispersion of magnons is

$$\omega_k = \sqrt{c^2(\mathbf{k} - \mathbf{Q})^2 + \Delta^2}, \quad \mathbf{Q} = (\pi, \pi), \tag{2.11}$$

in the vicinity of the AFM wave-vector $\boldsymbol{Q}$, here Δ is the magnon gap and c is the velocity of magnons $c = 2J\bar{s}^2 = 1.64J$, where the more precise value is $c = 1.9J$, see Ref. [150]. In the AFM ordered phase the magnons are Goldstone bosons and thus necessarily gapless. On the contrary, in the disordered phase the gap opens up and the spin-bond approach gives $\Delta \propto (J_\perp - J_{\perp,c})$ which is reasonably close to the

prediction for $O(3)$ universality class systems $\Delta \propto (J_\perp - J_{\perp,c})^\nu$ with critical index $\nu = 0.71$ (see Ref. [5]). So the spin-bond method provides a sufficiently accurate description of the QCP.

2.2.2 Hole-magnon interaction

We dope our system with two immobile holes by removing two electrons from the upper plane of the bilayer antiferromagnet. Hence we define the hole creation operator $a^\dagger_{i\sigma}$ with spin projection $\sigma =\uparrow,\downarrow$ by its action on the spin singlet bond $|s\rangle$

$$a^\dagger_{i\uparrow}|s\rangle = c^\dagger_{i\uparrow,2}|0\rangle, \qquad a^\dagger_{i\downarrow}|s\rangle = c^\dagger_{i\downarrow,2}|0\rangle \ , \tag{2.12}$$

where $|0\rangle$ is vacuum. The electron creation/annihilation operator in the upper plane can be expressed in terms of hole creation/annihilation operators $a^\dagger_{i\sigma}/a_{i\sigma}$ (see Ref. [155]), and after substitution in (2.1) it gives following part of the Hamiltonian which describes hole-magnon interaction

$$\begin{aligned} H_{hm} \;\; = \;\; & -\frac{J\bar{s}}{2}\sum_{\langle i,j\rangle}\Big\{(\mathbf{t}_j+\mathbf{t}^\dagger_j)\boldsymbol{\sigma}_i + (\mathbf{t}_i+\mathbf{t}^\dagger_i)\boldsymbol{\sigma}_j\Big\} - \\ & \frac{J}{2}\sum_{\langle i,j\rangle} i(\boldsymbol{\sigma}_i[\mathbf{t}^\dagger_j\times\mathbf{t}_j] + \boldsymbol{\sigma}_j[\mathbf{t}^\dagger_i\times\mathbf{t}_i]). \end{aligned} \tag{2.13}$$

Here $\boldsymbol{\sigma}_i = a^\dagger_{i\mu}\boldsymbol{\sigma}_{\mu\nu}a_{i\nu}$. The first line in the Hamiltonian (2.13) corresponds to a hole-magnon interaction vertex. The terms, describing the hole-double-magnon vertex, which come from the second line of (2.13) will be neglected below, because they are irrelevant in the infrared limit, see Section 2.3 for the explanation of this point. Performing again the standard Fourier and Bogoliubov transformations (2.6) the Hamiltonian (2.13) can be rewritten as

$$H_{hm} \approx \sum_i \sigma^\alpha_i \sum_{\boldsymbol{q}} g_q(b_{q\alpha}e^{i\mathbf{q}\mathbf{r}_i} + b^\dagger_{q\alpha}e^{-i\mathbf{q}\mathbf{r}_i}). \tag{2.14}$$

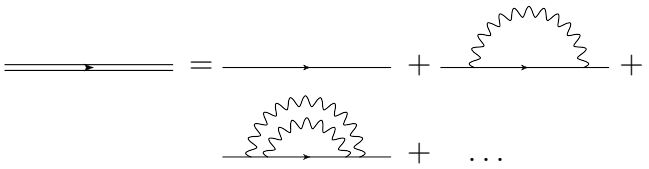

Figure 2.2: Dyson's equation for single hole Green's function in Self-Consistent Born Approximation. Solid and waivy lines correspond to hole and magnon Green's functions.

The hole-magnon vertex is equal to

$$g_q = -\frac{J\bar{s}}{\sqrt{N}}\gamma_q(u_q + v_q). \tag{2.15}$$

Note, that at the QCP the vertex diverges at $\mathbf{q} \to \mathbf{Q} = (\pi, \pi)$, because of the singularity of Bogoliubov coefficients $u_q, v_q \propto 1/\sqrt{\omega_q} \to \infty$.

The divergence of g_q is crucial for the physics of fermion-magnon coupling at the QCP. In fact, it results in the phenomenon of a separation of fermion's spin and charge [142]. The spin of the hole is delocalized in the power-law cloud of magnons where the majority of the spin is concentrated at large distances from the impurity's site. In this sense is separated from the charge of the hole, localized on the hole's site. Later in the Chapter we will show that the infrared divergence of the fermion-magnon coupling at the QCP results in strong power-law attraction between the fermions.

The importance of a spin-charge separation for a single-fermion problem at the QCP could be seen from analysis of analytical structure of the hole Green's function. Standard approach in order to calculate one-fermion Green's function is to use $1/\mathcal{N}$ expansion for the $O(\mathcal{N})$ group, where $\mathcal{N} = 3$ is the number of magnon components. Summation of leading terms in the expansion arises in Self-Consistent Born Approximation (SCBA), see Fig. 2.2.

Calculations of the hole Green's function in the disordered phase in SCBA have been performed in Refs. [64, 65]. The results show that away from the QCP, in the disordered magnetic phase, a quasiparticle pole in the fermion Green's function is separated by Δ from an incoherent part of the Green's function. Furthermore, when approaching to the QCP the Green's function instead of normal pole has only a branch cut. This is a consequence of the infrared singularity of the fermion-magnon

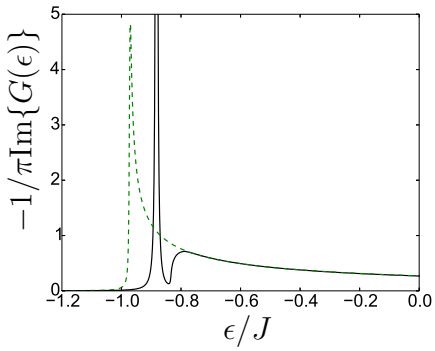

Figure 2.3: Spectral function $-1/\pi\,\mathrm{Im}\{G(\epsilon)\}$ of a single immobile hole obtained in SCBA (see [65]). The green dashed curve corresponds to the QCP ($\Delta = 0$), and the black solid line corresponds to the magnon gap $\Delta = 0.1J$. Note that at the QCP the quasiparticle pole disappears.

coupling constant g_q.

A spectral density of the fermion Green's function (see Fig. 2.3) has an inverse square root behaviour

$$G(\epsilon) \propto 1/\sqrt{\epsilon_0 - \epsilon} \tag{2.16}$$

in the vicinity of the singularity point ϵ_0 and the quasiparticle residue is approaching to zero $Z \propto \sqrt{\Delta}$ at the QCP. Here

$$\epsilon_0 \approx -0.97J \tag{2.17}$$

is the position of the branching point of the Green's function and it has a meaning of fermion energy shift due to interaction with magnons (we set the bare energy of the non-interacting hole to zero).

2.3 Hole-hole interaction, mediated by magnons

Now we are ready to move to the actual problem of a magnon mediated pairing of fermions and demonstrate new results. Adding up magnon Hamiltonian H_m, Eq. (2.7) and hole-magnon interaction Hamiltonian H_{hm}, Eq. (2.14), we arrive to an effective Hamiltonian for two interacting holes, located at the sites with coordinates

$\boldsymbol{r}_1$ and $\boldsymbol{r}_2$,

$$H_{eff} = \sum_{\boldsymbol{q}} \omega_q b^\dagger_{q\alpha} b_{q\alpha} + \sum_{i=1,2} \sigma_i^\alpha \sum_{\boldsymbol{q}} g_q (b_{q\alpha} e^{i\boldsymbol{q}\boldsymbol{r}_i} + b^\dagger_{q\alpha} e^{-i\boldsymbol{q}\boldsymbol{r}_i}). \tag{2.18}$$

The Hamiltonian (2.18) is applicable only if distance between holes $r = |\boldsymbol{r_1} - \boldsymbol{r_2}| > 1$, as long as we put aside direct exchange interaction between the two neighbouring holes.

The effective model (2.18) can be formulated in terms of a quantum field theory. In fact, it is equivalent to the problem of two spin 1/2 fermions coupled to a vector field $\boldsymbol{\phi}(\boldsymbol{r})$, described by $O(3)$-symmetric theory with a Lagrangian

$$\mathcal{L} = \frac{1}{2}(\partial_t \boldsymbol{\phi})^2 - \frac{c^2}{2}(\boldsymbol{\nabla}\boldsymbol{\phi})^2 - \frac{\Delta^2}{2}\boldsymbol{\phi}^2 - \lambda(\boldsymbol{\phi}(\boldsymbol{r}_1)\boldsymbol{\sigma}_1 + \boldsymbol{\phi}(\boldsymbol{r}_2)\boldsymbol{\sigma}_2), \tag{2.19}$$

where λ is the coupling constant of a fermion spin to a magnon field. We focus only on the disordered magnetic phase, and therefore assume $\Delta^2 \geq 0$.

We would like to make three comments concerning techniques and approximations we use in the present work. (i) We use SCBA as the main technical tool. The approximation is justified by the small parameter $1/\mathcal{N}$, where $\mathcal{N} = 3$, corresponding to the $O(3)$ symmetry group. Application of this method to the single impurity problem [65] gives results extremely close to that obtained within more conventional renormalization group approach [64]. (ii) We neglected the self-action of magnons, the term $\propto \boldsymbol{\phi}^4$ is dropped in Eq. (2.19). There is no doubt that the self-action influences the position of the QCP, it also influences the critical index in the gap dependence, $\Delta \propto (J_\perp - J_{\perp,c})^\nu$. However, as soon as we express our answers in terms of Δ the self-action is getting insignificant compared to the noncrossing diagrams accounted within SCBA. It can be illustrated by the single impurity Green's function (2.16), the noncrossing diagrams dramatically reduce the fermion quasiparticle residue from $Z = 1$ to $Z \propto \Delta^{1/2}$, the anomalous dimension is 1/2. On the other hand, the magnon self-action only slightly influences the magnon quasiparticle residue, $Z = 1 \to Z \propto \Delta^\eta$, the anomalous dimension is $\eta = 0.033$ [5]. (iii) We neglect the second line in the interaction (2.13). The simplest way to justfy this is to use the field theory language. In this language the second line has the following

kinematic form, $\boldsymbol{\sigma} \cdot [\boldsymbol{\phi} \times \partial_t \boldsymbol{\phi}]$. Because of the time derivative the term is infrared irrelevant.

Parameters of the Lagrangian (2.19) could be directly expressed via parameters of the initial lattice Hamiltonian (2.1). As an example, the coupling constant λ in (2.19) is related to the hole-magnon vertex g_q in the effective Hamiltonian (2.18) as $g_q = \lambda/\sqrt{2\omega_q}$. Hence, for the Heisenberg bilayer model $\lambda \approx 2J\sqrt{c}$. This equivalence shows, that the problem of fermion pairing at the QCP, we are considering here, is generic. It has implications far beyond the particular bilayer model.

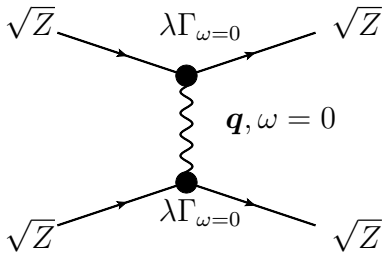

Figure 2.4: One-magnon exchange diagram that provides fermion-fermion interaction potential $V_{int}^{(1)}(\boldsymbol{q})$. Note that a renormalization factor $\sqrt{Z}$ should be referred to each fermion line. Fermion-magnon vertices also come renormalized $\lambda \to \lambda\Gamma_{\omega=0}$.

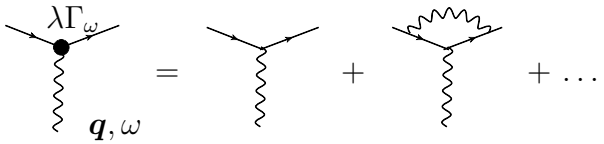

Figure 2.5: The fermion-magnon vertex.

In order to calculate the pairing energy between two fermions we first consider one magnon exchange contribution, Fig. 2.4. According to Feynman rules we obtain the interaction potential

$$V_{int}^{(1)}(\boldsymbol{q}) = -\lambda^2 Z^2 \Gamma_{\omega=0}^2 \frac{\langle \boldsymbol{\sigma}_1 \boldsymbol{\sigma}_2 \rangle}{c^2(\mathbf{q}-\mathbf{Q})^2 + \Delta^2}. \tag{2.20}$$

The factor Z^2 comes from $Z^{1/2}$ for each external fermion line. The vertex $\lambda\Gamma_{\omega=0}$ comes from diagrams in Fig. 2.5, $\lambda \to \lambda\Gamma_{\omega=0}$. Here ω is the frequency of the exchange magnon, which is equal to zero. In the coordinate representation the

potential reads

$$V_{int}^{(1)}(r) = -\frac{\lambda^2}{2\pi c^2} Z^2 \Gamma_{\omega=0}^2 \cos(\boldsymbol{Qr}) \langle \boldsymbol{\sigma}_1 \boldsymbol{\sigma}_2 \rangle K_0 \left(\frac{r\Delta}{c} \right), \tag{2.21}$$

where K_0 is the Macdonald function of zero's order. The potential energy $V_{int}^{(1)}(r) \propto \ln(r)$ is logarithmic at small distances $r < c/\Delta$ and it exponentially decays at $r > c/\Delta$ as $V_{int}^{(1)}(r) \propto e^{-r\Delta/c}$. The spin-dependent prefactor $\langle \boldsymbol{\sigma}_1 \boldsymbol{\sigma}_2 \rangle = 2[S(S+1) - 3/2]$ is determined by the total spin of two fermions S and equals to -3 in the singlet channel and $+1$ in the triplet channel. The potential is attractive in the state with the total spin zero (one) when

$$P_r = \cos(\boldsymbol{Qr}) = (-1)^{r_x + r_y} \tag{2.22}$$

is negative (positive) and repulsive in the opposite case ($\mathbf{r} = r_x \mathbf{e_x} + r_y \mathbf{e_y}$). This fact has a clear physical meaning and reflects AFM character of spin correlations in the antiferromagnet. The system tends to restore AFM ordering and the state when the spins of two interacting holes are aligned according to antiferromagnetic pattern (see Fig. 2.6) is energetically preferable.

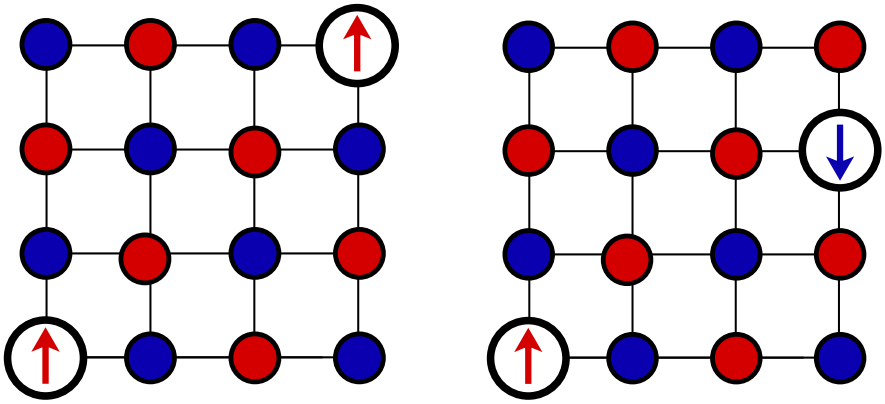

Figure 2.6: Dependence of spin channel which provides attraction between holes on a mutual positioning of the holes in the lattice. Two holes with spins up symbolicaly represent triplet channel which provides negative interaction energy for $P_r = (-1)^{r_x + r_y} = +1$, two holes with opposite spins represent singlet channel which results in attraction when $P_r = -1$.

When we approach the QCP the quasiparticle residue as well as the magnon-hole vertex tends to zero: $Z \propto \sqrt{\Delta} \to 0$ and $\Gamma_{\omega=0} \propto \Delta^{1/6} \to 0$ (see discussion in

Section 2.2.2 and Ref. [65]). Thus the single magnon exchange contribution given by (2.21) vanishes, because the potential $V_{int}^{(1)}$ is proportional to $Z^2\Gamma^2_{\omega=0} \to 0$. Does this imply that the pairing between fermions becomes very weak close to the QCP? Our answer is "no", on the contrary the pairing becomes very strong, but it is due to the Casimir bag mechanism.

Casimir effect attraction has different limits/regimes. The simplest one is the "van der Waals" regime which is relevant to the van der Waals force between two neutral atoms. In this regime the quasiparticle residue remains large, $Z \approx 1$, and the attraction is described by the box diagrams shown in Fig. 2.7; this approach to the effect was developed by Dzyaloshinsky [159]. The number of intermediate magnons is just two, it is equal to the number of fermions. A mechanism of Casimir magnetic attraction between impurities suggested in Ref. [145] for antiferromagnetically ordered phase belongs exactly to this regime. In this phase the fermion's quasipraticle residue is practically unchanged due to the Adler's relation, and the attraction is described by simple box diagrams, see Ref. [61].

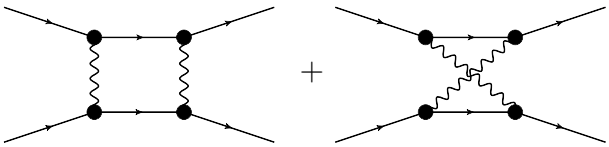

Figure 2.7: The box diagrams for a two-magnon exchange between fermions. Note that the renormalization factor $\sqrt{Z}$ should be referred to each external fermion line.

The diagrams in Figs. 2.4 and 2.7 contain $\sqrt{Z}$ per each external leg. While the presence of $\sqrt{Z}$ is a textbook statement [5], it is important to understand where it comes from. The origin is the quasiparticle description, these diagrams generate effective potentials/interactions between quasiparticles. As soon as the interaction is established, it is used in Schrodinger equation, Lippmann-Schwinger equation, or BCS equation. Obviously, the techniques based on the quasiparticle approach are not applicable in the case when $Z \to 0$ and the spectral weight becomes fully incoherent. To the best of our knowledge the only known technique which does not refer to quasiparticles is Bethe-Salpeter equation (BSE) which operates with two-fermion Green's function with amputated legs. Unfortunately all known applications of BSE, for example binding of positronium [160], in the end assume quasipraticles

with nonzero residue. While in principle the BSE approach is applicable to our problem, all our attempts to apply the method were unsuccessful because of a large number of two-fermion irreducible diagrams with multiple magnon exchanges.

To solve the Casimir bag problem we have developed a new diagramatic method which we call the "Lamb-shift" technique. Similar to BSE in the "Lamb-shift" technique we also operate with two-fermion Green's function. The advantage of BSE is that it is generic and in principle it is independent of the large parameter $\mathcal{N}$. On the other hand, the "Lamb-shift" technique is the large $\mathcal{N}$ expansion by construction. The advantage of the "Lamb-shift" technique is that it allows us to solve the multi-magnon problem.

2.3.1 The "Lamb shift" technique for calculation of Casimir interaction

In this section we introduce a new technique to treat Casimir pairing energy. To incorporate "Casimir effect" physics, we consider a composite two-fermion "atom", which has the total spin either zero (singlet state) or one (triplet state). Next, we calculate "Lamb shift" in energy of this composite "atom" due to radiation of magnons as a function of separation between fermions.

Let's consider effective theory for the composite object. Creation operator for singlet state is

$$\Psi_S^\dagger = \frac{1}{\sqrt{2}}(a_{1\uparrow}^\dagger a_{2\downarrow}^\dagger - a_{1\downarrow}^\dagger a_{2\uparrow}^\dagger) \tag{2.23}$$

and for triplet state

$$\begin{aligned}
\Psi_{T,x}^\dagger &= \frac{-1}{\sqrt{2}}(a_{1\uparrow}^\dagger a_{2\uparrow}^\dagger - a_{1\downarrow}^\dagger a_{2\downarrow}^\dagger), \\
\Psi_{T,y}^\dagger &= \frac{i}{\sqrt{2}}(a_{1\uparrow}^\dagger a_{2\uparrow}^\dagger + a_{1\downarrow}^\dagger a_{2\downarrow}^\dagger), \\
\Psi_{T,z}^\dagger &= \frac{1}{\sqrt{2}}(a_{1\uparrow}^\dagger a_{2\downarrow}^\dagger + a_{1\downarrow}^\dagger a_{2\uparrow}^\dagger).
\end{aligned} \tag{2.24}$$

According to the selection rules for interaction of the "atom" with a magnon, there are three types of transitions $S \to T_\alpha$, $T_\alpha \to T_\beta$ and $T_\alpha \to S$, where S means singlet state and T_α denotes triplet state with polarization α. The only possible invariant

kinematic structure that provides coupling between S and T,α states with emission (absorption) of one magnon is $\left\{g_{ST}(q)\Psi^{\dagger}_{T,\alpha}\Psi_S(b_{q\alpha}+b^{\dagger}_{q\alpha})+h.c.\right\}$. In similar way, transition of the type $T_\alpha \to T_\beta$ is governed by the term $ig_{TT}(q)\varepsilon_{\alpha\beta\gamma}\Psi^{\dagger}_{T,\alpha}\Psi_{T,\beta}(b_{q\gamma}+b^{\dagger}_{q\gamma})$. The coefficients $g_{ST}(q)$ and $g_{TT}(q)$ are coupling constants for these transitions. Therefore, the interaction of two-fermion system with a magnon field in the singlet-triplet representation reads

$$\begin{aligned}\mathcal{H} &= \left\{\delta_{\alpha\beta}\Psi^{\dagger}_{T,\alpha}\Psi_S\sum_{\boldsymbol{q}} g_{ST}(q)(b_{q\beta}+b^{\dagger}_{q\beta})+h.c.\right\}+ \\ & i\varepsilon_{\alpha\beta\gamma}\Psi^{\dagger}_{T,\alpha}\Psi_{T,\beta}\sum_{\boldsymbol{q}} g_{TT}(q)(b_{q\gamma}+b^{\dagger}_{q\gamma}).\end{aligned} \tag{2.25}$$

The effective vertices can be calculated by evaluating matrix elements of the Hamiltonian (2.18) between states (2.23), (2.24) :

$$\begin{aligned} g_{ST}(q) &= g^{*}_{TS}(q) = 2ig_q\sin\left(\frac{\boldsymbol{qr}}{2}\right), \\ g_{TT}(q) &= 2g_q\cos\left(\frac{\boldsymbol{qr}}{2}\right). \end{aligned} \tag{2.26}$$

Let us define a retarded Green's function for the singlet and triplet state

$$\begin{aligned} G_{T,\alpha\beta}(t_2-t_1) &= -i\langle 0|\Psi_{T,\beta}(t_2)\Psi^{\dagger}_{T,\alpha}(t_1)|0\rangle\theta(t_2-t_1), \\ G_S(t_2-t_1) &= -i\langle 0|\Psi_S(t_2)\Psi^{\dagger}_S(t_1)|0\rangle\theta(t_2-t_1), \end{aligned} \tag{2.27}$$

where $|0\rangle$ is a ground state of the system and theta-function is

$$\theta(t) = \begin{cases} 1,\ t>0; \\ 0,\ t<0. \end{cases} \tag{2.28}$$

Due to the $O(3)$ rotational invariance the triplet Green's function should be of the form $G_{T,\alpha\beta}(t)=\delta_{\alpha\beta}G_T(t)$. Note that our definition of the Green's functions $G_S(t_2-t_1)$, $G_T(t_2-t_1)$ assumes that the fermions, which constitute the composite "atom", are both created at the same moment of time t_1 and then both annihilated at the moment t_2. Apart from several other technical details the creation/annihilation at the same time is the major difference of our technique from BSE. Fourier transform

of Eq. (2.27) gives the Green's functions in the frequency representation

$$G_{S,T}(\epsilon) = \int_0^\infty dt e^{i(\epsilon+i0)t} G_{S,T}(t) \ . \tag{2.29}$$

Dyson's equations for singlet and triplet state Green's functions read

$$G_{S,T}(\epsilon) = \frac{1}{\epsilon - \Sigma_{S,T}(\epsilon) + i0}. \tag{2.30}$$

We use SCBA to evaluate singlet and triplet self-energy

$$\begin{aligned} \Sigma_S(\epsilon) =& 3\sum_{\boldsymbol{q}} |g_{ST}(q)|^2 G_T(\epsilon - \omega_q), \\ \Sigma_T(\epsilon) =& \sum_{\boldsymbol{q}} |g_{ST}(q)|^2 G_S(\epsilon - \omega_q) + 2\sum_{\boldsymbol{q}} |g_{TT}(q)|^2 G_T(\epsilon - \omega_q). \end{aligned} \tag{2.31}$$

The diagrams for the singlet and triplet self-energies are presented in Fig. 2.8. The combinator factors here come from contraction of the corresponding tensor structures of the coupling vertices in (2.25) and have a meaning of the number of the polarizations of an intermediate state.

Note, that unlike the scattering amplitude (2.20), expressions (2.31) for the two-fermion self-energy do not contain single-fermion quasiparticle residues. Similar to the one-fermion problem, the residue of the composite "atom" Green's function is zero at the QCP. However, it is not a problem now, because we are interested only in the position of singularity of the Green's function, i.e. in two-fermion pairing energy.

Note also, that the Dyson's equations (2.30), (2.31) for the two-fermion system include processes when the fermions are dressed by magnons, as well as the processes with (multi-)magnon exchanges between the fermions. Therefore, the "Lamb shift" approach implicitly accounts for the incoherent part of single-fermion Green's, that is crucial in the vicinity of the QCP.

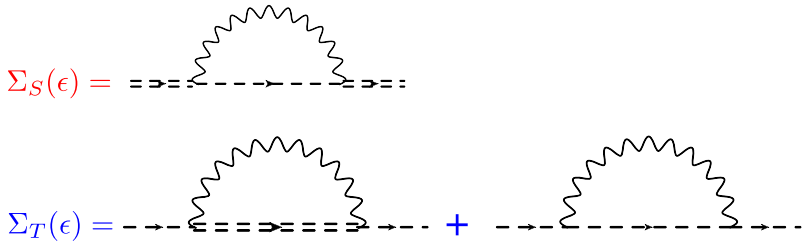

Figure 2.8: Diagrams for singlet $\Sigma_S(\epsilon)$ and triplet $\Sigma_T(\epsilon)$ self-energies in SCBA. Double dashed line and dashed line represent double-fermion Green's function in singlet and triplet channels correspondingly. Analytical expressions for the diagrams are given in Eq. (2.31).

2.3.2 The hole-hole interaction potential

In order to find interaction energy of two fermions, we numerically solve the system of two Dyson's equations (2.31) in the square Brillouin zone for different inter-fermion separations r, measured in units of lattice spacings. Energy grid in our computation is $\Delta\epsilon = 10^{-3}J$. The zero's order approximation for the Green's function is $G^{(0)}_{S,T}(\epsilon) = 1/(\epsilon + i0)$ and for artificial broadening we take $+i0 \to i10^{-3}J$. In order to perform a numerical integration in equations (2.31) we can directly integrate over the square Brillouin zone, or introduce an effective momentum cutoff and integrate analytically over the azimuthal angle in the momentum space and then integrate over radial component of the momentum $|\boldsymbol{q}'| = |\boldsymbol{q} - \boldsymbol{Q}| \leq \Lambda_q \approx 1$ numerically. We have checked that there is a good agreement between these two methods. However, the effective momentum cutoff method is much more efficient for numerics and provides better precision of the computations, therefore we employed the later approach for our calculations.

The limit $r \to \infty$ of infinite separation between the fermions corresponds to the case, when the vertices in the equations (2.31) are substituted by the averaged ones over q oscillations $|g_{ST}(q)|^2, |g_{TT}(q)|^2 \to 2|g_q|^2$. The position of a singularity of the triplet and singlet Green's functions gives us the energy E_∞ of the two-fermion system separated by an infinite distance. It is clear that in such limit the Green's functions in both spin channels should coincide $G_S(\epsilon) = G_T(\epsilon)$ which guarantees the same value for the asymptotic energy E_∞ in the singlet and triplet states. So, we refer interaction energy as a difference $V_{int}(r) = E(r) - E_\infty$.

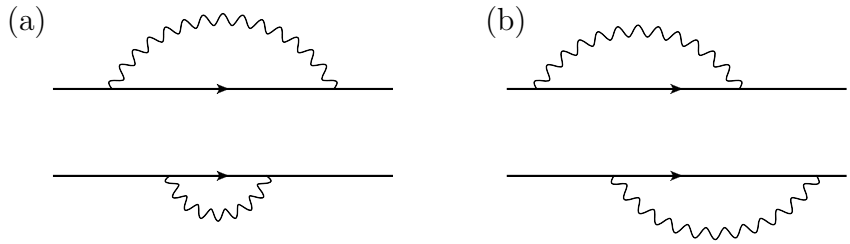

Figure 2.9: Diagrams contributing to E_∞. Top and bottom solid line correspond to single hole Green's function. Diagram (a) is accounted in SCBA (2.31), diagram (b) is not included in (2.31) and corresponds to $1/\mathcal{N}$ correction to SCBA.

We found that the value $E_\infty \approx -1.55J$ (at the QPC) is about 20% smaller compared to a doubled energy of an isolated single hole $2\epsilon_0 \approx -1.94J$, see Eq. (2.17). This difference is due to the fact that certain diagrams, which are presented in SCBA for the single hole Green's function, are not included in SCBA for the two hole Green's function $G_{S,T}$ (see Fig. 2.9). This deviation shows precision of our method, which can be improved by calculating $1/\mathcal{N}$ corrections to SCBA (2.31).

As it is clear from the structure of effective vertices

$$\begin{aligned} |g_{ST}(q)|^2 &= 2g_q^2(1 - P_r \cos \boldsymbol{q'r}), \\ |g_{TT}(q)|^2 &= 2g_q^2(1 + P_r \cos \boldsymbol{q'r}), \end{aligned} \tag{2.32}$$

the system's behaviour greatly depends on the "parity" $P_r = (-1)^{r_x+r_y}$ of the inter-fermion distance. The holes prefer to form a singlet (triplet) spin state for negative (positive) "parity" P_r at given r.

First, let us consider the case, when the system is away from the QCP, $\Delta > 0$. We plot spectral functions

$$A_{S,T}(\epsilon) = -\frac{1}{\pi} \operatorname{Im}\{G_{S,T}(\epsilon)\} \tag{2.33}$$

for the singlet and triplet Green's functions at different r, see Fig.2.10 (a, b). We see a well defined quasiparticle peak in the triplet (singlet) spin channel at $r = 4$ ($r = 5$). However, in the opposite spin channel the peak broadens and submerges to continuum. This effect can be interpreted as a formation of an excited decaying state, which coupled via magnons to the ground state.

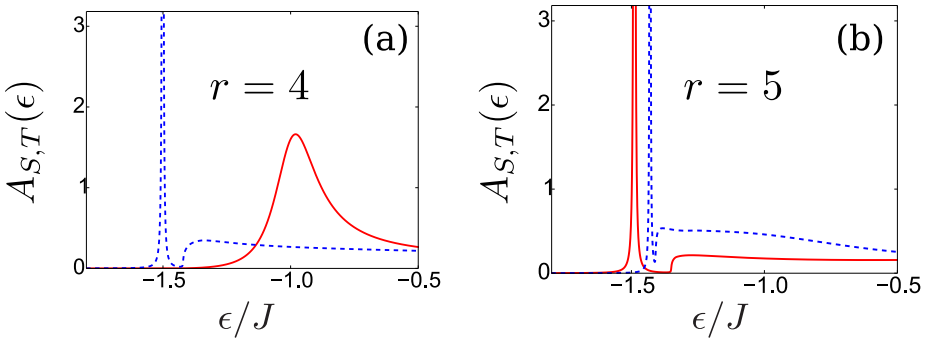

Figure 2.10: Spectral functions $A_S(\epsilon)$, $A_T(\epsilon)$ of double-fermion Green's functions in the singlet and triplet channels close to the QCP ($\Delta = 0.08J$). Panel (a) corresponds to the inter-hole distance $r = 4$ and (b) corresponds to $r = 5$. Blue dashed lines correspond to the triplet state, red solid lines correspond to the singlet state.

In Fig. 2.11 we plot the fermion-fermion interaction energy versus distance. The inset displays the interaction energy when the system is away from the QCP (the magnon gap is large, $\Delta = 0.67J$). Squares and triangles show results of our "Lamb-shift" technique calculations and solid lines represent the single magnon exchange formula (2.21). There is an excellent agreement between the two approaches. The main part of Fig. 2.11 shows the same quantities, but close to the QCP (the magnon gap is small, $\Delta = 0.08J$). Here we observe a dramatic disagreement between the result of the "Lamb-shift" technique and the single magnon exchange potential (2.21). The single magnon exchange approximation fails in the vicinity of the QCP.

Let us now consider the most interesting case of pairing between fermions at the QCP ($\Delta = 0$). As in the case of a single fermion at the QCP, the Green's functions $G_S(\epsilon)$ and $G_T(\epsilon)$ have just power-law cuts, instead of quasiparticle peaks, with a branching point $E = E(r)$, see Fig. 2.12 (a, b). The position $E(r)$ of the branching point gives the ground state energy of the system. The spin channel of the ground state is specified by the spin state in which the Green's function is singular at $E(r)$. The state, in which the Green's function is not singular, corresponds to a decaying state. The imaginary part of the both singlet and triplet Green's functions emerges at the same branching point $E(r)$ for any fixed r (see Fig. 2.12). This is due to transitions between these states with an emission of a soft magnon with $\omega_q \to 0$. In the Fig. 2.12 (b) we see a distinct discontinuity of the both singlet and triplet spectral functions at the same branching point $E(r)$. In the Fig. 2.12 (a)

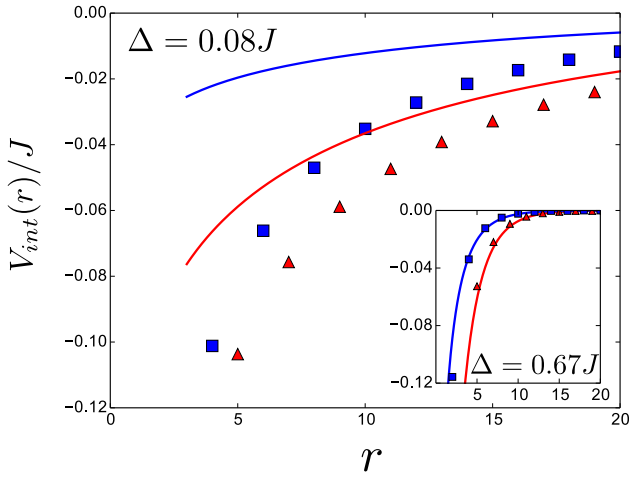

Figure 2.11: Interaction energy of two holes $V_{int}(r)$ at finite magnon gaps as a function of inter-hole distance r. Red trangles and blue squares show the results of the "Lamb shift" technique in the singlet and triplet state. Red and blue solid lines represent theoretical prediction from one-magnon exchange mechanism (2.21) for the singlet and triplet channels. The main plot corresponds to a small magnon gap ($\Delta = 0.08J$), the inset corresponds to a large magnon gap ($\Delta = 0.67J$).

the branching points are also coincide, but the singlet spectral function has a small spectral weight in the vicinity of the branching point.

Our results for the interaction energy $V_{int}(r)$ at the QCP as a function of distance r, obtained within the "Lamb shift" technique, are presented in Fig. 2.13. We see from the data that the interaction between two fermions is attractive, when the "parity" P_r is negative (positive), see Fig. 2.6. The binding becomes stronger at smaller inter-fermion distances r. The interaction energy has a power-law form

$$\boxed{V_{int}(r) = -a/r^{\alpha}, \quad \alpha \approx 0.75} \tag{2.34}$$

with a prefactor $a \approx 0.3J$, where α and a are found from the least-square fit of our numerical data. The values for the prefactor a and the exponent α are slightly different for singlet ($a = 0.3J$, $\alpha = 0.76$) and triplet ($a = 0.33J$, $\alpha = 0.74$) cases. The variations of the values of a and α are negligible within the accuracy of our calculations.

In the inset in Fig. 2.13 we show $V_{int}(r)$ which includes vertex corrections to SCBA (2.31). Leading in $1/\mathcal{N}$ corrections for the singlet and triplet self-energy $\delta\Sigma_S$

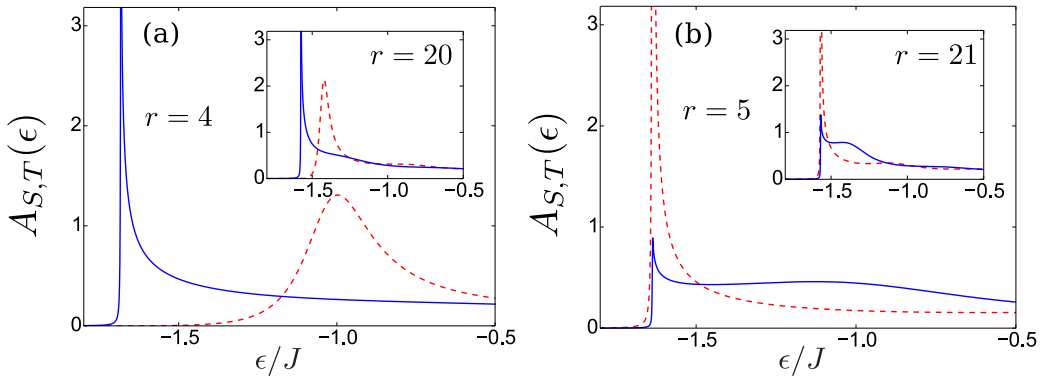

Figure 2.12: Spectral functions $A_S(\epsilon)$, $A_T(\epsilon)$ of double-fermion Green's functions in singlet and triplet channels at the QCP ($\Delta = 0$). On the panel (a) the main plot corresponds to inter-hole distance $r = 4$, the inset plot to $r = 20$. On the panel (b) the main plot corresponds to $r = 5$, the inset plot corresponds to $r = 21$. Red solid lines show singlet state, blue dashed lines show triplet state.

and $\delta\Sigma_T$ are presented in the supplementary Section 2.3.3 (see diagrams in Fig. 2.14 and formulas (2.35), (2.36)). These corrections increase the binding energy by about 20%, leaving the critical index α almost unchanged. Thus we conclude that corrections in $1/\mathcal{N}$ to SCBA do not change qualitative and quantitative picture given by SCBA.

From our calculations we observe very strong long-range attraction between fermions in the vicinity of the QCP. We clearly see that one magnon exchange contribution to the interaction energy vanishes at the QCP. On the contrary, accounting for multi-magnon exchange processes we obtain significant binding in singlet and triplet channels. We calculate the attraction energy due to multi-magnon exchange processes as a "Lamb shift" of energy of a two fermion "atom" due to emission of multiple magnons. The fermions interact, sharing common "bag" of magnetic fluctuations and reducing energy of fluctuations inside of the "bag". Therefore, the physics of inter-fermion attraction in the vicinity of the QCP is due to "Casimir bag" mechanism.

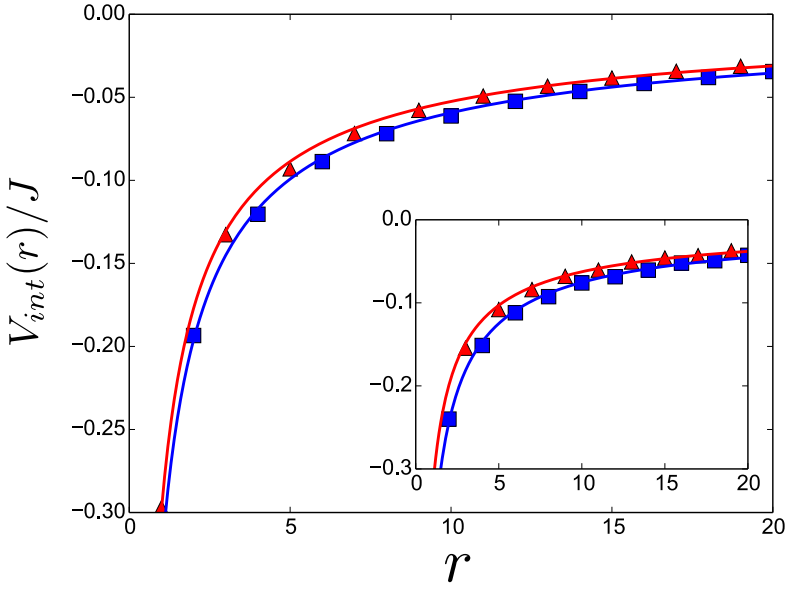

Figure 2.13: Interaction energy $V_{int}(r)$ of two holes at the QCP, $\Delta = 0$. Red trangles and blue squares show the results of the "Lamb shift" technique for the singlet and triplet state. Red and blue solid lines represent power-law fits $V_{int}(r) = -a/r^{\alpha}$ for the singlet and triplet channel. The main plot corresponds to SCBA, in the inset we represent $V_{int}(r)$, which includes the first $1/\mathcal{N}$ correction to the SCBA. The exponent for all curves is approximately $\alpha \approx 0.75$.

2.3.3 Leading $1/\mathcal{N}$ corrections to SCBA for two-fermion Green's function

Let us consider $1/\mathcal{N}$ corrections to the self-energies $\Sigma_S(\epsilon)$ and $\Sigma_T(\epsilon)$, calculated in Self-Consistent Born Approximation (see Eqs. (2.31)). In order to do this we account for vertex corrections $\delta\Sigma_S(\epsilon)$ and $\delta\Sigma_T(\epsilon)$ to self-energies obtained in SCBA, corresponding diagrams are shown in Fig. 2.14. The vertex correction to the singlet self-energy reads

$$\delta\Sigma_S(\epsilon) = 3\sum_{\boldsymbol{q},\boldsymbol{k}} |g_{ST}(q)|^2 |g_{ST}(k)|^2 G_{T,q} G_{T,k} G_{S,qk} - 6\sum_{\boldsymbol{q},\boldsymbol{k}} g_{ST}(q) g^*_{ST}(k) g_{TT}(k) g^*_{TT}(q) G_{T,q} G_{T,k} G_{T,qk}. \tag{2.35}$$

The combinator factors come from contractions of the corresponding tensor structures of the effective vertices in Eq. (2.25). In the similar way the vertex correction

to the triplet self-energy is given by

$$\delta\Sigma_T(\epsilon) = \sum_{\boldsymbol{q},\boldsymbol{k}} |g_{ST}(q)|^2 |g_{ST}(k)|^2 G_{S,q} G_{S,k} G_{T,qk} - 2\sum_{\boldsymbol{q},\boldsymbol{k}} g_{TT}(q) g^*_{TT}(k) g^*_{ST}(q) g_{ST}(k) G_{T,q} G_{T,k} G_{S,qk} + 2\sum_{\boldsymbol{q},\boldsymbol{k}} |g_{TT}(q)|^2 |g_{TT}(k)|^2 G_{T,q} G_{T,k} G_{T,qk}. \tag{2.36}$$

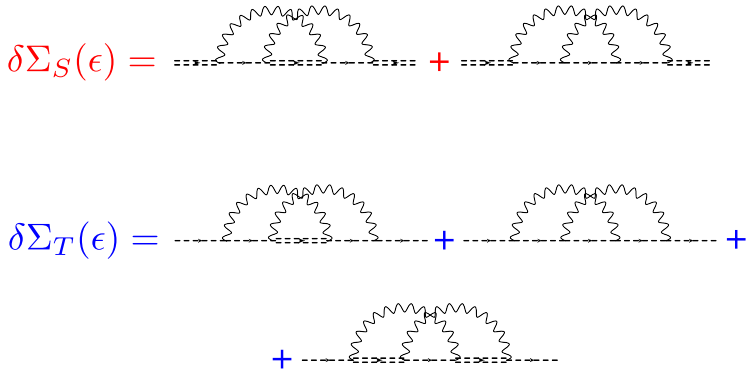

Figure 2.14: Diagrams for the leading $1/\mathcal{N}$ corrections $\delta\Sigma_S(\epsilon)$ and $\delta\Sigma_T(\epsilon)$ (a) to singlet and (b) to triplet self-energies. Double dashed line and dashed line represent two-fermion Green's function in singlet and triplet channels correspondingly.

Here we are using shorten notations $G_{n,q} = G_n(\epsilon - \omega_q)$, $G_{n,k} = G_n(\epsilon - \omega_k)$ and $G_{n,qk} = G_n(\epsilon - \omega_q - \omega_k)$ for singlet and triplet Green's functions ($n = S, T$). One can check that in the limit $r \to \infty$ the correction $\delta\Sigma_S$ will be suppressed by the factor $1/\mathcal{N} = 1/3$ with respect to $\Sigma^{(2\,loop)}_{S,T}$ calculated in SCBA within two loop approximation.

The relative shift of binding energy, calculated with and without vertex correction, does not exceed 20%. It can be considered as a confirmation of applicability of $1/\mathcal{N}$ expansion for the effective "'Lamb shift" theory described by the Hamiltonian (2.25).

2.3.4 Influence of mobility of fermions

How mobility of fermions influences the considered mechanism? We do not have a full answer to this question yet. However, we do understand that the mobility does not influence the Casimir bag mechanism as soon as the fermion hopping amplitude

is sufficiently small. The fermion hopping influences the dynamics in two ways, (i) It leads to additional terms in the fermion-magnon vertexes (2.15) and (2.26), (ii) Hopping leads to a fermionic kinetic term in the Hamiltonian (2.18).

(i) The hole-magnon vertex with an account of hoppings has been calculated in Ref. [142]. An important point is that the hopping induced term in the vertex has an additional power of the momentum transfer compared to the term considered in the present work. Therefore, the hopping induced term is infrared *irrelevant* and hence, as it has been demonstrated in Ref. [142], hopping does not influence the spin-charge separation at the QCP. For the same reason the hopping induced term in the vertex does not influence the magnon bag Casimir attraction.

(ii) Kinetic energy of the fermions, which is quadratic in the momentum of the fermion, is suppressed at small momenta comparing to linear magnon kinetic term, and therefore is negligible at the QCP [142, 161]. However, the fermion mobility imposes limitations on the time formation of the magnon bag. To address this issue we distinguish the nearest neighbour hopping t and the next nearest neighbour hopping t'. The hopping t leads to mixing between singlet and triplet pairing channels and therefore the effect of this hopping requires a special analysis. However, the hopping t' does not lead to such mixing. Therefore, in a model with the following hopping parameters, $t = 0$, $t' \neq 0$, and with hopping less then the depth of the potential $V_{int}(r)$: $t' < 0.3J$ the binding problem is very simple. One has to solve Lippmann-Schwinger equation with kinetic energy due to t' and with the attraction given by Eq. (2.34). Obviously the solution gives a strong binding. Of course the set of parameters, $t = 0$, $t' \neq 0$, and $t' < 0.3J$, is not the most physically interesting one. However, the example demonstrates that in principle mobility is consistent with the Casimir bag mechanism.

2.4 Conclusions

In conclusion, we considered an interaction between two spin 1/2 fermions embedded in a two dimensional antiferromagnetic system at the QCP, which separates ordered and disordered magnetic phases. As a model system we study bilayer antiferromagnet at $T = 0$ with two injected holes, in which magnetic criticality is driven by

interlayer coupling. We have shown that in the vicinity of the QCP the interaction between fermions can not be described by simple one-magnon exchange, unlike the case when the system is away from the QCP. The interaction mechanism is similar to Casimir effect and is due to multi-magnon exchange processes. To incorporate features of Casimir physics we developed a new approach, which we call a "Lamb shift" technique. We considered composite two-fermion "atom" and calculated it's energy shift ("Lamb shift") provided by radiation of magnons. We found strong attraction between the fermions in spin singlet and triplet states depending on the "parity" of the inter-fermion distance r, which is positive (negative) for even (odd) r. Positive (negative) "parity" corresponds to attraction in triplet (singlet) channel. The attractive potential has power-law form $V_{int}(r) \propto -1/r^{\alpha}$ with the exponent $\alpha \approx 0.75$.

We suppose that our work sheds light on the influence of magnetic criticality on fermion pairing mediated by magnons. We also believe that our results are conceptually applicable to underdoped cuprates.

Chapter 3

Impurity problem in a 3D antiferromagnet at quantum critical point

In the present Chapter we consider a Kondo-like problem of an impurity in the vicinity of a quantum critical point. More specifically we study magnetic screening of an impurity spin in 3D quantum critical antiferromagnets. We calculate the spatial distribution of a magnetization induced by the impurity and show that quantum criticality results in the complete screening of the local impurity's magnetic moment. Our results show the existence a spin-charge separation in two and three dimensional systems at quantum critical point.

3.1 Introduction

Quantum critical phenomena is an extensively developing subject in modern condensed matter physics, in both theoretical and experimental frontiers.[162] The most vivid manifestations of quantum phase transitions (QPT) arise in low-dimensional systems such as cuprates and iron pnictides. However, quantum critical behaviour is also found in three-dimensional (3D+time) systems. A well-known example of a 3D compound with a magnetic quantum critical point (QCP) is $TlCuCl_3$.[163] Under normal conditions the material is in the magnetically disordered phase, while

pressure drives QPT to the antiferromagnetically ordered Neel phase.

Quantum critical properties of a system can be significantly influenced by the presence of impurities. For instance, substitution of Cu atoms in the parent compound $TlCuCl_3$ with low concentration of nonmagnetic Mg impurities creates an uncompensated spin 1/2 at the sites of the impurities, which induces magnetization around the impurities and can even lead to the formation of a long-range magnetic order in the macroscopic volume of the crystal. [164] In the magnetically disordered phase the magnetization cloud around each impurity exponentially decays over a few lattice spacings away from the impurity. But in the vicinity of the QCP the effect of impurity-induced magnetization can be notably enhanced. Experimental observations reveal an interplay between the impurity-induced staggered magnetization and a quantum criticality near the QCP. [56, 57, 58]

Despite of the vast amount of theoretical work on the impurity-induced magnetization in quasi-1D and 2D systems (see Refs. [165, 51, 68, 64, 66] and references therein), we are not aware of similar studies in the relation to 3D materials. In the present Chapter we consider a single impurity with spin S embedded in a 3D antiferromagnet (AFM), which is close to the QCP, separating the magnetically disordered and magnetically ordered phases. Conceptually the problem is similar to the Kondo effect (see e.g. [166, 167, 168]) since, as we show below, the spin cloud screens the impurity's spin at the QCP. While sometimes this phenomenon is called Bose-Kondo effect [169], it is significantly different from usual Kondo problem, for instance there are no mobile fermions in our case. In the present work we study spatial distribution of the nonlocal spin density and the staggered magnetization induced by the impurity using effective field theory formalism. We show that, when approaching the QCP from the disordered phase, the spin density around the impurity decays as $\propto 1/r^3$ with logarithmic corrections and the total spin accumulated in the delocalized cloud is equal to S. We also demonstrate that the induced staggered magnetization decays as $\propto 1/r$.

Closely related to the problem of impurity-induced spin density and impurity-induced Neel order is a phenomenon of spin-charge separation (SCS). The conventional definition of SCS relies on the existence of two quasiparticles carrying spin and charge ("spinon" and "holon"), which is the case in 1D Tomonaga-Luttinger

liquid of strongly interacting electrons. [170, 171]. In contrast, there are no known systems with SCS in higher spatial dimensions in the conventional definition. However, a partial SCS exists in 2D models such as hole-doped AFM [173, 174, 175, 176]. Furthermore, the recent research [177] reports pronounced SCS in the vicinity of the magnetic QCP. In the latter case, the precise meaning of SCS is different from SCS in Tomonaga-Luttinger liquid. A hole creates a spin cloud around the itself with a radius which diverges at the QCP. As a result the delocalized impuritiy's spin becomes spatially separated from the impurity's charge pinned to the impurity's site; this basically means SCS. In the present Chapter we show that such SCS also occurs in 3D systems near the QCP.

The Chapter is organized in the following way. In Section 3.2 we introduce an effective field theory describing a 3D AFM doped with a single impurity in the vicinity of the QCP. Considering the interaction of the doped AFM with a probe magnetic field, we introduce an operator of the spin density and explain how we calculate induced spin density. Here we also provide a method of calculation of the staggered magnetization around the impurity. The rest of the Chapter is divided into two parts, which correspond to the two techniques of the calculations: Self-Consistent Born Approximation (SCBA) and Renormalization Group (RG) approach in $3+1$ dimensions. Section 3.3 refers to the calculation of the spin density in SCBA for the most physically interesting case of the impurity with spin $S = 1/2$. In Section 3.4 we calculate the impurity-induced nonlocal spin density, the local spin of the impurity and the staggered magnetization using RG technique. We also consider a semiclassical limit of an impurity with a large spin. We draw our conclusions in Section 3.4.4.

3.2 Effective Theory

An example of a 3D lattice model which incorporates main features of magnetic quantum criticality is presented in Fig. 3.1. The model corresponds to a cubic lattice AFM consisting of spins $S = 1/2$ at each site with weak J bonds and strong J' bonds. The system has a QCP driven by parameter $g = J'/J$ and located at $g_c = 4.013$, which separates the disordered magnetic phase of spin dimers at $g > g_c$

from the Neel phase at $g < g_c$. [178, 179] This lattice model describes various properties of $TlCuCl_3$ near the pressure-driven QCP in zero and non-zero magnetic fields. [178]

Substitution of a $S = 1/2$ Cu^{2+} ion with a spinless Zn^{2+} in $TlCuCl_3$ creates an impurity (vacancy), see Fig. 3.1. The effective spin of the impurity is $S = 1/2$. The vacancy in the lattice induces a nonlocal magnetization cloud around the impurity's site. In the present Chapter we will calculate spatial distribution of the spin density and the staggered magnetization in the spin cloud around the impurity.

Magnetic properties of the critical system are determined by low-energy magnetic excitations. The magnetic excitations are magnons in the Neel phase and triplons in the paramagnetic phase. Hereafter we refer to the both types of quasiparticles as "magnons". Effective theory, which describes magnons in the vicinity of the QCP is based on the following Lagrangian, see e.g. [5]:

$$\mathcal{L}_M = \frac{(\partial_t \boldsymbol{\phi})^2}{2} - \frac{(\nabla_i \phi_\mu)^2}{2} - \frac{\Delta_0^2 \boldsymbol{\phi}^2}{2} - \frac{\alpha_0 (\boldsymbol{\phi}^2)^2}{4!}\,, \tag{3.1}$$

where $\phi_\mu = (\phi_x, \phi_y, \phi_z)$ is the magnon field, $\Delta_0^2 \propto g - g_c$ is the magnon gap (squared), α_0 is a four-magnon coupling constant, ∂_t is the time derivative, $\nabla_i = \partial/\partial r_i$ is the three-dimensional gradient. Hereafter we set the Plank constant and magnon speed equal to unity $\hbar = c = 1$. In the disordered magnetic phase $\Delta_0^2 > 0$. Near the QCP the magnon gap $\Delta_0 \to 0$.

The Lagrangian (3.1) contains quadratic terms as well as quartic term $\propto \phi^4$, describing the magnon self-action. The magnon self-action results in the renormalization of the magnon gap Δ_0 in the Lagrangian (3.1). From one-loop RG calculations [5] it follows that in the disordered phase the evolution of the renormalized gap is given by

$$\Delta^2 \propto \Delta_0^2 \left[\ln \frac{C(\Lambda)}{g - g_c} \right]^{-\frac{N+2}{N+8}}\,, \tag{3.2}$$

where $N = 3$ in the present case of the $O(3)$ universality class system, and $C(\Lambda)$ is a positive constant determined by an ultraviolet scale Λ. Besides that, the ϕ^4 term leads to renormalization of magnon quasiparticle residue. [5] However, the change of the residue appears only in the two-loop renormalization group and therefore is

small. Hence, for our purposes we drop out the self-action term from the Lagrangian (3.1) and substitute the bare magnon gap to the renormalized value $\Delta_0 \to \Delta$.

The Lagrangian describing the "Berry phase" dynamics of a non-interacting spin-S impurity reads

$$\mathcal{L}_{imp} = i\left(\psi^\dagger(\boldsymbol{r},t)\partial_t\psi(\boldsymbol{r},t) - \left(\partial_t\psi^\dagger(\boldsymbol{r},t)\right)\psi(\boldsymbol{r},t)\right), \tag{3.3}$$

where ψ is the $2S+1$ component spinor. Hereafter we set the energy of the non-interacting impurity to zero. The impurity-magnon interaction term in the magnetic disordered phase reads [64]

$$\mathcal{L}_{int} = -\frac{\lambda}{S}\,\psi^\dagger(\boldsymbol{S}\cdot\boldsymbol{\phi})\psi\,, \tag{3.4}$$

where λ is the coupling constant, $\boldsymbol{S} = (S_x, S_y, S_z)$ are the operators of the impurity's spin acting in the $(2S+1)$-dimensional Hilbert space.

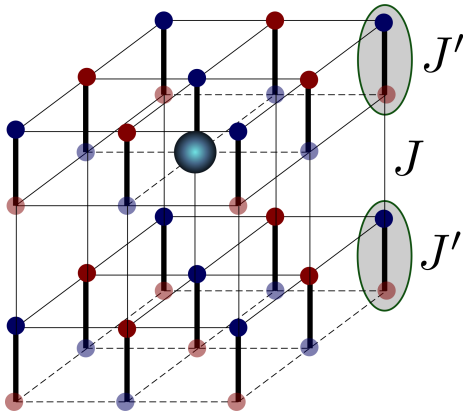

Figure 3.1: An example of a lattice model for 3D AFM with $O(3)$ QCP. Spins $S = 1/2$ located at each site. Thin lines denote weak J bonds and thick lines denote strong J' bonds. A quantum phase transition between the Neel and the dimerized paramagnetic phases occurs at $(J'/J)_c = 4.013$. [178, 179] The big blue sphere represents an impurity (hole) introduced into the lattice.

The impurity-magnon coupling creates a nonlocal spin density $\boldsymbol{s}(\boldsymbol{r})$ around the impurity. In order to find $\boldsymbol{s}(\boldsymbol{r})$ we use the Lagrangian of interaction of the system

with an external magnetic field (see, e.g. [205])

$$\mathcal{L}_B = -\left(\partial_t \boldsymbol{\phi} \cdot [\boldsymbol{B} \times \boldsymbol{\phi}]\right) + \frac{[\boldsymbol{B} \times \boldsymbol{\phi}]^2}{2} + \psi^\dagger \left(\boldsymbol{S} \cdot \boldsymbol{B}\right) \psi \,, \tag{3.5}$$

where we have set $\mu_B g = 1$. Note that Eq. (3.5) is still valid if the magnetic field $\boldsymbol{B}$ is non-uniform. In the contrast to the majority of previous works, where $\boldsymbol{B}$ is considered uniform, the non-uniformity of the probe magnetic field is crucial for the derivations presented in the present Chapter. Terms linear in $\boldsymbol{B}$ terms in the Lagrangian (3.5) provide following expression for spin density:

$$\boldsymbol{s}(\boldsymbol{r}) = \langle \frac{1}{2} \left([\boldsymbol{\phi} \times \partial_t \boldsymbol{\phi}] + \text{h.c.}\right) + \psi^\dagger \boldsymbol{S} \psi \rangle \; = \boldsymbol{s}_{nl}(\boldsymbol{r}) + \boldsymbol{S}_{imp} \delta(\boldsymbol{r}). \tag{3.6}$$

The brackets $\langle \cdots \rangle$ denote an averaging over the ground state of the system. The term $1/2\langle [\boldsymbol{\phi} \times \partial_t \boldsymbol{\phi}] + \text{h.c.} \rangle$ in Eq. (3.6) is the nonlocal part of the spin density $\boldsymbol{s}_{nl}(\boldsymbol{r})$, induced by the impurity. The subscript "nl" stands hereafter for "nonlocal". The term $\langle \psi^\dagger \boldsymbol{S} \psi \rangle$ in Eq. (3.6) corresponds to the local spin $\boldsymbol{S}_{imp}$ at the impurity's site.

In addition to the spin density we will consider the staggered magnetization induced by the impurity. Writing down the Euler-Lagrange equation for the magnon field operator $\boldsymbol{\phi}$ from the action $\int dt d^3r \, \{\mathcal{L}_M + \mathcal{L}_{int}\}$ and taking expectation value of the result we obtain Yukawa-like form of the staggered magnetization

$$\langle \boldsymbol{\phi}(\boldsymbol{r}) \rangle = -\lambda \frac{e^{-\Delta r}}{4\pi r} \frac{\boldsymbol{S}_{imp}}{S}. \tag{3.7}$$

At the QCP the exponent in Eq. (3.7) is close to unity and $\langle \phi(r) \rangle \propto 1/r$. The prefactor is determined by the expectation value of local spin at the impurity's site $\boldsymbol{S}_{imp}$.

In the rest of the Section we explain the technique of our calculations of the induced spin density and the staggered magnetization. In order to find the impurity-induced spin density we proceed as follows. The impurity-induced spin density can be defined as

$$\boldsymbol{s}(\boldsymbol{r}) = \left. \frac{\delta \epsilon_B}{\delta \boldsymbol{B}(\boldsymbol{r})} \right|_{\boldsymbol{B}=0}, \tag{3.8}$$

where ϵ_B is the shift of the ground state energy due to the probe magnetic field

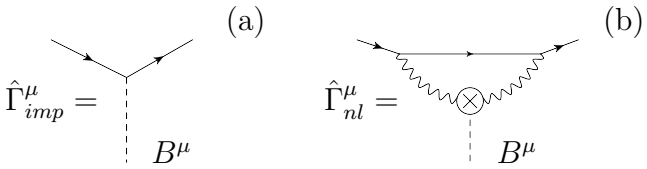

Figure 3.2: Example of diagrams for a coupling between a probe magnetic field $\boldsymbol{B}$ and (a) an impurity spin and (b) nonlocal spin density. The solid lines correspond to a bare ($\lambda = 0$) impurity Green's function, the wavy line represents magnon, dashed line represents probe magnetic field $\boldsymbol{B}$. The cross on the magnon line corresponds to the magnon-$\boldsymbol{B}$ vertex, provided by the term $\boldsymbol{B}[\boldsymbol{\phi} \times \dot{\boldsymbol{\phi}}]$ in the Lagrangian is (3.5).

$\boldsymbol{B}(\boldsymbol{r}') = \boldsymbol{B}\delta(\boldsymbol{r}' - \boldsymbol{r})$.

The ground state energy ϵ_g of the system is the position of a singularity of the retarded impurity's Green's function $\hat{G}_B(\epsilon)$ and can be found from the Dyson's equation

$$\hat{G}_B^{-1}(\epsilon) = \epsilon - \hat{\Sigma}(\epsilon) - B^{\mu}\hat{\Gamma}^{\mu}(\epsilon, \boldsymbol{r}) = 0\,, \tag{3.9}$$

where $\hat{\Sigma}(\epsilon)$ is the self-energy of the impurity at zero magnetic field, $\hat{\Gamma}^{\mu}(\epsilon, \boldsymbol{r})$ is the vertex function, corresponding to the interaction of the system with the probe magnetic field. Note that in Eq. (3.9) we need to keep only linear in B^{μ} terms. From rotational symmetry properties the only possible "kinematic" structure of the vertex

$$\hat{\Gamma}^{\mu}(\epsilon, \boldsymbol{r}) = \Gamma(\epsilon, \boldsymbol{r})\hat{S}^{\mu}/S. \tag{3.10}$$

The vertex function can be split into local and nonlocal parts

$$\hat{\Gamma}^{\mu}(\epsilon, \boldsymbol{r}) = \begin{cases} \hat{\Gamma}^{\mu}_{imp}(\epsilon), & \boldsymbol{r} = 0, \\ \hat{\Gamma}^{\mu}_{nl}(\epsilon, \boldsymbol{r}), & \boldsymbol{r} \neq 0. \end{cases} \tag{3.11}$$

Calculating the shift ϵ_B of the position of the singularity in the Green's function $\hat{G}_B(\epsilon)$ due to the probe magnetic field and using the formula (3.8) we find the local and nonlocal components of spin density $\boldsymbol{s}(\boldsymbol{r})$ as well as the staggered magnetizaton 3.7. The spin density $\boldsymbol{s}(\boldsymbol{r}) = \boldsymbol{e}s(r)$ and the staggered magnetization $\langle\boldsymbol{\phi}(\boldsymbol{r})\rangle = \boldsymbol{e}\langle\phi(r)\rangle$ are directed along the impurity's spin $\boldsymbol{S}_{imp} = \boldsymbol{e}S_{imp}$ ($\boldsymbol{e}$ is a unit vector), and due to spatial isotropy of the system depend only on $r = |\boldsymbol{r}|$.

Below in we consider the spin density/staggered magnetization distribution using

two approaches: Self-Consistent Born Approximation (Section 3.3) and Renormalization Group (Section 3.4).

3.3 Self-Consistent Born Approximation

The standard approach for calculation of a single-fermion Green's function is $1/N$ expansion for $O(N)$ group, where $N = 3$ is the number of magnon components. Summation of leading terms in the $1/N$ expansion ("rainbow" type diagrams, see Fig. 2.2) results in the Self-Consistent Born Approximation (SCBA). We will apply the SCBA to the case of $S = 1/2$ impurity only. As it will be demonstrated in Section 3.4.4, for larger impurity spins ($S > 1/2$) the corrections to impurity-magnon vertex disregarded in SCBA become relevant. Therefore, in the latter case SCBA fails and application of RG technique is necessary.

3.3.1 "Dressed" Green's function of the impurity

In order to proceed with the calculations of the impurity-induced spin density, we first find Green's function of the impurity "dressed" by critical magnons at zero magnetic field. The system at $\boldsymbol{B} = 0$ possesses $O(3)$ rotational invariance and therefore is proportional to the identity matrix in the spin space $\hat{G}(\epsilon) = G(\epsilon)$. The Dyson's equation for the impurity's Green's function is graphically represented in Fig. 2.2. The analytical form of the equation reads:

$$G(\epsilon) = \frac{1}{\epsilon - \Sigma(\epsilon) + i0}, \tag{3.12}$$

where the impurity's self-energy is given by following expression:

$$\begin{aligned} \hat{\Sigma}(\epsilon) &= \lambda^2 \int \frac{id\omega}{2\pi} \sum_{\boldsymbol{q}} \sigma^\mu \hat{G}(\epsilon - \omega) D_{\mu\nu}(\omega, \boldsymbol{q}) \sigma^\nu = \\ & 3 \sum_{\boldsymbol{q}} M_{\boldsymbol{q}}^2 \hat{G}(\epsilon - \omega_{\boldsymbol{q}}) . \end{aligned} \tag{3.13}$$

Here $\omega_{\boldsymbol{q}} = \sqrt{\Delta^2 + \boldsymbol{q}^2}$ is the magnon dispersion, $M_{\boldsymbol{q}} = \lambda/\sqrt{2\omega_{\boldsymbol{q}}}$ is the matrix element corresponding to emission of a magnon with momentum $\boldsymbol{q}$ by the impurity and

$D_{\mu\nu}(\omega, \boldsymbol{q}) = \delta_{\mu\nu}/(\omega^2 - \omega_{\boldsymbol{q}}^2 + i0)$ is the magnon propagator. We expressed spin 1/2 operators via Pauli matrices $S^\mu = \sigma^\mu/2$. The combinatorial factor 3 in Eq. (3.13) comes from the summation over the intermediate polarization states of a magnon.

The sum over momentum $\boldsymbol{q}$ in Eq. (3.13) logarithmically diverges at large $|\boldsymbol{q}|$, therefore we have to introduce an ultraviolet cutoff Λ. The parameter Λ depends on a particular realisation of the system and can be estimated as inverse lattice spacing in the host AFM.

The solution to Dyson's equation (3.12) near the QCP ($\Delta \to 0$) has the following form

$$G^{-1}(\epsilon) = (\epsilon - \epsilon_0 + i0)\sqrt{1 + \frac{3\lambda^2}{2\pi^2} \ln\left(\frac{\Lambda}{\epsilon_0 + \Delta - \epsilon - i0}\right)}. \tag{3.14}$$

Formula (3.14) is valid in the vicinity of the singularity point $\epsilon_0 \approx -3\Lambda\lambda^2/4\pi^2$ and obtained within a logarithmic accuracy, i.e. assuming that $\ln\left(\frac{\Lambda}{\epsilon_0+\Delta-\epsilon}\right) \gg 1$.

The Green's function (3.14) has a nontrivial analytic structure. The quasiparticle pole at $\epsilon = \epsilon_0$ is separated by the gap Δ from the incoherent part of the Green's function. At the QCP the magnon gap closes ($\Delta \to 0$), hence the quasiparticle pole and the branching point singularity are merging. A similar analytical structure of a fermion's (impurity's) Greens function has been discussed in Chapter 2 in the context of fermion-fermion pairing in 2D critical systems. The quasiparticle residue of the impurity Green's function $G(\epsilon)$ vanishes in the vicinity of the QCP

$$Z = \left(1 - \frac{\partial\Sigma(\epsilon_0)}{\partial\epsilon}\right)^{-1} = \frac{1}{\sqrt{1 + \frac{3\lambda^2}{2\pi^2}\ln\left(\frac{\Lambda}{\Delta}\right)}}\Bigg|_{\Delta\to 0} \to 0. \tag{3.15}$$

The vanishing quasiparticle residue is an indication of the impurity-induced spin cloud delocalization and implies SCS. [177]

A typical value of the impurity-magnon coupling constant λ can be estimated from the lattice model shown in Fig. 3.1. Bond-operator mean-field theory calculations [181] result in the value of the effective coupling constant $\kappa = 3\lambda^2/2\pi^2 \sim 0.5$, appearing in front of the logarithm in formula (3.14). Therefore, the logarithmic corrections are significant in the vicinity of the QCP.

The analytical result (3.14) for the impurity Green's function can be directly compared with a numerical solution of the Dyson's equation (3.12); corresponding

plots for the analytical and numerical spectral functions $-1/\pi\,\mathrm{Im}\{G(\epsilon)\}$ are presented in Fig. 3.3. An artificial broadening $i0 \to i2.5 \times 10^{-3}\Lambda$ is introduced in the numerical procedure and in analytical formula (3.14). We see an excellent agreement between the numerical and the analytical results.

Let us make a comment on the validity conditions of the SCBA for the results of the present Section, and all following results, which will be derived in Sections 3.3.2 and 3.3.3. Formally, SCBA relies only on a $1/N$ expansion of the $O(N)$ group, independently on the value of the coupling constant λ. SCBA is applicable for arbitrary λ, in contrast to RG method, which works only for small λ. We will return to this discussion later, in the Section 3.4.1.

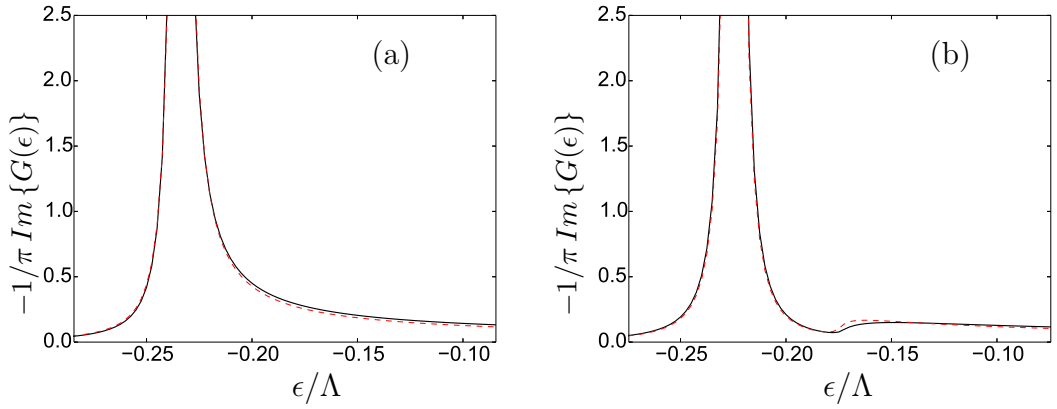

Figure 3.3: The spectral function of $S = 1/2$ impurity obtained in SCBA. Panel (a) corresponds to the QCP ($\Delta = 0$); panel (b) corresponds to magnon gap $\Delta = 0.05\Lambda$. The effective coupling constant is set to $\kappa = 0.6$. The solid black line corresponds to the impurity's Green's function, calculated numerically and the red dashed line corresponds to the analytical formula (3.14). Note that on the panel (a) the position of pole and branching point are merging.

3.3.2 Induced spin density

The nonlocal spin density induced by the impurity at distances $r > 0$ can be calculated based on the "probe magnetic field" approach, described in Section 3.2. In the present Section we follow this approach and develop a self-consistent diagrammatic technique that allows us to compute $s_{nl}(r)$ in the regime of strong impurity-magnon coupling.

First, let us substitute the Green's function pole position $\epsilon_g = \epsilon_0 + \epsilon_B$ into Eq. (3.9), expand it in ϵ_B up to the first order and use Eq. (3.8). The result reads

$$s_{nl}(r) = Z\Gamma_{nl}(\epsilon_0, r)\,. \tag{3.16}$$

The leading perturbative contribution to the vertex function $\hat{\Gamma}^{\mu}_{nl} \sim \mathcal{O}(\lambda^2)$ is represented by the Feynman diagram shown in Fig. 3.2 (b). The analytical expression for the diagram is following

$$\hat{\Gamma}^{\mu}_{nl}(\epsilon, r) = \Gamma_{nl}(\epsilon, r)\sigma^{\mu} = \int \frac{id\omega}{2\pi} \sum_{\boldsymbol{q},\boldsymbol{k}} (\lambda\sigma^{\varkappa})\, \hat{G}_0(\epsilon - \omega)$$
$$\left(\lambda\sigma^{\beta}\right) D_{\varkappa\nu}(\omega, \boldsymbol{k}) \left[-2i\omega\, \varepsilon_{\mu\nu\alpha}\, e^{i(\boldsymbol{q}-\boldsymbol{k})\boldsymbol{r}}\right] D_{\beta\alpha}(\omega, \boldsymbol{q})\,, \tag{3.17}$$

where $\hat{G}_0(\epsilon) = 1/(\epsilon + i0)$ is the bare retarded Green's function of a non-interacting impurity. The expression in square brackets corresponds to the magnon - probe magnetic field vertex, which we show in Fig. 3.2, (b) as a circle with a cross inside. The leading order approximation 3.17 completely ignores effects of impurity "dressing" by a magnon cloud and multi-magnon processes, which are important in the vicinity of the QCP.

The SCBA equation for vertex $\hat{\Gamma}^{\mu}_{nl}(\epsilon, r)$, which accounts for multi-magnon processes, is graphically represented in Fig. 3.4. The analytical form of the equation reads

$$\Gamma_{nl}(\epsilon, r) = \Gamma^{(0)}_{nl}(\epsilon, r) -$$
$$\sum_{\boldsymbol{q}} M_q^2 G^2(\epsilon - \omega_q)\Gamma_{nl}(\epsilon - \omega_q, r), \tag{3.18}$$

where $\Gamma^{(0)}_{nl}(\epsilon, r)$ corresponds to the first term in the r.h.s. of the diagrammatic equation in Fig. 3.4:

$$\Gamma^{(0)}_{nl}(\epsilon, r) = 2\lambda^2 \sum_{\boldsymbol{q},\boldsymbol{k}} e^{i(\boldsymbol{q}-\boldsymbol{k})\boldsymbol{r}} \frac{G(\epsilon - \omega_q) - G(\epsilon - \omega_k)}{\omega_q^2 - \omega_k^2}\,. \tag{3.19}$$

Expressions (3.18) and (3.19) were obtained by performing integration over ω in the rhs of the original SCBA equation, shown in Fig. 3.4. The factor (-1) in Eq. (3.18) comes from the algebraic identity for Pauli matrices $\sigma^\mu\sigma^\nu\sigma^\mu = -\sigma^\nu$. Formula (3.19) follows from (3.17), where the bare impurity Green's function is substituted by the "dressed" Green's function $G(\epsilon)$, shown in Fig. 2.2.

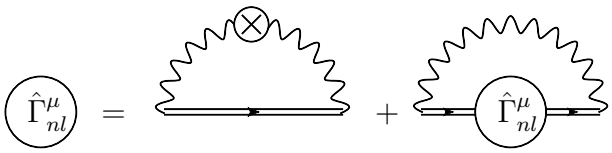

Figure 3.4: Diagrammatic equation for "nonlocal" vertex function $\hat{\Gamma}^{\mu}_{nl}$.

The solution of the self-consistent integral Eq. (3.18) together with the quasiparticle residue Z obtained from numerical solution of Dyson's equation (3.12), provide all necessary ingredients for the spin-density, see Eq. (3.16). We solve numerically Eq. (3.18) for the vertex $\Gamma_{nl}(\epsilon, r)$ and compute Z using the numerical solution of Eq. (3.12). Solution to Eq. (3.18) has been found iteratively, we start the iterations from the $\Gamma_{nl}(\epsilon, r) = \Gamma^{(0)}_{nl}(\epsilon, r)$. The results of the calculation of the spin density $s_{nl}(r)$ for different values of the magnon gap Δ and coupling constant λ are presented in Fig. 3.5.

For the purpose of computational efficiency we use the spherical cutoff $|\boldsymbol{q}|, |\boldsymbol{k}| \leq \Lambda$ in integrals in Eq. (3.18) and (3.19), instead of integrating over a cubic Brillouin zone. This cutoff scheme resultes in significant r-oscillations in the induced spin-density $s_{nl}(r)$, where the period of oscillations is $r \sim 1/\Lambda$ and the amplitude of the oscillations decays with increasing r. It is clear that these oscillations are by-products of the rigid spherical cutoff and will be notably suppressed if one performs proper 3D-integration over the cubic Brillouin zone. Hence, in Fig. (3.5) we plot numerical data for the spin-density averaged over the period of the oscillations.

Our numerical calculations show that the starting approximation $\Gamma^{(0)}_{nl}(\epsilon, r)$ for the vertex function and the solution $\Gamma_{nl}(\epsilon, r)$ of the SCBA equation (3.18) are very close to each other. Therefore, we use $\Gamma^{(0)}_{nl}$ instead of Γ_{nl} in order to obtain an analytical approximation for the nonlocal spin density. Substituting (3.19) in Eq.

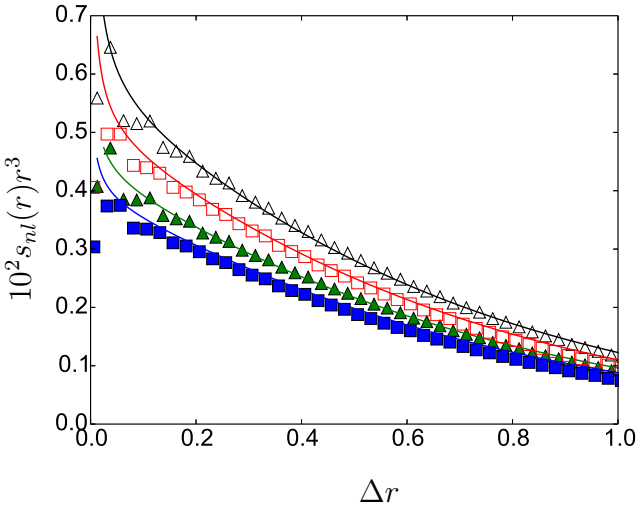

Figure 3.5: Spin density $s_{nl}(r)$ (multiplied by r^3) induced by $S = 1/2$ impurity as a function of the dimensionless distance $y = \Delta r$. Calculations are performed in the SCBA. The points represent numerical results for different values of magnon gap and effective coupling constant $\kappa = 3\lambda^2/2\pi^2$. The squares correspond to $\Delta = 6.25 \times 10^{-3}\Lambda$, triangles correspond to $\Delta = 1.25 \times 10^{-2}\Lambda$; filled markers represent $\kappa = 0.3$, open markers correspond to $\kappa = 0.6$. The solid line is the analytical approximation (3.20).

(3.16) and using formula (3.14) for the impurity's Green's function, we find

$$\boxed{s_{nl}(r) = \frac{\lambda^2 \Delta}{4\pi^3 \sqrt{1 + \frac{3\lambda^2}{2\pi^2} \ln \frac{\Lambda}{\Delta}} \sqrt{1 + \frac{3\lambda^2}{2\pi^2} \ln \Lambda r}} \frac{K_1(2\Delta r)}{r^2}.} \tag{3.20}$$

Here $K_1(x)$ is the Macdonald function of the first kind. At the distances $1/\Lambda < r < 1/\Delta$ using the expansion of the Macdonald function $K_1(x) \to 1/x$ at $x \to 0$, we obtain power-law asymptotics for the spin density with logarithmic corrections:

$$s_{nl}(r) \to \frac{\lambda^2}{8\pi^3 r^3} \frac{1}{\sqrt{\left(1 + \frac{3\lambda^2}{2\pi^2} \ln \frac{\Lambda}{\Delta}\right)\left(1 + \frac{3\lambda^2}{2\pi^2} \ln \Lambda r\right)}}. \tag{3.21}$$

At large distances $r > 1/\Delta$ the spin density (3.20) is exponentially suppressed: $s_{nl}(r) \propto e^{-2\Delta r}/r^{5/2}$. In Fig. (3.5) solid lines correspond to the analytical result given by Eq. (3.20). One can see an excellent agreement between the analytical and the numerical results.

The net spin of the system, which is given by the sum of the local impurity's

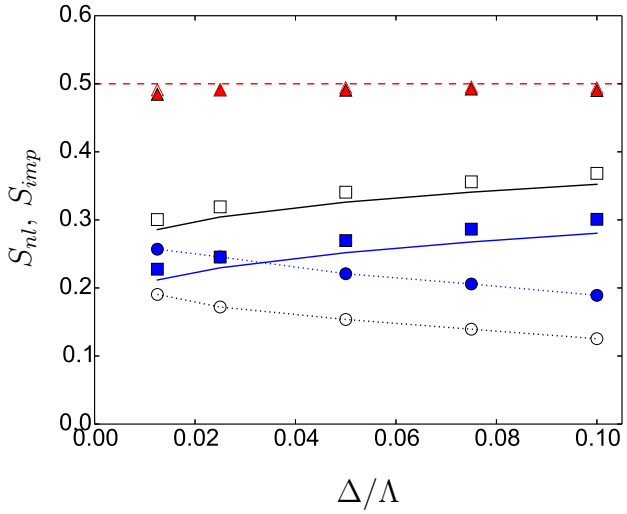

Figure 3.6: Integral nonlocal spin S_{nl} and local spin of the imputity S_{imp} as a function of the magnon gap Δ in SCBA. Full and open markers correspond to values of effective coupling constant $\kappa = 0.6$ and $\kappa = 0.3$. Circles correspond to S_{nl}, squares represent S_{imp} and triangles show the net spin $S_{nl} + S_{imp}$. Solid lines are theoretical predictions for the local impurity's spin S_{imp}, given by Eq. (3.25). Dotted lines are visual guides for S_{nl}. Red dashed line corresponds to the net spin equal to 1/2.

spin and spin of the nonlocal cloud, is conserved and must equal to $S = 1/2$. The integral spin corresponding to the nonlocal spin density

$$S_{nl} = \int d^3 r s_{nl}(r) \tag{3.22}$$

as a function of Δ/Λ is depicted in Fig. 3.6. We use the numerical results for $s_{nl}(r)$, shown in Fig. 3.5, in order to obtain S_{nl}. According to Fig. 3.6 and Eq. (3.20) the integral nonlocal spin S_{nl} increases with decreasing Δ. Moreover, the impurity's spin $S_{imp} = 1/2 - S_{nl} \to 0$ vanishes at the QCP, as we will demonstrate in Section 3.3.3. Therefore, the integral nonlocal spin $S_{nl} \to 1/2$ at the critical point. We will return to this discussion in Section 3.4.2.

3.3.3 Local spin of the impurity and staggered magnetization

In order to calculate the impurity's spin, localized at $\boldsymbol{r} = 0$, we use a similar approach to what we have used in the previous section. We introduce the local magnetic field $\boldsymbol{B}(\boldsymbol{r}) = \boldsymbol{B}\delta(\boldsymbol{r})$ and calculate energy shift of the impurity due to the magnetic field. The result for the impurity's spin reads

$$S_{imp} = \frac{Z}{2}\Gamma_{imp}(\epsilon)\Big|_{\epsilon=\epsilon_0}. \tag{3.23}$$

The diagrammatic equation for the vertex function $\hat{\Gamma}^{\mu}_{imp}(\epsilon) = \Gamma_{imp}(\epsilon)\sigma^{\mu}$ in the SCBA has the graphical representation shown in Fig. 3.7. The corresponding analytical

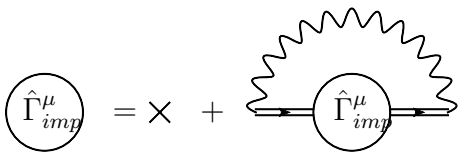

Figure 3.7: Diagrammatic equation for the "local" vertex function $\hat{\Gamma}^{\mu}_{imp}$. The cross represents the bare vertex $\Gamma^{(0)}_{imp} = 1$.

form of the equation, represented in Fig. 3.7, is

$$\Gamma_{imp}(\epsilon) = 1 - \sum_{\boldsymbol{q}} M^2_{\boldsymbol{q}} G^2(\epsilon - \omega_{\boldsymbol{q}})\Gamma_{imp}(\epsilon - \omega_{\boldsymbol{q}})\,. \tag{3.24}$$

Solving equation (3.24) and substituting the solution in to Eq. (3.23) we obtain spin of the impurity with logarithmic accuracy

$$S_{imp} = \frac{1}{2\left(1 + \frac{3\lambda^2}{2\pi^2}\ln\frac{\Lambda}{\Delta}\right)^{2/3}}. \tag{3.25}$$

We also calculate the residual spin of the impurity, numerically solving Eq. (3.24). Both analytical and numerical results for S_{imp} at different values of the parameters Δ and λ are shown in Fig. 3.6. We see good agreement between the analytical and the numerical results. From Fig. 3.6 we can notice that the impurity's spin logarithmically tends to zero when we approach to the QCP, $\Delta \to 0$. In Fig. 3.6 we

also show the net spin $S_{imp} + S_{nl}$ for different values of Δ and λ.

Results of our calculations presented in Eq. (3.21), Eq. (3.25) and also in Figs. 3.5, 3.6 show that at the QCP the local spin is approaching zero and the spin of the system is accumulated in the nonlocal spin cloud. This delocalized spin cloud around the impurity has a size proportional to the inverse magnon gap $r \simeq 1/\Delta$, and therefore significant part of impurity's spin is separated from charge localized at $r = 0$. The discussion on spin-charge separation is also presented in the Section 3.4.2.

The net spin of the system equals to 1/2. This is an exact statement and can be demonstrated at the diagrammatic level. One can trace mutual cancellations of the quantum corrections to the impurity's spin and integral spin of nonlocal cloud in every order in λ. Corrections to the impurity's spin S_{imp} are cancelled by the corrections to integral spin S_{nl}. The numerical results for the net spin of the system presented in Fig. 3.6 are consistent with the conservation of spin.

Using Eq. (3.7) and Eq. (3.25) we obtain following expression for the staggered magnetization induced by the spin 1/2 impurity

$$\langle \phi(r) \rangle = -\lambda \frac{e^{-\Delta r}}{4\pi r} \frac{1}{\left(1 + \frac{3\lambda^2}{2\pi^2} \ln \frac{\Lambda}{\Delta}\right)^{2/3}}. \tag{3.26}$$

Away from the QCP the staggered magnetization induced by the impurity is exponentially small. In the vicinity of the QCP the prefactor in Eq. (3.26) becomes logarithmically suppressed, however the staggered magnetization decays only as $\langle \phi(r) \rangle \propto 1/r$.

3.4 The Renormalization Group approach in D=3+1

In this Section we calculate nonlocal and local components of the spin density using one-loop RG technique in $3+1$ dimensions. In the RG approach the coupling constant λ becomes dependent on the energy scale. Since $D = 3+1$ is the upper critical dimension, the evolution of the running coupling constant is logarithmic. It leads to logarithmic corrections to s_{nl} and $\langle \phi(r) \rangle$, similar to the logarithmic corrections in (3.21) and (3.26) obtained in the SCBA. We derive our results for the case of an

arbitrary spin S of the impurity in Sections 3.4.1 and 3.4.2, and then we analyze the limit of a large spin S in Section 3.4.4.

In the RG technique we consider the evolution of the coupling constant λ, quasiparticle residue Z, spin density and staggered magnetization with the energy scale μ. In the momentum-shell approach (Wilsonian RG) the RG provides an evolution of the renormalized parameters by integrating out high-energy degrees of freedom; the evolution starts at the ultraviolet scale Λ and continues all the way up to the infra-red scale Δ. The scale μ here has the meaning of the characteristic energy transfer from magnons to the impurity. At the ultraviolet scale Λ we set parameters of the theory to the bare values, in our calculations Λ plays a role of a renormalization point. Observables in the vicinity of the QCP are calculated as the result of RG evolution from the ultraviolet scale Λ to the infrared scale $\mu = \Delta$.

3.4.1 Evolution of coupling constant and quasiparticle residue

First, we calculate the evolution of the coupling constant $\lambda(\mu)$. The one-loop correction to the coupling constant is represented by the sum of diagrams, shown in Fig. 3.8.

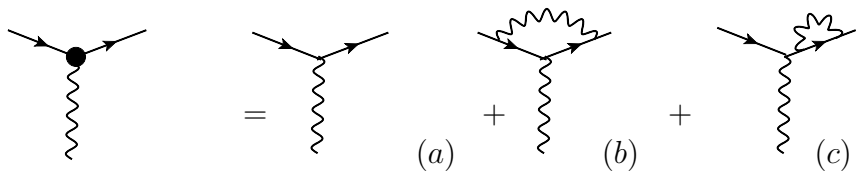

Figure 3.8: One-loop corrections to the impurity-magnon coupling constant λ.

Note, that in RG approach the correction to the coupling constant includes the vertex correction [Fig. 3.8, (b)], and also the self-energy correction [Fig. 3.8, (c)]. This is different from the SCBA, in which we disregard the diagram (b).

Contribution $\delta\lambda^{(b)}$ to the coupling constant correction is given by the diagram

(b) in Fig. 3.8 and reads

$$\boldsymbol{S}^{\mu}\delta\lambda^{(b)} = \lambda^3 \frac{\boldsymbol{S}^{\nu}\boldsymbol{S}^{\mu}\boldsymbol{S}^{\nu}}{S^2} \times \int \frac{id\omega'}{2\pi} \sum_{\boldsymbol{k}} G_0(\mu-\omega')G_0(\mu-\omega-\omega')D(\omega',\boldsymbol{k}) \approx \boldsymbol{S}^{\mu}\frac{(S(S+1)-1)}{S^2}\frac{\lambda^3}{4\pi^2}\ln\frac{\Lambda}{\mu}. \tag{3.27}$$

After cancelling out the factor $\boldsymbol{S}^{\mu}$ from the both sides of Eq. (3.27) we obtain $\delta\lambda^{(b)}$. The second contribution $\delta\lambda^{(c)}$, which comes from the diagram (c) in Fig. 3.8 reads

$$\delta\lambda^{(c)} = \lambda^3\left(1+\frac{1}{S}\right)G_0(\mu-\omega) \times \int \frac{id\omega'}{2\pi}\sum_{\boldsymbol{k}} G_0(\mu-\omega-\omega')D(\omega',\boldsymbol{k}) \tag{3.28}$$

and contains terms linear in Λ and logarithmic in Λ. The linear term corresponds to the shift of the position of quasiparticle pole ϵ_0 in the impurity's Green's function and therefore is irrelevant for our purposes. The logarithmic term in $\delta\lambda^{(2)}$ reads

$$\delta\lambda^{(c)} \to -\frac{\lambda^3}{4\pi^2}\left(1+\frac{1}{S}\right)\ln\frac{\Lambda}{\mu}. \tag{3.29}$$

The total correction to the coupling constant λ is

$$\delta\lambda = \delta\lambda^{(b)} + \delta\lambda^{(c)} = -\frac{\lambda^3}{4S^2\pi^2}\ln\frac{\Lambda}{\mu}. \tag{3.30}$$

The vertex correction (3.27) for $S = 1/2$ is suppressed by the factor $1/N = 1/3$, comparing to $\delta\lambda^{(c)}$. This suppression corresponds to the standard $1/N$ expansion of the $O(N)$ group. However, at large S the $1/N$ suppression of $\delta\lambda^{(b)}$ is compensated by S, and hence $\delta\lambda^{(b)}$ and $\delta\lambda^{(c)}$ to a large extent compensate each other, $\delta\lambda^{(b)} \approx -\delta\lambda^{(c)}$. Thus, at large S the vertex correction becomes significant and can not be disregarded. This is the reason why the SCBA fails in the case of large impurity's spin.

In the paradigm of RG, evolution of physical parameters on some energy scale μ is determined by the value of $\lambda(\mu)$ on the same scale. Hence, Eq. (3.30) results in

the following Gellman - Low equation

$$\frac{d\lambda(\mu)}{d\ln\mu} = \frac{\lambda^3(\mu)}{4S^2\pi^2}. \tag{3.31}$$

The solution to Eq. (3.31) with the initial condition $\lambda(\Lambda) = \lambda$ is

$$\lambda(\mu) = \frac{\lambda}{\sqrt{1 + \frac{\lambda^2}{2S^2\pi^2}\ln\frac{\Lambda}{\mu}}}. \tag{3.32}$$

The running coupling constant in Eq. (3.32) vanishes in the infrared limit: $\lambda(\mu) \to 0$ at $\mu \simeq \Delta \to 0$. The RG scale μ is bounded from below by the value of magnon gap $\mu \geq \Delta$.

In order to find the quasiparticle residue of the impurity's Green's function we consider the one-loop correction to the impurity's self-energy. Logarithmic part of this correction was already calculated as a part of the diagram (c) in Fig. 3.8. The corresponding equation for evolution of $Z(\mu)$ reads

$$\frac{d\ln Z(\mu)}{d\ln\mu} = \left(1 + \frac{1}{S}\right)\frac{\lambda^2(\mu)}{4\pi^2}. \tag{3.33}$$

The solution to Eq. (3.33) with the initial condition $Z(\Lambda) = 1$ is following

$$Z(\mu) = \frac{1}{\left(1 + \frac{\lambda^2}{2S^2\pi^2}\ln\frac{\Lambda}{\mu}\right)^{S(S+1)/2}} = \left(\frac{\lambda(\mu)}{\lambda}\right)^{S(S+1)}. \tag{3.34}$$

The quasiparticle residue $Z(\mu)$ vanishes, while approaching to the QCP: $\mu \simeq \Delta \to 0$.

The RG approach being used in the current Section is valid if the effective coupling constant $\tilde{\kappa} = \lambda^2/2S^2\pi^2 < 1$, since we perform perturbative expansion, such as in Eq. (3.30). However, the proper expansion parameter in the vicinity of the QCP is not $\tilde{\kappa}$, but $\tilde{\kappa}\ln\Lambda/\Delta$. The RG method (in the single-loop approximation) allows to sum up (leading) logarithmic corrections of the following kind $\tilde{\kappa}^m \sum_n \tilde{\kappa}^n \ln^n(\Lambda/\Delta)$. Therefore, the results obtained within one-loop RG in the Section 3.4 are valid when $\tilde{\kappa} < 1$, but the product $\tilde{\kappa}\ln(\Lambda/\Delta)$ can have an arbitrary value.

3.4.2 Impurity's spin and nonlocal spin density

Now we consider RG evolution of the impurity's spin S_{imp} and spin density distribution $s(r)$ with the renormalization scale μ. We compute S_{imp} and $s(r)$, considering an interaction of the system with a probe magnetic field $\boldsymbol{B}(\boldsymbol{r})$, see Section 3.3.

We start from calculation of corrections to S_{imp} due to interaction of the impurity with magnons. One-loop corrections to S_{imp} are shown in Fig. 3.9. The diagrams

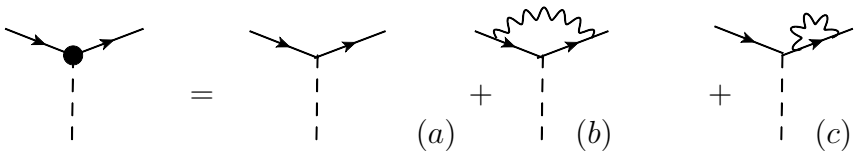

Figure 3.9: One-loop corrections to "local" spin S_{imp}.

in Fig. 3.9 are analogous to the diagrams in Fig. 3.8 for corrections to the coupling constant λ. The only difference is that the impurity-magnetic field coupling $\boldsymbol{S}_{imp} \cdot \boldsymbol{B}$ is proportional to the impurity's spin $\boldsymbol{S}_{imp}$. Hence, RG evolution of the impurity's spin is governed by the following equation

$$\frac{dS_{imp}(\mu)}{d\ln\mu} = \frac{\lambda^2(\mu)}{4S^2\pi^2} S_{imp}(\mu). \tag{3.35}$$

The solution to Eq. (3.35) with initial condition $S_{imp}(\Lambda) = S$ reads

$$S_{imp}(\mu) = \frac{S}{\sqrt{1 + \frac{\lambda^2}{2S^2\pi^2} \ln\frac{\Lambda}{\mu}}}, \tag{3.36}$$

and proportional to solution (3.32) for the running coupling $\lambda(\mu)$. The local spin at the impurity's site is equal to $S_{imp}(\mu \simeq \Delta)$ and approaches to zero at the QCP. Using the result (3.36) and relation (3.7) we obtain the distribution of staggered magnetization around impurity

$$\langle\phi(r)\rangle = -\frac{\lambda}{4\pi r} \frac{e^{-\Delta r}}{\sqrt{1 + \frac{\lambda^2}{2S^2\pi^2} \ln\frac{\Lambda}{\Delta}}}. \tag{3.37}$$

In the rest of the present Section we calculate the nonlocal spin density $s_{nl}(r)$. In the RG framework it is natural to use momentum representation for the spin density

instead of the coordinate representation, therefore we write evolution equation for the Fourier component $s_{nl}(q)$. The leading contribution to $s_{nl}(q)$ is provided by one-loop diagram, shown in Fig. 3.2, (b). Evaluation of this diagram with logarithmic precision leads to

$$s_{nl}^{(0)}(q) \approx \begin{cases} \frac{\lambda^2}{4S\pi^2} \ln \frac{\Lambda}{\mu}, & \mu \gg q, \\ \frac{\lambda^2}{4S\pi^2} \ln \frac{\Lambda}{q}, & \mu \ll q. \end{cases} \tag{3.38}$$

The Fourier transform of the second line of Eq. (3.38) gives the spin density $s_{nl}^{(0)}(r) = \lambda^2/16S\pi^3 r^3$ at the distances $1/\Lambda < r < 1/\Delta$. In analogy with the result (3.21) obtained in SCBA, in RG calculations we should expect logarithmic corrections to $\propto 1/r^3$ distribution. Note, that the logarithmic corrections are important, because they provide the proper normalization condition of the integral nonlocal spin $\int d^3 r s_{nl}(r) \to S$ at the QCP. The volume integral of the spin density $\propto 1/r^3$ is logarithmically divergent $\propto \ln \Lambda/\Delta$ if we disregard the log corrections.

In order to account for the RG evolution of the spin-density, we evaluate single-loop corrections to the leading diagram presented in Fig. 3.2, (b). Diagrams (b) and (c) in Fig. 3.10 represent these corrections, which are similar to corresponding diagrams in Figs. 3.8 and 3.9. RG evolution of nonlocal spin density distribution

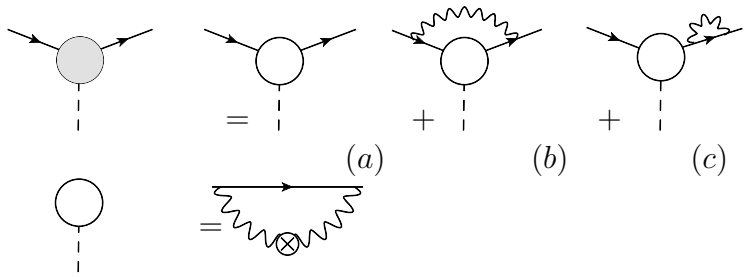

Figure 3.10: One-loop corrections to nonlocal spin density $s_{nl}(q)$.

reads

$$\frac{ds_{nl}(q,\mu)}{d\ln\mu} = \begin{cases} \frac{\lambda^2(\mu)}{4S^2\pi^2} s_{nl}(q,\mu) - \frac{\lambda^2(\mu)}{4S\pi^2}, & \mu \gg q, \\ \frac{\lambda^2(\mu)}{4S^2\pi^2} s_{nl}(q,\mu), & \mu \ll q. \end{cases} \tag{3.39}$$

The evolution equation for the spin density is different in two domains $\mu \gg q$ and $\mu \ll q$. The reason is that the one-loop expression (3.38) for spin density is different in the both domains. We solve Eq. (3.39) separately in the two domains

and match the solutions at $\mu \simeq q$. An initial condition for the evolution equation (3.39) is set to $s_{nl}(\Lambda) = 0$. We get the following result for the spin density at the infrared scale $\mu \simeq \Delta$:

$$s_{nl}(q) = \frac{S}{\sqrt{1 + \frac{\lambda^2}{2S^2\pi^2} \ln \frac{\Lambda}{\Delta}}} \left(\sqrt{1 + \frac{\lambda^2}{2S^2\pi^2} \ln \frac{\Lambda}{q}} - 1 \right). \tag{3.40}$$

In the momentum representation the net spin conservation condition has the form $s_{nl}(q)\big|_{q\to 0} + S_{imp} = S$. Using expressions (3.36) and (3.40) it is easy to check the net spin conservation, keeping in mind that the low bound for the momentum q in our formulas is $q \simeq \Delta$.

Calculating Fourier transform of Eq. (3.40) we obtain the spatial distribution of the induced spin density

$$\boxed{s_{nl}(r) = \frac{\lambda^2}{16S\pi^3 r^3 \sqrt{1 + \frac{\lambda^2}{2S^2\pi^2} \ln \frac{\Lambda}{\Delta}} \sqrt{1 + \frac{\lambda^2}{2S^2\pi^2} \ln \Lambda r}}} \tag{3.41}$$

at the distances $1/\Lambda < r < 1/\Delta$. Employing (3.41) and (3.36) one can verify conservation of the net spin in r-representation: $\int d^3r\, s_{nl}(r) + S_{imp} = S$. Integration of nonlocal spin density should be performed in the range of the distances $1/\Lambda < r < 1/\Delta$ which is defined by the infrared and the ultraviolet cutoffs of our theory.

In the vicinity of the QCP the main contribution to the nonlocal spin $\int d^3r\, s_{nl}(r)$ comes from large distances $r < 1/\Delta \to \infty$. Indeed, the integral

$$\int_{1/\Lambda \le r \le R} d^3r\, s_{nl}(r) = S \frac{\sqrt{1 + \frac{\lambda^2}{2S^2\pi^2} \ln \Lambda R} - 1}{\sqrt{1 + \frac{\lambda^2}{2S^2\pi^2} \ln \frac{\Lambda}{\Delta}}} \tag{3.42}$$

logarithmically grows as a function of the upper integration limit R, which means that the major part of spin in the nonlocal cloud is accumulated at the distances of the order of $R \simeq 1/\Delta$. At the same time, the local spin of the impurity S_{imp} vanishes at the QCP, see Eq. (3.36). Therefore, we conclude that at the QCP the impurity's spin is spatially separated from the impurity charge.

The results (3.34), (3.37) and (3.41) obtained in the RG technique are similar

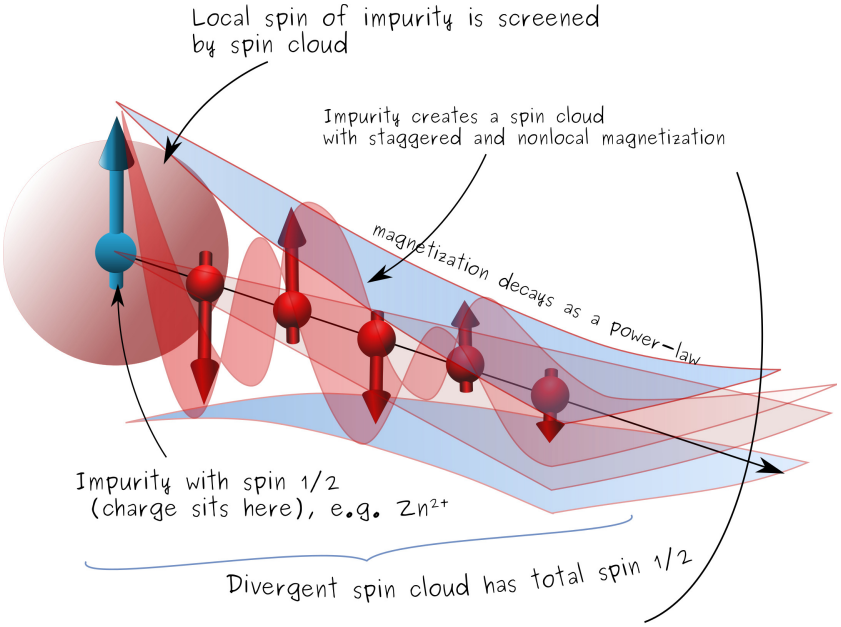

$$s_{nl}(r) \propto 1/r^3 + \mathcal{O}(\ln r), \quad \langle \phi(r) \rangle \propto 1/r$$

Figure 3.11: Bose-Kondo screening of $S = 1/2$ impurity in a 3D antiferromagnet at a QCP.

to corresponding answers (3.15), (3.26) and (3.21), obtained in the SCBA. For the spin $S = 1/2$ the difference is in the numerical factors in front of the logarithms: $3\lambda^2/2\pi^2$ in SCBA, comparing to $2\lambda^2/\pi^2$ in RG. For Z and $\langle \phi(r) \rangle$ the powers of the logarithms are also insignificantly changed: $1/2 \to 3/8$ and $2/3 \to 1/2$, respectively. The reason for these minor changes is due to the $1/N$ vertex correction, which is accounted for in the RG approach (see diagram (b) in Fig. 3.8), and is disregarded in the SCBA. The RG results are more accurate then the SCBA results. However, the expansion of the RG results and the SCBA results coincide up to the single-loop order (first order in λ^2).

3.4.3 Discussion of results

Our results show that in a three dimensional antiferromagnet impurity-induced spin density at the QCP decays as $s_{nl}(r) \propto 1/r^3$ (with the corresponding $\log(r)$ corrections) and the staggered magnetization decays as $\langle \phi(r) \rangle \propto 1/r$. RG flow in $3+1$ D leads only to $\log(r)$ corrections to $s_{nl}(r)$, leaving the power laws unchanged.

On the other hand, in $D = 2+1$ RG flow has Wilson-Fisher fixed points that

instead of log corrections provide non-trivial critical exponents for correlation functions. For instance, the impurity's quasiparticle residue $Z \propto \Delta^{\eta'/2}$ [see e.g. Ref. [64, 65]] acquires an anomalous dimension near the QCP, $\eta' = 1$ (in one-loop approximation). It results in the following scaling law [64] in the spin density distribution $s_{nl}(r) \propto 1/r^{2-\eta'/2} \approx 1/r^{3/2}$. A more accurate value of the anomalous dimension $\eta' \approx 0.4$ is known from Quantum Monte Carlo study [66] of hole-induced magnetization in Heisenberg bilayer model. Following similar arguments being used to obtain Eq. (3.7), the staggered magnetization in $D = 2+1$ reads [64] $\langle \phi(r) \rangle \propto \Delta^{\eta'/2} \ln(\Delta r)$ at $\Delta r \ll 1$. Although the scaling laws are well known, the problem of calculation of corresponding prefactors still remains unsolved.

Interestingly, the RG scaling law $s_{nl} \propto 1/r^{3/2}$ for the spin density in $D = 2+1$ can be also reproduced within our diagrammatic SCBA approach. The "dressed" impurity's Green's function at QCP in $2D$ systems has an inverse square root behaviour near the singularity point $G(\epsilon) \propto 1/\sqrt{\epsilon_0 - \epsilon}$ (see Chapter 2, Section 2.2.2 and Refs. [64, 65]). Substituting the Green's function in the Eqs. 3.18 and 3.19 and proceeding with the calculation technique described in Section 3.3.2, we recover the asymptotic behaviour $s_{nl} \propto 1/r^{3/2}$ (at $1 \ll r \ll 1/\Delta$). This result can be obtained from formula (3.19) from simple power counting. Moreover, the corresponding prefactor can be evaluated in a straightforward way using the SCBA diagrammatic technique. The SCBA diagrammatic method is more efficient computationally if compared with the standard Quantum Monte Carlo technique. This makes the SCBA very useful for calculations of impurity effects in quantum materials.

As one can see the integral spin $\int^R d^2 r s_{nl}(r)$ accumulated in the nonlocal cloud in $2+1$ D grows as a power law of upper integration limit $\propto R^{\eta'/2}$, in contrast with slow logarithmic growth in $3+1$ D [see (3.42)]. Therefore, the effect of spatial spin-charge separation at the QCP is more pronounced in two-dimensional systems, rather then in three-dimensional systems.

So far we have considered physics of spin-charge separation when approaching the QCP from the disordered phase. What happens when approaching the QCP from the AFM ordered Neel phase? In the ordered phase interaction of an impurity (hole) with a probe magnetic field cannot be written as $\psi^\dagger (\boldsymbol{S} \cdot \boldsymbol{B}) \psi$ since both the impurity and the antiferromagnetic background interact with the magnetic field.

The interaction Lagrangian, instead, has quite an unusual form [182, 183]

$$\delta\mathcal{L}_B = (\boldsymbol{B}\cdot\boldsymbol{n})\,\psi^\dagger(\boldsymbol{S}\cdot\boldsymbol{n})\psi, \tag{3.43}$$

where $\boldsymbol{n}(\boldsymbol{r})$ is Neel ordering vector, $\boldsymbol{n}^2 = 1$. The interaction energy (3.43) of the impurity with a probe magnetic field depends on the direction of the spontaneous staggered magnetization $\boldsymbol{n}$. This implies that notion of impurity's spin in the phase with broken rotational invariance is not well defined. This is why usually people use the notion of a pseudospin originating from two AFM sublattices. For example a holon carries charge and a psedospin, but it does not carry spin in the usual sense. Therefore it is possible to say that deeply in the Neel phase the impurity's spin and charge are always separated, or more precisely are partially separated, see also discussion in [34].

Even though the notion of the impurity's spin in AFM phase is poorly defined, it is not meaningless to ask a question about the distribution of induced magnetization around the impurity. We do not have complete solution to this problem, but rather propose an intuitive physical picture. Interestingly, this problem has a direct relevance to the transition to Adler's theorem regime in the ordered phase. The Adler's theorem guarantees that in the spontaneously broken phase the impurity-magnon coupling constant has additional smallness in the momentum transfer. By analogy with the case of 2D AFM [184, 61], we expect spin-density in the cloud decaying as a power law $s_{nl}(r) \propto 1/r^\nu$ in the Neel phase. The value of the exponent ν should differ in different spatial domains, provided by two characteristic scales in the problem. The first scale is determined by the impurity spin-flip energy [61], $r_A \sim 1/\lambda|\phi_0| \propto 1/\lambda|\Delta|$, here ϕ_0 is the vacuum expectation value of ϕ-field in the Neel phase. The second scale $r_H \sim 1/m_H \sim 1/|\Delta|$ is given by the energy gap of the longitudinal mode. Subscripts A and H stand for Adler and Higgs. In the region $r < r_H$ we expect the same exponent for the magnetization decay, $s_{nl}(r) \propto 1/r^3$, as on the disordered side of the QCP. To put it in another way, at small distances $r < r_H$ only magnons with large momenta are relevant, which do not "know" the difference between the spontaneously broken and the paramagnetic phases. On the other hand, at the distances $r > r_A$ Adler's theorem for the impurity-magnon ver-

tex is valid and hence the magnetization cloud decays faster than $1/r^3$; we expect that it decay as $1/r^5$. A crossover between the two decays laws is within the range $r_H < r < r_A$. At the QCP the both scales diverge, which means the region with $s_{nl}(r) \propto 1/r^3$ is unlimitedly extending at $|\Delta| \to 0$. This is the same behaviour as in the disordered phase.

3.4.4 Semiclassical limit: impurity with a large spin S

From a theoretical point of view it is interesting to consider the semiclassical case of a large spin of the impurity. Taking a formal limit $S \to \infty$ in Eqs. (3.36), (3.37) and (3.41) we obtain

$$S_{imp} = S, \quad s_{nl}(r) = 0, \quad \langle \phi(r) \rangle = -\lambda \frac{e^{-\Delta r}}{4\pi r}. \tag{3.44}$$

We see from Eq. (3.44), that in the semiclassical limit there is no nonlocal spin density around the impurity and a local spin S is unscreened in this case. Therefore, there is no spin-charge separation in the semiclassical limit.

A local impurity's spin, nonlocal spin density and staggered magnetization in the semiclassical limit are provided just by tree-level Feynman diagrams. The reason is that quantum fluctuations of the impurity's spin are suppressed at large S. Let us consider the case of the impurity in the state with the maximal projection of spin on the quantization axis z: $|S, S_z = S\rangle$. The interaction of the impurity with magnon either leaves the projection S_z to be unchanged or changes it by unity, $\Delta S_z = -1$. The action of an operator $\hat{S}_z$ on the state $|S, S\rangle$ provides an eigenvalue S. On the other hand, the matrix element of the lowering operator $\hat{S}_-$ between the states $|S, S-1\rangle$ and $|S, S\rangle$ is equal to $\sqrt{2S}$. Therefore, the processes with a change of the projection of the impurity's spin are suppressed in the limit of a large S.

In the semiclassical limit only the z-component of the operator of impurity's spin is relevant, therefore the Lagrangian in Eq. (3.4) corresponding to the interaction of the impurity with magnons takes the form

$$\mathcal{L}_{int} = -\lambda \psi^\dagger \psi \phi_z. \tag{3.45}$$

Thus, the problem of a classical impurity "dressed" by z-polarized magnons is equivalent to the problem of impurity interacting with a scalar bosonic field ϕ_z. The problem of an impurity immersed in a scalar boson bath is known as the independent boson model, this model is exactly solvable. [185] The exact solution agrees with Eq. (3.44).

A retarded Green's function of the impurity in time representation at $t > 0$ reads [185]

$$G(t) = -i \exp\left[it\epsilon_0 - \lambda^2 \sum_{\boldsymbol{q}} \frac{(1 - e^{-i\omega_q t})}{2\omega_q^3} \right], \tag{3.46}$$

where $\epsilon_0 = -\lambda^2 \sum_q 1/2\omega_q^2$. Performing Fourier transformation of the impurity Green's function (3.46), and calculating a quasiparticle residue at the Green's function pole $\epsilon = \epsilon_0$, we obtain

$$Z = \exp\left(-\lambda^2 \sum_q \frac{1}{2\omega_q^3} \right) = \left(\frac{\Delta}{\Lambda} \right)^{\lambda^2/4\pi^2}. \tag{3.47}$$

In the limit $S \to \infty$ the RG result (3.34) is consistent with Eq. (3.47).

3.5 Conclusion

The present Chapter has considered a single impurity with a spin S embedded into a 3D AFM system, which is close to the $O(3)$ QCP separating paramagnetic and the Neel phase. The impurity's spin induces the usual magnetization and the staggered magnetization clouds around the site of the impurity. Approaching the QCP from the disordered phase, we have calculated spatial distributions of the spin density $s(r)$ (magnetization) and the staggered magnetization $\langle \phi(r) \rangle$ in the cloud. For calculations we use two different methods, Self Consistent Born Approximation (SCBA) and Renormalization Group (RG). The SCBA is justified by the small parameter $1/N$ where $N = 3$ for the $O(3)$ group, while RG is justified by the small coupling constant. We show that for $S = 1/2$, the results of the both methods are consistent within the expected accuracy $1/N$. However, at larger values of the impurity's spin SCBA method is not valid because the small parameter $1/N$ is compensated by the large spin. Therefore, for $S \geq 1$ only the RG results are valid.

The impurity's quasiparticle residue vanishes at the QCP, see Eq. (3.34). This is the first indication that the impurity's spin is fully transferred to the magnon cloud. The effect of screening of the impurity's spin by spin-one magnetic fluctuations is a Kondo-like effect in a bosonic sector. [169] The spin density has a local component $S_{imp}\delta(\boldsymbol{r})$, which is localized at the site of the impurity, as well as a spatially distributed nonlocal part $s_{nl}(r)$. As a result of the vanishing residue the impurity's average spin S_{imp} logarithmically vanishes at the QCP, see Eq. (3.34). The total spin S is conserved and it is transferred into the nonlocal spin cloud. The nonlocal spin density at $r < 1/\Delta$, where Δ is the magnon gap, decays as $s_{nl}(r) \propto 1/r^3$ with proper logarithmic corrections, see Eq. (3.41). At $r > 1/\Delta$ the spin density decays exponentially.

Spin in the nonlocal cloud is mainly accumulated at large distances $r \simeq 1/\Delta$, see Eq. (3.42). Therefore the spin is spatially separated from the impurity and at $\Delta \to 0$ the separation scale becomes infinite. In this sense our results demonstrate the spin-charge separation in 3D magnetic systems at the QCP.

Interestingly, the cloud of the staggered magnetization at $r < 1/\Delta$ decays only as the first power of distance, see Eq. (3.37). This is why a tiny concentration of impurities can significantly influence the critical behaviour of the system.

Finally, we have analyzed the semiclassical limit of a very large impurity spin, $S \gg 1$. In this limit the quantum spin-flip transitions become negligible and the spin impurity problem is reduced to an exactly solvable textbook example. [185]

Chapter 4

The amplitudes and the structure of charge density wave in YBCO

In this chapter we perform phenomenological analysis of experimental data on the recently discovered charge density wave (CDW) in underdoped cuprates and report unknown s- and d-wave amplitudes of the CDW. The analysis includes data on nuclear magnetic resonance, resonant inelastic X-ray scattering, and hard X-ray diffraction for ortho-II $YBa_2Cu_3O_y$ (YBCO). The amplitude of doping modulation found in my analysis is of the order of $\delta p \sim 5 \cdot 10^{-3}$ of elementary charge per unit cell of a CuO_2 plane. We show that the data rule out a checkerboard pattern, and we also show that the data potentially exclude mechanisms of the CDW which do not include phonons.

4.1 Introduction

The recent discovery of the charge density wave (CDW) in YBCO and other cuprates gave a new twist to physics of high-T_c superconductivity. Existence of a new charge ordered phase has been reported in bulk sensitive nuclear magnetic resonance (NMR) measurements [41, 42, 43], resonant inelastic X-ray scattering (RIXS) [35, 36, 37], resonant X-ray scattering [38] and hard X-ray diffraction (XRD) [39]. Additional non-direct evidence comes from measurements of ultrasound speed [186] and Kerr rotation angle [187].

While the microscopic mechanism of the CDW and its relation to superconductivity remains an enigma, there are several firmly established facts listed below, here we specifically refer to YBCO. (i) The CDW state arises in the underdoped regime within the doping range $0.08 \leq p \leq 0.13$. (ii) The onset temperature of CDW at doping $p \sim 0.1$ is $T_{CDW} \approx 150$ K, which is between the pseudogap temperature T^* and the superconducting temperature T_c, $T_c < T_{CDW} < T^*$. (iii) The CDW "competes" with superconductivity, the CDW amplitude is suppressed at $T < T_c$. Probably due to this reason the CDW amplitude at $T < T_c$ is enhanced by a magnetic field that suppresses superconductivity. (iv) The CDW wave-vector is directed along the CuO link in the CuO_2 plane. (v) The wave-vector $Q \approx 0.31$ r.l.u. only very weakly depends on doping. (vi) The CDW is essentially two-dimensional in low magnetic fields, the correlation length in the c-direction is about one lattice spacing, while the in-plane correlation length is $\xi_{a,b} \sim 20$ lattice spacings. (vii) In high magnetic fields ($B > 15$ T) and low temperatures ($T < 50$ K) the CDW exhibits three-dimensional correlations with the correlation length in the c-direction $\xi_c \sim 5$ lattice spacings [188, 40]. (viii) Ionic displacements in the CDW are about $10^{-3}\mathring{A}$ [189].

In spite of numerous experimental and theoretical works, there are two major unsolved problems in the phenomenology of the CDW. (i) The amplitude of the electron density modulation remains undetermined. (ii) The intracell spatial charge pattern is unclear, while there are indications from RIXS [190] and from scanning tunneling microscopy [191] that the pattern is a combination of s- and d-waves. The major goal of the present work is to resolve the open problems. We stress that in the present Chapter we perform combined analysis of experimental data to resolve the problems of the phenomenology, but we do not build a microscopic model of the CDW. While we rely on various data, the most important information in this respect comes from NMR. In particular we use the ortho-II YBCO data. Ortho-II YBCO (doping $p \approx 0.11$) is the least disordered underdoped cuprate and hence it has the narrowest NMR lines. Development of the CDW with decreasing of temperature leads to the broadening of the quadrupole satellites in the NMR spectrum [41, 42, 43]. Below we refer the quadrupole satellites as NQR lines. Quite often the term "NQR" implies zero magnetic field measurements. We stress that

it is not true in our case, NQR here means quadrupole satellites of NMR lines. The broadening is directly proportional to the CDW amplitude with the coefficients determined in Ref. [192]. So, one can find the CDW amplitude and this is the idea of the present analysis. Moreover, combining the data on copper and oxygen NMR we deduce the CDW intracell pattern within the CuO_2 plane.

The second goal of the present work is "partially theoretical". Based on the phonon softening data [193] we are able to separate between two broad classes of possible mechanisms responsible for the formation of the CDW. (i) In the first class the CDW is driven purely by strongly correlated electrons which generate the charge wave. In this case phonons and the lattice are only spectators which follow electrons. (ii) In the second class, which we call "the Peierls/Kohn" scenario, both electrons and phonons are involved in the CDW development on equal footing. We argue that the phonon softening data [193] potentially supports the second scenario.

4.2 The amplitudes of the CDW: analysis of NMR data

The CDW implies modulation of electron charge density on copper and oxygen sites in the CuO_2-planes. Our notations correspond to the orthorhombic YBCO, the axis c is orthogonal to the CuO_2-plane, the in-plane axes a and b are directed perpendicular and parallel to the oxygen chains, respectively. Usually the CDW is described in terms of s-, s'-, and d-wave components with amplitudes A_s, $A_{s'}$, and A_d, see e.g. Refs. [190, 44, 191]. The s-wave component corresponds to the modulation of the population of Cu $3d_{x^2-y^2}$ orbitals, and s'- and d-wave components correspond to the modulation of the populations of oxygen $2p_\sigma$ orbitals:

$$\begin{aligned}
\delta n_d &= A_s \cos[\boldsymbol{Q}\cdot\boldsymbol{r} + \phi_s], \\
\delta n_{px} &= A_{s'} \cos[\boldsymbol{Q}\cdot\boldsymbol{r} + \phi_{s'}] + A_d \cos[\boldsymbol{Q}\cdot\boldsymbol{r} + \phi_d], \\
\delta n_{py} &= A_{s'} \cos[\boldsymbol{Q}\cdot\boldsymbol{r} + \phi_{s'}] - A_d \cos[\boldsymbol{Q}\cdot\boldsymbol{r} + \phi_d].
\end{aligned} \tag{4.1}$$

Here $\boldsymbol{Q}$ is the wave vector of the CDW, directed along a or b crystal axis [$\boldsymbol{Q} = (Q, 0)$ or $\boldsymbol{Q} = (0, Q)$] and ϕ_s, $\phi_{s'}$, ϕ_d are the phases of s-, s'- and d-waves. The subscripts "x" and "y" in Eq. (4.1) indicate different oxygen sites within the CuO_2-plane unit cell. The standard nomenclature of the oxygen sites in YBCO is O(2) and O(3). The O(2) $2p_\sigma$-orbital is parallel to the axis "a", and the O(3) $2p_\sigma$-orbital is parallel to the axis "b", see Fig. 4.1. For the CDW wave-vector $\boldsymbol{Q}$ directed along the a-axis, the "x"-site is O(2) and the "y"-site is O(3) as shown in Fig. 4.1. In the same figure we indicate excess charge corresponding to s, s'-, and d-waves. For $\boldsymbol{Q}$ orientated along the axis "b" the "x"-site is O(3), and the "y"-site is O(2).

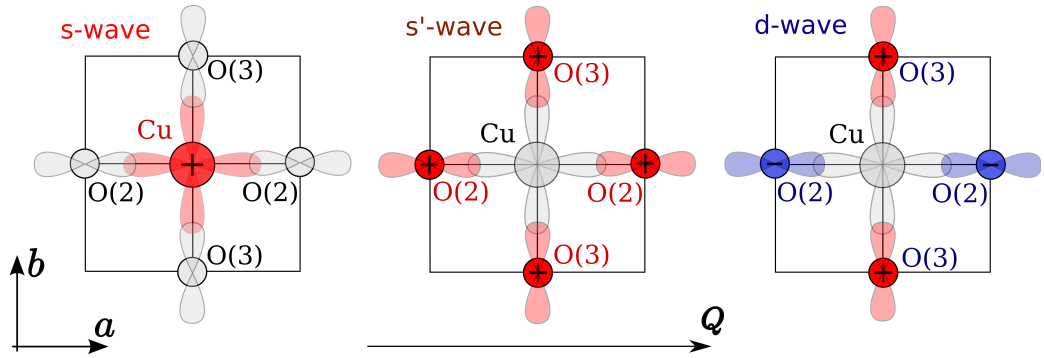

Figure 4.1: Intra-unit cell patterns of the CDW directed along the a-axis, $\boldsymbol{Q} = (Q, 0)$: s-wave, s'-wave, and d-wave. Positive and negative excess charge variations are shown in red and blue respectively.

According to the analysis [192] the NQR frequency of a particular ^{17}O nucleus is proportional to the local hole density n_p at this site, and of course it depends on the orientation of the magnetic field with respect to the oxygen p-orbital,

$$\begin{aligned} B \perp 2p_\sigma: \quad & f_{O\perp} \approx 1.23 MHz \times n_p + C_1, \\ B \parallel 2p_\sigma: \quad & f_{O\parallel} \approx 2.45 MHz \times n_p + C_2, \end{aligned} \tag{4.2}$$

where B is the external magnetic field of NMR. Constants C_1 and C_2 are due to other ions in the lattice; generally they depend on the position of the oxygen ion in the lattice. Typical values of these constants are: $C_1 \sim 0.2$ MHz, $C_2 \sim 0.5$ MHz. According to the same analysis [192] the ^{63}Cu NQR frequency is proportional to

the local hole density n_d at the Cu site and also n_p at the adjacent oxygen sites,

$$\begin{aligned} \mathrm{Cu}^{63}(B\,||\,c):\ f &\approx 94.3MHz\times n_d \\ &- 11MHz\times[4-(n_{pa}+n_{pb})]+C_3. \end{aligned} \tag{4.3}$$

Here the "ion-related" constant $C_3 \sim -6$ MHz.

There are two mechanisms for the position dependent variation of the NQR frequency which are related to the CDW, (i) a variation of the local densities n_d, n_p, (ii) a variation of the ions' positions. The position dependent frequency variation leads to the observed inhomogeneous broadening of the NQR line. Let us show that the mechanism (ii) is negligible. Only in-plane displacements of ions contribute to (ii) in the first order in the ion displacement. The magnitudes of the relative in-plane displacements of Cu and O ions are $\delta r/r \lesssim 10^{-3}$ [189], where $r \approx 2\mathring{A}$ is the Cu-O distance. Hence we can expect a lattice-related variation of e.g. oxygen $f_\perp$ at the level $\delta f_\perp \sim C_1\delta r/r \sim 0.2$ kHz. This is two orders of magnitude smaller than the CDW related broadening ~ 10 kHz observed experimentally. For copper nuclei the expected ion-related broadening comes mainly from the 11×4MHz term in (4.3), $\delta f \sim \delta r/r \times 44$ MHz ~ 0.04 MHz. Again, this is much smaller than the observed broadening ~ 1 MHz. These estimates demonstrate that one can neglect the contribution of the lattice distortion in the NQR broadening. Therefore, below we consider only the broadening mechanism (i) related to variation of hole densities.

Any compound has an intrinsic quenched disorder. The disorder is responsible for the NQR line widths at $T > T_{CDW}$. The experimental NQR lines in a "weak magnetic field", $B = 12-15$T, are practically symmetric, the analysis of the NQR lines and the corresponding values of full widths at half maximum (FWHM) are presented in Refs. [42, 43]. However, the experimental NQR lines in a "strong magnetic field" [41], $B \approx 30$T, are somewhat asymmetric due to various reasons. The asymmetry brings a small additional uncertainty in the analysis. The "strong field" data is less detailed than the "weak field" data and therefore the additional uncertainty is completely negligible, the "strong field" NQR widths are given in Ref. [41].

Hereafter we assume simple Gaussian lines, $I(f) \propto \exp[-(f-f_0)^2/2\sigma_0^2]$, where

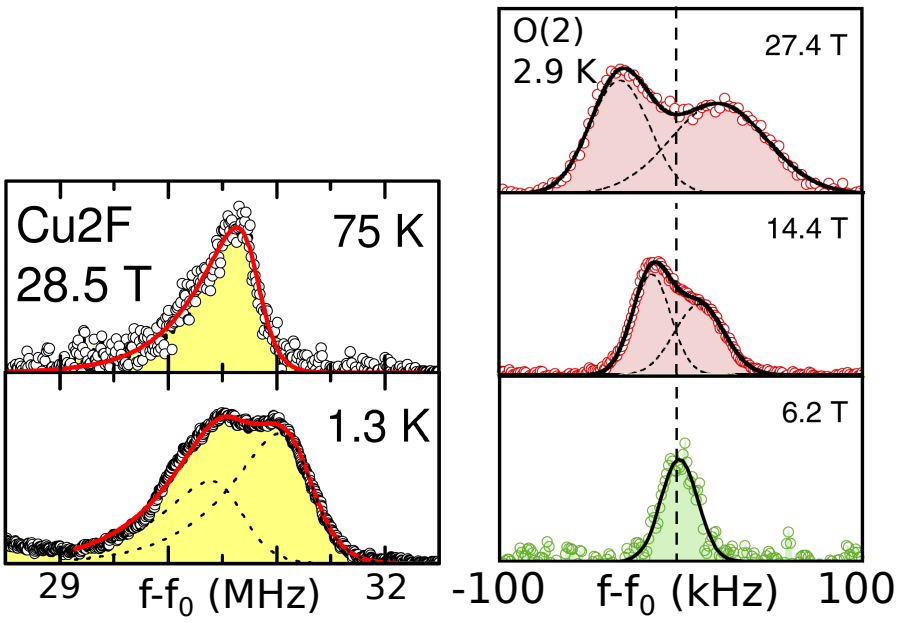

Figure 4.2: Experimental NQR lines in ortho-II YBCO. Left panel: ^{63}Cu in magnetic field $B = 28.5$T at two different temperatures, 75K and 1.3K [41]. Right panel: ^{17}O at $T = 2.9$K at different values of magnetic field [42].

f_0 is the center of the NQR line, σ_0 corresponds to the intrinsic disorder-related width. At $T < T_{CDW}$ the line shape is changed to

$$I(f) \propto \left\langle \exp\left\{ -\frac{[f - f_0 - \delta f(\mathbf{r})]^2}{2\sigma_0^2} \right\} \right\rangle , \tag{4.4}$$

where $\delta f(\boldsymbol{r})$,

$$\delta f(\boldsymbol{r}) = A\cos[(\boldsymbol{Q}\cdot\boldsymbol{r}) + \phi] \tag{4.5}$$

follows from Eqs. (4.2), (4.3), (4.1). In particular, in MHz

$$\begin{aligned}
\delta f_{O\perp} &= 1.23\left\{A_{s'}\cos[\boldsymbol{Q}\cdot\boldsymbol{r} + \phi_{s'}] \pm A_d\cos[\boldsymbol{Q}\cdot\boldsymbol{r} + \phi_d]\right\}, \\
\delta f_{O||} &= 2.45\left\{A_{s'}\cos[\boldsymbol{Q}\cdot\boldsymbol{r} + \phi_{s'}] \pm A_d\cos[\boldsymbol{Q}\cdot\boldsymbol{r} + \phi_d]\right\}, \\
\delta f_{Cu} &= 94.3A_s\cos[\boldsymbol{Q}\cdot\boldsymbol{r} + \phi_s] + 22A_{s'}\cos[\boldsymbol{Q}\cdot\boldsymbol{r} + \phi_{s'}].
\end{aligned} \tag{4.6}$$

The averaging in Eq. (4.4), $\langle ....\rangle$, is performed over the position $\mathbf{r}$ of a given ion (Cu or O) in the CuO plane. A simulation of $I(f)$ in Eq. (4.4) with δf from (4.5) is straightforward, the results for several values of the ratio A/σ_0 are presented in

Fig. 4.3a. The CDW leads to the NQR line broadening and at larger amplitudes

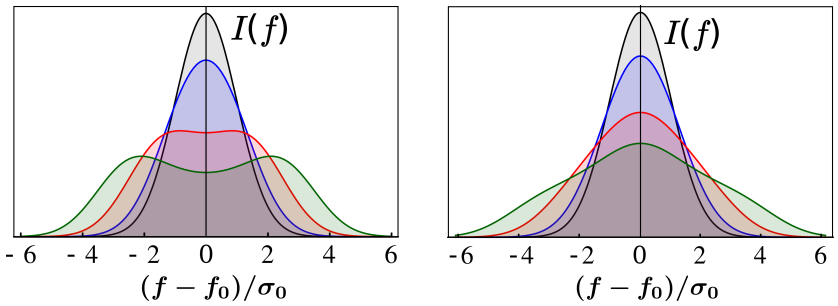

Figure 4.3: **(a)** The NQR lineshapes for the stripe-like CDW (4.5). **(b)** The NQR lineshapes for the checkerboard CDW (4.7). Both **(a)** and **(b)** show the lines for four different values of the CDW amplitude A with respect to the intrinsic broadening, $A/\sigma_0 = 0, 1, 2, 3$.

results in a distinctive double peak structure. For a comparison in the Panel b of Fig. 4.3 we present the lineshapes obtained with Eq. (4.4) for the checkerboard density modulation,

$$\delta f(\boldsymbol{r}) = \frac{A}{\sqrt{2}}[\cos(Qr_a) + \cos(Qr_b)] \ . \tag{4.7}$$

Obviously, the lineshapes in panels a and b of Fig. 4.3 are very different. The checkerboard pattern does not result in the double peak structure even at very large amplitudes. NQR data [41, 42] clearly indicate the double peak structure. This is a fingerprint of the stripe-like CDW. Comparison of the experimental NQR lineshapes with Panels b of Fig. 4.3 rules out the checkerboard scenario at large magnetic field, see also [195, 196, 197].

The qualitative difference between the lineshapes corresponding to the stripe and the checkerboard patterns is a "density of states" effect. Indeed, the NQR intensity (4.4) can be written in terms of the "density of states"

$$I(f) \propto \langle \ldots \rangle = \int dS \, (\ldots) = \int df \, \nu(f)(\ldots), \tag{4.8}$$

where $(\ldots)$ denotes the Gaussian exponent in (4.4), dS is the element of area in the CuO_2 plane. The "density of states" $\nu(f) = \int dS \, \delta(f - f_0 - \delta f(\boldsymbol{r}))$ in the case of the stripe-like CDW (4.5) has two singularities, see Fig. 4.4, at points $f - f_0 = \pm A$.

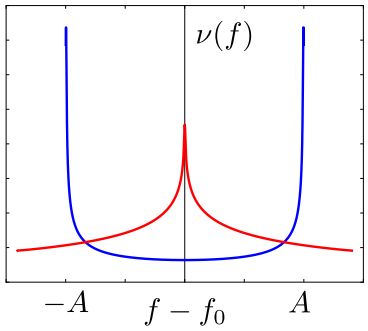

Figure 4.4: "Density of states" $\nu(f)$ for the stripe CDW (blue line) and for the checkerboard CDW (red line). The two singularities at $f - f_0 = \pm A$ in the case of the stripe-like CDW result in the double peak structure of the NQR lines.

The singularities result in two peaks in the NQR spectrum. On the other hand, in the case of the checkerboard CDW (4.7) the "density of states" $\nu(f)$ has a single maximum at $f = f_0$, see Fig. 4.4, leading to a single-peak NQR lineshape. After averaging over the $(Q, 0)$ and $(0, Q)$ stripe domains the double-peak NQR lineshape is intact. Of course this is true only because the size of the domains ($\xi_{a,b} \sim 20 - 60$ lattice spacings) is much larger then the period of the CDW ($2\pi/Q \approx 3.2$ lattice spacings).

Numerical integration (averaging) in (4.4) shows that the full NQR line width at half maximum can be approximated as

$$\begin{aligned} &\Gamma_0 = \sqrt{8 \ln 2}\sigma_0, \\ &\Gamma \approx \sqrt{\Gamma_0^2 + 4 \ln 2 A^2}\ , \qquad \text{if} \ \ \Gamma < \Gamma_0, \\ &\Gamma \approx 1.2\sqrt{\Gamma_0^2 + 4 \ln 2 A^2}\ , \quad \text{if} \ \ \Gamma > 2\Gamma_0. \end{aligned} \tag{4.9}$$

Note that this is the FWHM even for the non-Gaussian line shape like that in Fig. 4.3a. All the data we use below are in the regime $\Gamma \geq 2\Gamma_0$.

The typical dependence of the experimental NQR line width [43] on temperature is sketched in Fig. 4.5.

Hereafter we denote by Γ_0 the value of the width at the temperature, where the width starts to increase with lowering of temperature, and by Γ_1 the value of the width at the lowest available temperature, as indicated in Fig. 4.5. The increase of the width at low temperatures is due to the CDW development. Comparing

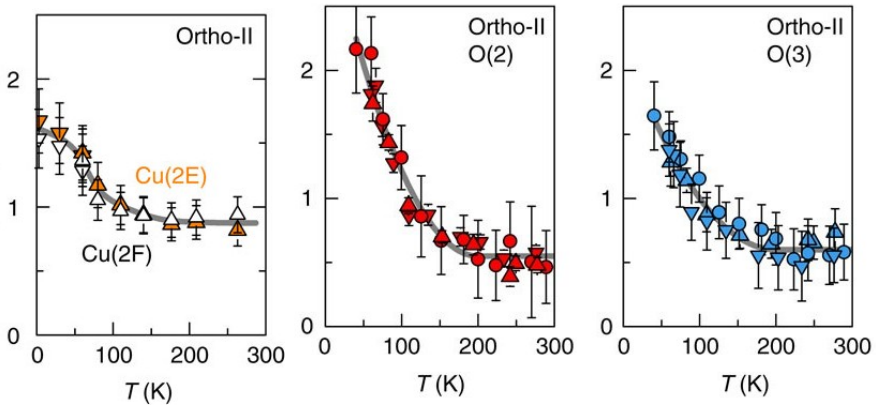

Figure 4.5: Ortho-II YBCO NQR line broadening versus temperature [43]. ^{63}Cu data (panel a) are taken in magnetic field 11T and 15T, and ^{17}O data (panels b,c) are taken in magnetic field 12T. The width is presented in units of the corresponding central line frequency f_0 [43]. The panel a shows Cu(2) data for $B||c$. The panels b and c present O(2) and O(3) data respectively for three field orientations, $B||a$, $B||b$, and $B||c + 20^o$.

the data with Eqs. (4.9) we can find the CDW amplitudes. There are two distinct Cu positions in ortho-II YBCO, Cu(2E) and Cu(2F), that reside under the empty (E) and full(F) oxygen chains, respectively. There are also three distinct in-plane oxygen positions, O(2), O(3F), and O(3E). The O(2) $2p_\sigma$ orbital is oriented along the a-axis, and the O(3F), O(3E) $2p_\sigma$ orbitals are oriented along the b-axis (see Fig. 4.1). O(3F) resides under the full chain and O(3E) resides under the empty chain. The NQR broadening data for Cu(2E) and Cu(2F) are almost identical, the same is true for O(3F) and O(3E). Therefore, in our analysis we do not distinguish "E" and "F" and refer to them as Cu(2) and O(3) respectively.

It is worth noting that the NQR lines have been measured in NMR experiments. Therefore, the actual line broadening is a combined effect of the NQR broadening and the NMR broadening. The NMR broadening comes from the magnetic Knight shift which is proportional to the charge density modulation. The Knight shift broadening is itself an interesting effect which can bring additional information about CDW. However, our present analysis is aimed at NQR. The structure of NMR satellites enables the subtraction of the Knight shift effect from the data. The subtraction results in the "rectified" NQR line widths, which we use in our analysis.

The rectified NQR line widths obtained in Refs. [43, 194] for different ions and for different orientations of magnetic field are listed in the second and third columns of Table 4.1. In this case the magnetic field is $B = 12 - 15$T, Γ_0 corresponds to 150K and Γ_1 corresponds to 60K. Figures in brackets represent crude estimates of error

	$\Gamma_0(kHz)$	$\Gamma_1(kHz)$	$\lvert A_s + 0.23A_{s'}\rvert$
Cu(2), B||c	230(30)	460(80)	2.0(0.5)
			$\sqrt{A_{s'}^2 + A_d^2}$
O(2), $2p_\sigma \| \| a$, B||a	6.0(0.5)	16.0(1.3)	2.9(0.3)
O(2), $2p_\sigma \| \| a$, B||b	6.0(0.6)	15.0(0.8)	5.4(0.4)
O(2), $2p_\sigma \| \| a$, B||c $+20^o$	5.0(2.0)	16.0(2.5)	6.0(1.1)
O(3), $2p_\sigma \| \| b$, B||a	6.0(1.0)	11.0(1.8)	3.6(0.9)
O(3), $2p_\sigma \| \| b$, B||b	5.0(2.0)	12.0(2.0)	2.1(0.5)
O(3), $2p_\sigma \| \| b$, B||c $+20^o$	9.0(2.3)	18.0(2.3)	6.1(1.4)

Table 4.1: NQR data for ortho-II YBCO in magnetic field $B = 12 - 15$T. The line widths, $\Gamma_0 = \Gamma_{T=150K}$ and $\Gamma_1 = \Gamma_{T=60K}$, are measured for different ions and for different orientations of the magnetic field [43, 194]. The last column displays the CDW amplitudes deduced from the particular line. Figures in brackets represent crude estimates of error bars.

The CDW-induced broadening at oxygen sites comes from contributions of the s'- and d-waves, see Eq. (4.6). RIXS and XRD data [35, 36, 39, 37] suggest that the CDW state consists of equally probable domains with the one-dimensional CDW along $(Q, 0)$ and $(0, Q)$ directions. This means, that even if the phases of s' and d-wave are locked in a domain, say $\phi_{s'} = \phi_d$, the s'-d interference disappears from the oxygen broadening after averaging over orientations of the domains. Hence, comparing Eqs. (4.5) and (4.6) we conclude that for the oxygen sites $A = K\sqrt{A_{s'}^2 + A_d^2}$ with the coefficient $K = 1.23$MHz or $K = 2.45$MHz dependent on the orientation of the magnetic field. Using the experimental widths presented in Table 4.1 together with Eq. (4.9) one finds values of $\sqrt{A_{s'}^2 + A_d^2}$ for each particular oxygen ion and orientation of the magnetic field. The values with indicative error bars are listed in the last column of Table 4.1. The average over the six different cases presented in the Table is

$$\sqrt{A_{s'}^2 + A_d^2} = 3.8 \cdot 10^{-3} \ . \tag{4.10}$$

Note, that the indicative error bars in Table 4.1 are not statistical, therefore in Eq. (4.10) we present the simple average value.

The CDW-induced broadening at Cu sites comes from contributions of s- and s'-waves, see Eq. (4.6). Below we assume that the phases are locked, $\phi_s = \phi_{s'}$. Hence comparing Eqs. (4.5) and (4.6) we conclude that for Cu sites $A = 94.3|A_s + 0.23A_{s'}|$MHz.

Using the experimental widths presented in the top line of Table 4.1 together with Eq. (4.9) we find

$$|A_s + 0.23A_{s'}| = 2.0 \cdot 10^{-3} \ . \tag{4.11}$$

It is very natural to assume that the amplitudes A_s and $A_{s'}$ are related as components of Zhang-Rice singlet, $A_s \approx 2A_{s'}$, see Ref. [192]. Hence, using (4.10), (4.11) we come to the following CDW amplitudes at $T = 60$K and $B \approx 12 - 15$T,

$$\begin{aligned} &A_s = 1.8 \cdot 10^{-3}, \quad A_{s'} = 0.87 \cdot 10^{-3}, \\ &A_d = 3.8 \cdot 10^{-3}, \quad \delta p = A_s + 2A_{s'} = 3.5 \cdot 10^{-3} \ . \end{aligned} \tag{4.12}$$

The values of $A_{s,s',d}$ are in units of the number of holes per atomic site, and δp is the doping modulation amplitude in units of the number of holes per unit cell of a CuO_2 plane. Values of the amplitudes have not been reported previously, but the ratios have been deduced from the polarization-resolved resonant X-ray scattering [190]. Our ratio $A_{s'}/A_d \approx 0.23$ is reasonably close to the value $A_{s'}/A_d \approx 0.27$ obtained in Ref. [190], however the ratio $A_s/A_d \approx 0.47$ is significantly larger than the value reported in Ref. [190]. Superficially our ratio $A_{s'}/A_d \approx 0.23$ is reasonably close to the value $A_{s'}/A_d \approx 0.27$ obtained in Ref. [190], on the other hand the ratio $A_s/A_d \approx 0.47$ is significantly larger than the value reported in Ref. [190]. However, one has to be careful making a direct comparison of our results with Ref. [190]. The analysis [190] assumes either $s + d$ or $s' + d$ models, while we keep the three components ($s + s' + d$ model). For example, it is easy to check that the $s' + d$ model ($s = 0$) is inconsistent with the NQR data, so the agreement in the value $A_{s'}/A_d \approx 0.27$ is purely accidental. On the other hand, in principle we can fit the NQR data by the $s + d$ model ($s' = 0$), this results in $A_s/A_d \approx 0.53$ that is

inconsistent with [190].

The ratios of the CDW amplitudes $A_s/A_d \sim 0.2$, $A_{s'}/A_d \sim 0.1$ have been reported in STM measurements with BSCCO and NaCCOC [44]. Comparing these ratios (although measured in different cuprates) with our results we see that [44] indicates dominance of the d-wave component, whereas in our analysis the s-wave amplitude is about a half of the d-wave amplitude. We do not have an explanation for the discrepancy between our results and REXS/STM measurements [190, 44], moreover REXS and STM are inconsistent with each other. The advantage of our analysis is that it is very simple and straightforward and, of course, NQR is a bulk probe.

Unfortunately, NQR data for magnetic field $B \approx 30$T are not that detailed as that for $B \approx 12 - 15$T. Nevertheless, based on the Cu NQR/NMR line broadening measured in Ref. [41] and rectifying the Cu NQR line width (subtracting the Knight shift), we conclude that $\Gamma_0 = \Gamma_{T=75K} = 0.6$MHz and $\Gamma_1 = \Gamma_{T=1.3K} = 1.0$MHz. Hence, using the same procedure as that for the low magnetic field, we find $|A_s + 0.23A_{s'}| = 3.7 \cdot 10^{-3}$. Again, assuming the Zhang-Rice singlet ratio, $A_s \approx 2A_{s'}$, we find the s-wave CDW amplitudes for $B \approx 30$T and $T = 1.3$K:

$$\begin{aligned} &A_s = 3.3 \cdot 10^{-3}, \quad A_{s'} = 1.6 \cdot 10^{-3}, \\ &\delta p = A_s + 2A_{s'} = 6.5 \cdot 10^{-3} \ . \end{aligned} \tag{4.13}$$

The doping modulation amplitude δp is about two times smaller than the estimate presented in Ref. [41]. Unfortunately, data [42] are not sufficient for unambiguous subtraction of the Knight shift broadening from oxygen lines, so the determination of A_d is less accurate. However, roughly at $B \approx 30$T and $T = 1.3$K the value is $A_d \sim 6 \cdot 10^{-3}$.

4.3 Discussion on microscopic mechanism of the CDW

To complete our phenomenological analysis we comment on two broad classes of possible mechanisms of the CDW instability. (i) In the first class the CDW instability is driven purely by strongly correlated electrons which generate the charge wave. It can be due to electron-electron interaction mediated by spin fluctuations and/or due to the Coulomb interaction, see e.g. Refs [199, 198]. We call this class of CDW formation mechanisms the "electronic scenario". In this scenario phonons/lattice are not crucial for the CDW instability, they are only spectators that follow electrons. (ii) In the second class which we call the "Peierls/Kohn scenario" and which is known in some other compounds [200, 201, 202], both electrons and phonons are involved in the CDW development on equal footing. We argue that the phonon softening data might support the second class.

A very significant softening of transverse acoustic and transverse optical modes in YBCO has been observed in Ref. [193]. The softening data are reproduced in Fig. 4.6a. The anomaly is very narrow in momentum space, $\delta q \approx 0.04$ r.l.u., and it is only two times broader than the width of the elastic CDW peak, $\delta q = 1/\xi_{a,b} \approx 0.02$ r.l.u. measured in RIXS and XRD [35, 39, 37]. Our observation is very simple, in the case of the "electronic" scenario, the electronic CDW creates a weak periodic potential $V = V_0 \cos(\mathbf{Q} \cdot \mathbf{r} + \phi)$ for phonons. Diffraction of phonons from the potential must lead to the usual band-structure discontinuity of the phonon dispersion ω_q at $q = Q$ as it is shown by blue lines in Panel b of Fig. 4.6. In the presence of the finite correlation length of the CDW the discontinuity is healed as it is shown by the red solid line at the same panel, and combined blue-red solid line shows the expected phonon dispersion. In Section 4.3.1 we present a calculation which supports this picture, but generally the picture is very intuitive. Obviously, this physical picture for the phonon dispersion is qualitatively different from the experimental data in Panel a of Fig. 4.6. On the other hand the "Peierls/Kohn scenario", where both electrons and phonons are equally involved in the CDW development, leads to phonon dispersions like that in Fig. 4.6a. This has been observed in several compounds, see e.g. Refs. [200, 202]. Even though the phenomenological observation does not

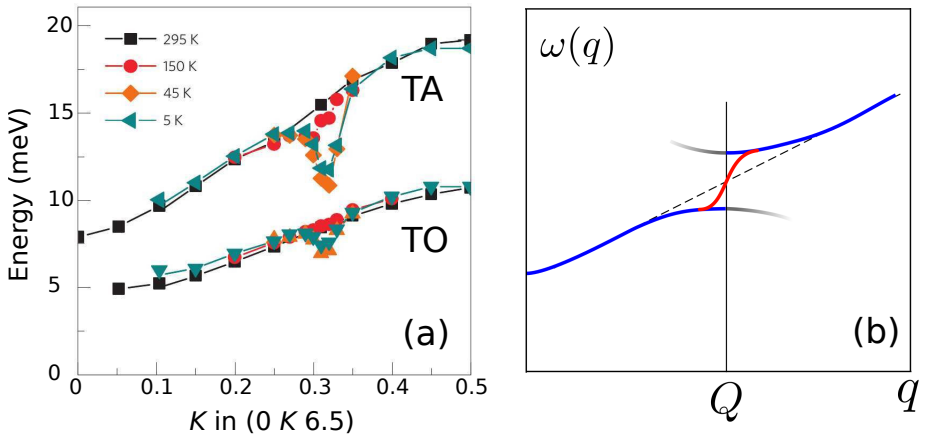

Figure 4.6: **(a)**: Phonon anomaly (dip) in the dispersion of transverse acoustic (TA) and transverse optical (TO) modes at $\mathbf{q} = (0, Q, 6.5)$ in $YBa_2Cu_3O_{6.6}$ [193]. **(b)** The expected phonon dispersion in the "electronic scenario". Blue solid lines show the dispersion in a perfect long-range CDW, grey lines represent the shadow bands. For a finite CDW correlation length the shadow bands practically disappear and solid blue lines become connected by the red solid line.

explain the mechanism of the CDW in underdoped cuprates, the observation poses a significant challenge to theoretical models based on "the electronic scenario" of the CDW formation. Furthermore, the phonon softening is generally expected in the "Kohn/Peierls scenario", which is likely to be the case in YBCO. At the same time our arguments in favour of the "Kohn/Peierls scenario" are not quite conclusive. Indeed, it seems that the "Kohn/Peierls scenario" does not provide an explanation of the strong broadening of TA and TO phonon modes at $T < T_{CDW}$ [19], as well as it does not explain why the phonon softening appears only in superconducting state $T < T_c$. So the last point of our work is less solid than the main results concerning the amplitudes of the CDW. Nevertheless, we believe that the presented discussion of the "Kohn/Peierls scenario" versus "electronic scenario" is useful for future work on the microscopic mechanism of the CDW.

4.3.1 Ginzburg-Landau model of the CDW and phonon dispersion

Here we consider a simple phenomenological Ginzburg-Landau model of the CDW developed in purely electron sector. Phonons weakly interact with electrons and

follow the developed CDW as "spectators". This is the first scenario discussed in the main text. Our analysis below shows that the phonon softening data does not support this scenario.

Let us consider a quasi-one dimensional (stripe-like) CDW, we direct the x axis along the CDW wave-vector. The CDW can be represented as a collective bosonic mode (ψ) in the electronic system. The effective Ginzburg-Landau-like Lagrangian for the CDW mode ψ reads

$$\mathcal{L}_\psi = \frac{\dot{\psi}^2}{2} - \psi\frac{\hat{\Omega}^2}{2}\psi - \frac{\alpha}{4}\psi^4 \ , \tag{4.14}$$

where $\psi(r)$ is a variation of electron density, $\hat{\Omega}^2/2$ is operator of "stiffness" of the CDW mode, and $\alpha > 0$ is a self-action constant. In momentum representation Ω_q^2 is a simple function sketched in Fig. 4.7. Kinetic energy has minima at $q_x = \pm Q$,

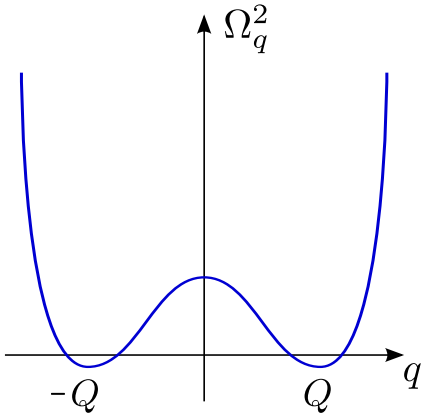

Figure 4.7: A sketch of the effective kinetic energy Ω_q^2 of the electronic CDW mode ψ.

and we can represent it as

$$\Omega_q^2 = \Omega_Q^2 + \kappa(q_x^2 - Q^2)^2/4, \tag{4.15}$$

where κ is a some constant. Importantly the minimal value of $\Omega_{\pm Q}^2$ is negative, $\Omega_{\pm Q}^2 < 0$, providing formation of the incommensurate CDW with the wave vector Q. The density variation is real, hence

$$\psi(x) = 2|\psi_Q|\cos(Qx + \phi), \tag{4.16}$$

here ψ_Q is a Fourier component of $\psi(r)$. In a perfect system the phase ϕ is arbitrary and this must result in a Goldstone sliding mode. Of course a disorder pins the phase. A similar phenomenological approach was successfully applied to describe a CDW state in transition-metal dichalcogenides [203].

To find the CDW amplitude one has to minimize the energy

$$E_\psi = \int d^2r \left(\psi \frac{\hat{\Omega}^2}{2} \psi + \frac{\alpha}{4} \psi^4 \right). \tag{4.17}$$

The saddle-point equation for static $\psi(r)$ reads

$$\hat{\Omega}^2 \psi + \alpha \psi^3 = 0. \tag{4.18}$$

Performing Fourier transform in Eqs. (4.18) and leaving only the dominating Fourier components with $q = \pm Q$ we find

$$|\psi_Q|^2 = -\Omega_Q^2 / 3\alpha. \tag{4.19}$$

To find the CDW excitation spectrum we expand energy (4.17) up to second order in fluctuations on the top of the ground state (4.16),(4.19),

$$\delta^2 E_\psi = \int d^2r \left(\delta\psi \frac{\hat{\Omega}^2}{2} \delta\psi + \frac{3\alpha}{2} \psi^2 (\delta\psi)^2 \right). \tag{4.20}$$

The term $\propto \psi^2 = |\psi_Q|^2 (2 + e^{2i(Qx+\phi)} + e^{-2i(Qx+\phi)})$ in (4.20) plays role of the effective potential with wave vector $2Q$ for the ψ-excitations. This results in a mixing between $\delta\psi_q$ and $\delta\psi_{q-2Q}$ (hereafter we assume that $q > 0$). Therefore, it is convenient to write the excitation energy as

$$\delta^2 E_\psi = \sum_q \Psi_q^\dagger \begin{pmatrix} \Omega_q^2 + 2|\Omega_Q^2| & |\Omega_Q^2| e^{2i\phi} \\ |\Omega_Q^2| e^{-2i\phi} & \Omega_{q-2Q}^2 + 2|\Omega_Q^2| \end{pmatrix} \Psi_q, \tag{4.21}$$

where

$$\Psi_q = \begin{pmatrix} \delta\psi_q \\ \delta\psi_{q-2Q} \end{pmatrix}.$$

Euler-Lagrange equation corresponding to (4.14), (4.21) results in the two normal modes: the sliding Goldstone mode and the gapped Higgs mode with the energies

$$\begin{aligned}
\epsilon_{Gq} &= \sqrt{\kappa Q^2}|p_x|, \\
\epsilon_{Hq} &= \sqrt{2|\Omega_Q^2| + \kappa Q^2 p_x^2} \\
\boldsymbol{p} &= \boldsymbol{q} - \boldsymbol{Q} \ .
\end{aligned} \tag{4.22}$$

The corresponding eigenmodes are

$$\begin{aligned}
G_q &= 1/\sqrt{2}(e^{i\phi}\delta\psi_q - e^{-i\phi}\delta\psi_{q-2Q}), \\
H_q &= 1/\sqrt{2}(e^{i\phi}\delta\psi_q + e^{-i\phi}\delta\psi_{q-2Q}).
\end{aligned} \tag{4.23}$$

Interestingly, due to the parabolic behaviour of Ω_q^2 near $q_x = \pm Q$, see Fig. 4.7, the weights of the states with wave vectors q and $q - 2Q$ in (4.23) are equal in a broad range of momenta around $q = \pm Q$.

The phonon is described by field φ, the phonon Lagrangian reads

$$\mathcal{L}_\varphi = \frac{\dot{\varphi}^2}{2} - \varphi\frac{\hat{\omega}^2}{2}\varphi, \tag{4.24}$$

where $\hat{\omega}^2/2$ is the elastic energy of lattice deformation. In momentum representation it is equivalent to the bare phonon dispersion ω_q. The CDW and phonons weakly interact, we describe the interaction by the Lagrangian

$$\mathcal{L}_{int} = -\lambda\psi\varphi \ , \tag{4.25}$$

where λ is coupling constant. Due to the coupling the CDW creates phonon condensate at $q_x = \pm Q$ (static lattice deformation) with amplitude $\varphi_Q = -\lambda/\omega_Q^2\,\psi_{-Q}$. Let us now consider phonon dispersion in the presence of the collective CDW mode. The interaction (4.25) in combination with Eqs (4.23) results in the following vertexes

describing transition of phonon to the Higgs and Goldstone modes of the CDW.

$$\langle \delta\varphi_q | H_q \rangle = \langle \delta\varphi_q | G_q \rangle = \frac{\lambda}{\sqrt{2}} e^{i\phi}$$
$$\langle \delta\varphi_{q-2Q} | H_q \rangle = -\langle \delta\varphi_{q-2Q} | G_q \rangle = \frac{\lambda}{\sqrt{2}} e^{-i\phi} \ .$$

This leads to normal and anomalous phonon self-energy operators shown in Fig. 4.8. The corresponding analytical expressions are

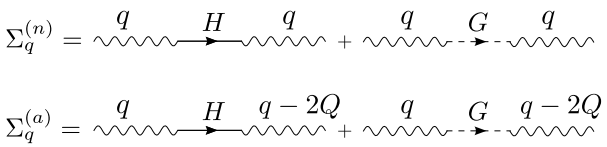

Figure 4.8: Normal and anomalous phonon self-energy

$$\begin{aligned}
\Sigma_q^{(n)} &= \frac{\lambda^2}{2}\left(\frac{1}{\omega_q^2 - \epsilon_{Hq}^2} + \frac{1}{\omega_q^2 - \epsilon_{Gq}^2}\right), \\
\Sigma_q^{(a)} &= e^{2i\phi}\Delta_q^2, \\
\Delta_q^2 &= \frac{\lambda^2}{2}\left(\frac{1}{\omega_q^2 - \epsilon_{Hq}^2} - \frac{1}{\omega_q^2 - \epsilon_{Gq}^2}\right).
\end{aligned} \tag{4.26}$$

A selfenergy generally depends on q and ω. In Eqs.(4.26) we set $\omega = \omega_q$. So "renormalized" dispersion $\widetilde{\omega}_q$ of phonons is described by the eigenvalue problem

$$\widetilde{\omega}_q^2 \Phi_q = \begin{pmatrix} \omega_q^2 + \Sigma_q^{(n)} & e^{2i\phi}\Delta_q^2 \\ e^{-2i\phi}\Delta_q^2 & \omega_{q-2Q}^2 + \Sigma_{q-2Q}^{(n)} \end{pmatrix} \Phi_q \ , \tag{4.27}$$

where

$$\Phi_q = \begin{pmatrix} \delta\varphi_q \\ \delta\varphi_{q-2Q} \end{pmatrix}. \tag{4.28}$$

As it is intuitively clear even without a calculation Eq. (4.27) is equivalent to scattering of phonon from some effective periodic potential with wave vector $2Q$.

One can represent matrix elements in (4.27) as

$$\begin{aligned}
&\sqrt{\omega_q^2+\Sigma_q^{(n)}} \approx w + cp_x, \\
&\sqrt{\omega_{q-2Q}^2+\Sigma_{q-2Q}^{(n)}} \approx w - cp_x, \\
&\Delta_q \approx \Delta \ ,
\end{aligned} \tag{4.29}$$

when the detuning $\boldsymbol{p} = \boldsymbol{q} - \boldsymbol{Q}$ is small. The speed c follows from the overall slope of the phonon dispersion. For the TO mode $w \approx 15$ meV, $c \approx 30$ meV/r.l.u., see Fig. 5a in the main text. The phonon dispersion which follows from (4.27) and (4.29),

$$\widetilde{\omega}_q^2 \approx w^2 \pm \sqrt{4w^2c^2p_x^2+\Delta^4} \ , \tag{4.30}$$

is shown in Fig.5b in the main text by the blue solid line. Shadow bands are indicated by fading grey lines. Expected intensity of the shadow bands is extremely small. Intensities of the bright (br) and shadow (sh) modes are

$$\begin{aligned}
I_{br} \propto |\delta\varphi_q|^2 &= \frac{1}{2}\left(1+\frac{2wcp_x}{\sqrt{4w^2c^2p_x^2+\Delta^2}}\right), \\
I_{sh} \propto |\delta\varphi_{q-2Q}|^2 &= \frac{1}{2}\left(1-\frac{2wcp_x}{\sqrt{4w^2c^2p_x^2+\Delta^2}}\right).
\end{aligned}$$

If the gap in the phonon spectrum ($gap \approx \Delta^2/w$) is 3 meV (TO mode), the intensity of the shadow mode practically diminishes at detuning $p_x = q_x - Q \geq 0.04$ r.l.u.

So far we disregarded temperature and intrinsic disorder. We remind the following experimental observations: (i) the CDW onset temperature is $T_{CDW} \sim 150$K, (ii) the CDW in low/zero magnetic fields is essentially two-dimensional, the correlation length in the c-direction is about one lattice spacing while the in-plane correlation length is $\xi_{a,b} \sim 20$ lattice spacings. In agreement with Mermin-Wagner theorem the observation (ii) implies that onset of the CDW at $T = T_{CDW}$ is not a true phase transition, it is a two-dimensional freezing crossover. Hence at $T > T_{CDW}$ the phase ϕ fluctuates with time and as a result the off-diagonal matrix element in Eq. (4.27) is averaged to zero, $e^{2i\phi}\Delta_q^2 \to 0$. Hence the phonon dispersion at $T > T_{CDW}$ near

$q_x = +Q$ is

$$\widetilde{\omega}_q = \sqrt{\omega_q^2 + \Sigma_q^{(n)}} \approx w + cp_x \ . \tag{4.31}$$

At $T < T_{CDW}$ the temporal fluctuations freeze, however due to the quenched disorder the phase $\phi(r)$ is a fluctuating function of coordinate r with the correlation length $\xi_{a,b}$. If $|p_x| > 1/\xi_{a,b} = 0.02$ r.l.u. the spatial fluctuations are not relevant and the phonon dispersion is given by Eq.(4.30). However, if the detuning is small, $|p_x| \ll 1/\xi_{a,b}$, one must average over spatial fluctuations of the phase ϕ effectively vanishing the off-diagonal matrix element, $e^{2i\phi}\Delta_q^2 \to 0$. This results in the red solid line connecting the blue solid lines in Fig. 5b in the main text.

All in all the phonon dispersion expected if the "electronic" scenario is realized is shown in Fig. 5b (main text). Obviously, the dispersion is inconsistent with the data. Therefore, we rule out the "electronic" scenario.

4.4 Conclusion

In conclusion, our analysis of available experimental data has resolved open problems in the phenomenology of the charge density wave (CDW) in underdoped cuprates. We have determined the amplitudes of s-, s'-, and d-wave components of the density wave. The amplitudes at low magnetic field and temperature $T = 60$K are given in Eq. (4.12), and the amplitudes for magnetic field $B = 30$T and temperature $T = 1.3$K are given in Eq. (4.13). We show that the data rule out a checkerboard pattern, and we also argue that the data might rule out mechanisms of the CDW which do not include phonons.

Chapter 5

Meron deconfinement and skyrmion/meron rings in frustrated magnets

In the present Chapter we study isolated topological defects (skyrmions and merons) in frustrated magnets with an easy axis/easy plane anisotropy. We demonstrate that skyrmions and meron pairs can exist in frustrated magnets in the absence of an external magnetic field and we find the conditions for stability of the skyrmions/merons. We show that isolated skyrmions in frustrated magnets possess unusual properties; the skyrmions attract each other and form skyrmion rings with a large topological charge. We found that in the presence of an easy plane anisotropy an elementary skyrmion with a unit topological charge becomes "fractionalized" into a pair of merons with a topological charge $1/2$ *per meron. The meron-meron confinement potential softens in the vicinity of the collinear-spiral phase transition that leads to deconfinement of merons at the critical point.*

5.1 Introduction

Some fifty years ago Tony Skyrme identified topologically stable "hedgehog"-like configurations of the meson field with baryons, such as proton and neutron.[72] The ensuing theoretical work showed that skyrmions indeed provide a semiquantitative

description of physical properties of baryons and their interactions [114].

Magnetic skyrmion are nanoscale topological defects in solids/magnetic films, that are characterized by a nonzero topological charge ("winding number"). A magnetic skyrmion has a number of unique properties including the following: (i) due to topological protection a skyrmion is a stable object, it can not be destroyed by any soft perturbations of the spin texture. (ii) A skyrmion can be manipulated and moved in a controlled way by ultra-low electric currents [105, 88], by an electric field [89] and a thermal gradient [100]. These properties make skyrmions attractive for developing skyrmion-based magnetic memory and data processing devices [106, 107, 109, 110].

In spite of a significant progress in the field, there are a few problems on the way to practical realization of skyrmion-based electronics. First, magnetic skyrmions have been experimentally observed only in handful of materials, where the main mechanism responsible for the formation of skyrmions is Dzyaloshinskii-Morya interaction. For future practical applications it is important to extend number of skyrmionic materials and find new physical mechanisms which support skyrmions. Second, in all known skyrmionic compounds an external magnetic field is necessary for stabilization of skyrmions and SkX phases. Finding a new material that hosts skyrmions in the absence of an external magnetic field would be highly desirable. A promising candidate for a novel skyrmionic material is a frustrated magnet. Recent studies predicted an existence of skyrmion crystals and isolated skyrmions in frustrated magnets in an external magnetic field [111, 112, 113].

In the present Chapter we show that in frustrated magnets with a weak easy axis/easy plane anisotropy an isolated skyrmion is stable even at zero magnetic field. We found that unlike the case of chiral magnets where skyrmions are repulsive [96], skyrmions in frustrated magnets can attract each other. The skyrmion-skyrmion attraction leads to energetic stability of new exotic topological objects, which we refer to as "skyrmion rings". Skyrmion rings are the skyrmions with large topological charges.

Interestingly, similar multi-skyrmion solutions of toroidal, tetrahedral and other peculiar shapes were used to model light atomic nuclei[115] and nuclear matter was described as a skyrmion crystal.[116] At high densities skyrmions forming the crystal

fractionalize into half skyrmions carrying half-integer baryon numbers.[117, 118]

A skyrmion with a unit topological charge can generally be represented as a bound state of two merons ("half-skyrmions") with a topological charge $|Q| = 1/2$ per meron. The concept of a meron originates from nuclear physics, where merons were invented for description of quark confinement in hadrons [121]. Merons can exist only in pairs due to their fractional topological charge, hence the merons are tightly confined within the radius of a skyrmion. The confinement potential increases with increasing distance between the merons, analogous to the quark confinement in QCD [122]. Merons have been elusive from a direct detection, however they were predicted to have many manifestations in condensed matter systems, such as meron phases in quantum Hall systems [123], bilayer graphene [124] and chiral magnets[125, 127].

In the present Chapter we demonstrate that meron pairs can be observed in frustrated magnets with an easy plane anisotropy. Moreover, we show that merons become spatially separated in the vicinity of a phase transition from FM to a spiral state. We show that the meron-meron potential at large meron-meron distances becomes finite at the critical point. At the critical point merons can be separated from each other by an arbitrary large distance with a small energy cost and therefore become "deconfined".

In order to clarify the semantics, we want to emphasise that the terms "skyrmion" and "meron pair" are used as synonyms in the present Chapter. The both terms refer to a compact topological objects with a unit topological charge - skyrmion. However, we will mostly use the term "skyrmion" in the case of magnets with easy axis anisotropy and "meron pair" in the case of magnets with easy plane anisotropy. The reasons for this naming convention are as follows: (i) the skyrmion spin configuration and topological charge density are quite anisotropic in the systems with easy plane anisotropy. Description of a skyrmion as a bound state of two merons is very natural in this case. (ii) The deconfinement of merons is possible only in the magnets with an easy plane anisotropy, whereas in the magnets with an easy axis anisotropy the merons are always confined inside of a skyrmion.

The Chapter is organized as follows. In Section 5.2 we introduce a model of a Heisenberg frustrated magnet on the square lattice. In Sec. 5.3 we find skyrmion

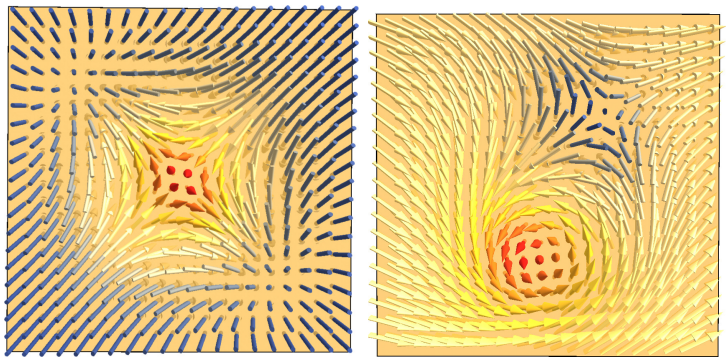

Figure 5.1: (Left panel) An isolated skyrmion in a frustrated magnet in the presence of an easy axis anisotropy. (Right panel) A pair of merons in a frustrated magnet in the case of easy plane anisotropy. The arrows represent a direction of spin in a 2D lattice, the color shows the z-component of spin.

solutions at zero magnetic field in the presence of an easy axis anisotropy and we develop a variational description of the skyrmion. In Section 5.4 we analyse skyrmions in the case of easy plane anisotropy and show how skyrmion becomes fractionalized in the vicinity of a phase transition to a spiral state. In Section 5.5 we calculate the skyrmion-skyrmion interaction potential, and show that the skyrmions can form giant skyrmion rings with a large topological charge. Finally, we summarize our results in Section 5.6.

5.2 Model

We consider a classical Heisenberg model for a frustrated magnet (at zero temperature) on the square lattice with competing interactions and a single ion onsite anisotropy. The Hamiltonian of the model reads

$$H = -J_1 \sum_{\langle i,j \rangle} \mathbf{S}_i \cdot \mathbf{S}_j + J_2 \sum_{\langle\langle i,j \rangle\rangle} \mathbf{S}_i \cdot \mathbf{S}_j + J_3 \sum_{\langle\langle\langle i,j \rangle\rangle\rangle} \mathbf{S}_i \cdot \mathbf{S}_j - \frac{K}{2} \sum_i \left(S_i^z\right)^2, \qquad (5.1)$$

where $\boldsymbol{S}_i$ is the spin of a unit length ($\boldsymbol{S}_i^2 = 1$) at the lattice site i, $J_{1,2,3}$ are the Heisenberg exchange couplings, where J_1 is ferromagnetic and $J_{2,3}$ are antiferromagnetic couplings ($J_{1,2,3} > 0$). The coefficient K characterizes the spin anisotropy, positive (negative) K corresponds to the case of easy-axis (easy-plane) anisotropy.

Notation $\langle i,j\rangle$, $\langle\langle i,j\rangle\rangle$ and $\langle\langle\langle i,j\rangle\rangle\rangle$ in Eq. (5.1) denotes summation over the nearest, next nearest and next-next nearest neighbour sites. Hereafter we set the energy scale putting $J_1 = 1$.

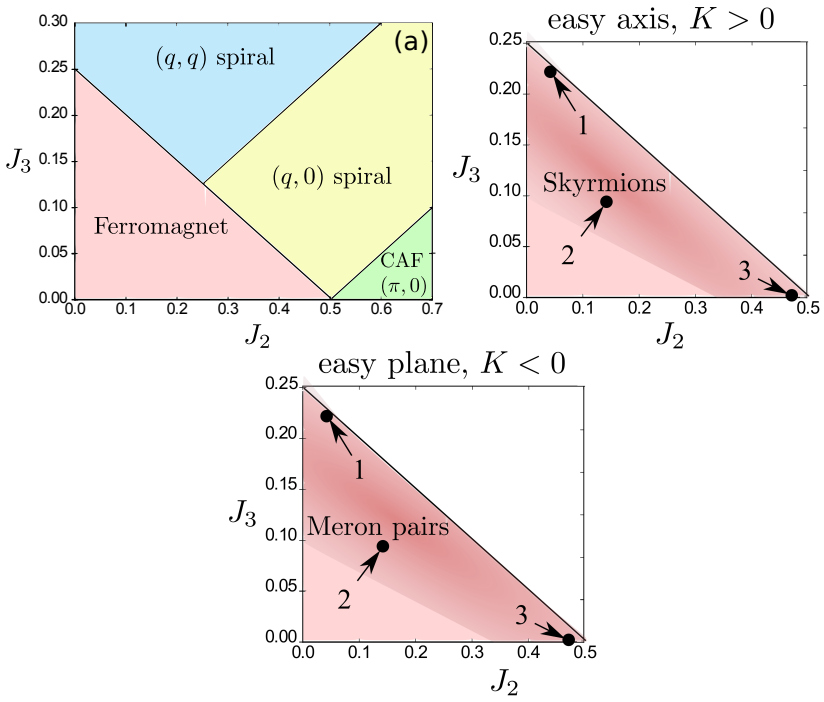

Figure 5.2: (a) $J_2 - J_3$ phase diagram of the square lattice frustrated magnet with easy axis/easy plane anisotropy for $|K| \ll 1$ (see Ref. [204]). With increase of $|K|$ the phase boundaries become slightly shifted. (b,c) Stability diagrams for isolated skyrmions and meron pairs with the topological charge $Q = 1$. Here $K = 10^{-3}$ for panel (b) and $K = -10^{-3}$ for panel (c). The Heisenberg couplings J_2, J_3 and magnetic anisotropy K are measured in units of nearest FM exchange coupling $J_1 = 1$.

The model of a frustrated magnet described by Hamiltonian (5.1) has four possible ground states, see Fig. 5.2a: (i) a collinear ferromagnetic (FM) state, (ii) a horizontal or vertical spiral phase with the ordering wave vector $\boldsymbol{q} = (q,0)$ or $(0,q)$ and (iii) a diagonal spiral phase with $\boldsymbol{q} = (q,\pm q)$, (iv) a columnar antiferromagnetic phase (CAF) with the ordering vector $\boldsymbol{q} = (0,\pi)$ or $(\pi,0)$. The $J_2 - J_3$ phase diagram in the case of a zero spin anisotropy $K = 0$ is discussed in Ref. [204] and in the case of finite K the phase diagram is similar and is analysed in Appendix 5.7.1. The phase diagram presented in Fig. 5.2a corresponds specifically to the case of a very small spin anisotropy. Hereafter we will be interested only in the regime of

small $|K| \ll 1$ because, as we will show below, the topological defects (skyrmions and merons) can exist in the frustrated magnet only in this regime.

In order to study skyrmions and merons it is convenient to consider Hamiltonian (5.1) in the continuous limit (see e.g. Ref.[205])

$$E = \frac{1}{2}\int d^2r \left[\rho(\partial_i S_\mu)^2 + b_1\{(\partial_x^2 S_\mu)^2 + (\partial_y^2 S_\mu)^2\} + b_2 \partial_x^2 S_\mu \partial_y^2 S_\mu + K(1 - S_z^2)\right], \tag{5.2}$$

where $\rho = J_1 - 2J_2 - 4J_3$, $b_1 = 1/12(-J_1 + 2J_2 + 16J_3)$ and $b_2 = J_2$. In Eq. (5.2) the index $i = x, y$ and we assume that the z-axis is perpendicular to the $\{xy\}$ plane of the lattice, x and y are directed along the main crystallographic axes of the square lattice. Of course, the continuous approximation (5.2) is valid only when the spatial derivatives in (5.2) are small: $\partial_i S_\mu \ll 1$ and $\partial_i^2 S_\mu \ll 1$.

The first term in the field model (5.2) corresponds to a standard $O(3)$ nonlinear sigma model (NLσ) with the spin stiffness $\rho > 0$. Note, that if the frustration is strong enough (the couplings J_2 and J_3 are sufficiently large), the spin stiffness ρ can change sign and become negative. The change of the sign of spin stiffness indicates a Lifshiz point corresponding to a transition from a collinear FM state to a spiral state. The high-order derivative terms in (5.2) proportional to $b_{1,2}$, enforce stabilization of the system's energy for $\rho < 0$ and determine the incommensurate wave vector $\boldsymbol{q}$ of the spiral ground state. Throughout the Chapter we will be mostly interested in the regions of the phase diagram in Fig. 5.2 in the vicinity of the FM-spiral phase boundary ($\rho \ll 1$).

5.3 Isolated skyrmions

In the present Section we analyse static properties of isolated skyrmions in the FM phase of the $J_1 - J_2 - J_3$ model with an easy axis anisotropy, $K > 0$. For this analysis we use the continuum approximation (5.2) and also perform full 2D numerical simulations of the original lattice model (5.1) solving Landau-Lifshitz-Gilbert equation with a damping term (for details see Appendix 5.7.2).

The continuum model (5.2) is a generalization of the NLσ model. The standard $O(3)$ NLσ model $E = \rho/2 \int d^2r (\partial_i S_\mu)^2$, which is a long wavelength field model of

a collinear ferromagnet, has well known topological solutions known as Belavin-Polyakov (BP) skyrmions [83]. Such skyrmions exist as excitations above a FM background, where the energy of a skyrmion with a topological charge Q reads $E_Q = 4\pi\rho|Q|$. Since NLσ model in two spatial dimensions is conformally invariant, the BP skyrmion has no internal scale, and therefore the energy of the skyrmion does not depend on size of the skyrmion.

On the other hand, the field theory (5.2) for the frustrated magnet has additional high order derivative terms originating from frustration ($\propto b_1$ and $\propto b_2$) and the spin anisotropy term ($\propto K$). Following Derrick's scaling arguments [210] it is easy to see that Eq. 5.2 supports 2D static skyrmions. The balance between frustration and magnetic anisotropy provides a characteristic spatial scale for the skyrmions and leads to stabilization of skyrmions.

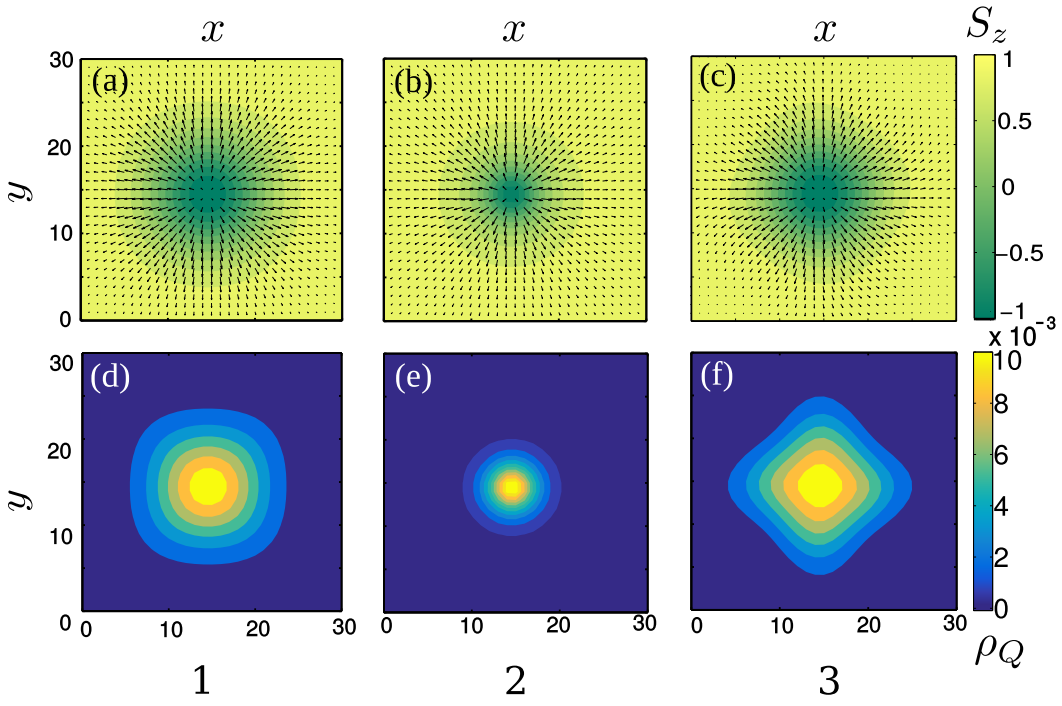

Figure 5.3: (a-c) Skyrmions in the frustrated magnet with easy axis anisotropy ($K > 0$), corresponding to the points $1, 2, 3$ on the phase diagram in Fig. 5.2b. Arrows show S_x and S_y components of the spin, color indicates S_z. (d-f) Profiles of topological density $\rho_Q(x, y)$, Eq. (5.6), of the skyrmions.

Static properties of an isolated skyrmion can be quantitatively understood within a variational approach. It is worth mentioning that the model (5.2) is not invariant

under the group of spatial rotations in the $\{xy\}$ plane. The rotational invariance is broken due to the terms with the second spatial derivatives (the invariance is restored in a very special case $b_2 = 2b_1$). Instead, the model (5.2) in a general case respects only a discrete C_4 symmetry of the underlying square lattice model (5.1). For the sake of simplicity we will ignore the spatial anisotropy of the skyrmions and treat them as radially symmetric. The variational ansatz for skyrmionic solution with a topological charge $Q = 1$ reads

$$S_\mu = (\sin\theta(r)\cos(\phi+\chi),\ \sin\theta(r)\sin(\phi+\chi),\ \cos\theta(r))\,, \tag{5.3}$$

where $\{r, \phi\}$ are the polar coordinates in the $\{xy\}$ plane with the origin at the center of skyrmion, and χ is a helicity angle of the skyrmion. The radially symmetric ansatz is described by a single function $\theta(r)$ with the boundary conditions $\theta(0) = \pi$ and $\theta(\infty) = 0$. The ansatz for an antiskyrmion ($Q = -1$) can be written in the form (5.3) with the substitution $\phi \to -\phi$.

In order to find a skyrmionic solution minimizing the energy (5.2) we use a probe function $\theta(r) = \pi\exp(-r/R)$ which satisfies the boundary conditions, where R is the variational parameter and corresponds to the radius of the skyrmion. Substituting this ansatz in (5.2), we obtain

$$E_{sk}[R] = \rho I_\rho + \frac{b_1 I_{b1} + (b_2 - 2b_1) I_{an}}{R^2} + K I_K R^2. \tag{5.4}$$

The integrals I_ρ, I_{b1}, I_{an} and I_K are dimensionless constants and can be calculated numerically (see Appendix 5.7.3). The variational energy (5.4) has a minimum as a function of R at optimal radius of the skyrmion $R_0 = \left(\frac{b_1 I_{b1} + (b_2-2b_1) I_{an}}{K I_K}\right)^{1/4}$. The radius of skyrmions $R \gg 1$ is large at small values of the spin anisotropy K (although the dependence R on K is very weak, $R \propto 1/K^{1/4}$). The variational energy of a skyrmion with $|Q| = 1$ is equal to

$$E_{sk}[R_0] = \rho I_\rho + 2\sqrt{b_1 I_{b1} + (b_2 - 2b_1) I_{an}}\sqrt{K I_K}. \tag{5.5}$$

The energy of a skyrmion is positive provided that the skyrmion is an excitation above the FM ground state. The skyrmion energy (5.5) does not depend on the

helicity angle χ due to a global $O(2)$ rotational symmetry of the Hamiltonian (5.1) in the spin space (S_x, S_y). Taking the formal limit $b_1 = b_2 = K = 0$ in Eq. (5.5), that corresponds to the $O(3)$ nonlinear sigma model, we obtain the estimate for the energy of a BP skyrmion. Our variational ansatz for the skyrmion with $|Q| = 1$ gives $E_{sk} = \rho I_\rho \approx 13.17\rho$ that overestimates the exact result $E_{sk} = 4\pi\rho$ by 5%.

In Fig. 5.3 we plot some typical skyrmion solutions, obtained numerically by solving Landau-Lifshitz-Gilbert equation for the the original 2D square lattice model (5.1). The details of the numerical procedure are explained in Appendix 5.7.2. We plot the corresponding spin configurations of the skyrmions (see Fig. 5.3(a,b,c)) and the topological charge density

$$\rho_Q(x, y) = \frac{1}{4\pi} \boldsymbol{S}[\partial_x \boldsymbol{S} \times \partial_y \boldsymbol{S}] \tag{5.6}$$

(see Fig. 5.3(d,e,f)). One can see that in the limit $K \ll 1$ and sufficiently close to the FM-spiral boundary line in Fig. 5.2(b), the skyrmion size can be much greater than the lattice spacing in agreement with our variational analysis. The shape of a skyrmion is controlled by parameters ρ, b_1 and b_2. When $\rho(\partial_i S_\mu)^2$ is a dominant term in (5.2) the skyrmion is axially symmetric, i.e. round-shaped, see Fig. 5.3(b,e). If the term $b_1\{(\partial_x^2 S_\mu)^2 + (\partial_x^2 S_\mu)^2\}$ is dominant, the skyrmion is square-shaped, the diagonals of the square are oriented along $(1, \pm 1)$ crystal axes, see Fig. 5.3(a,d). Finally, if $b_2 \partial_x^2 S_\mu \partial_y^2 S_\mu$ is the dominant term, the skyrmion is also square-shaped, the diagonals of the square are oriented along $(1, 0)$ and $(0, 1)$ crystal axes which is apparent in Fig. 5.3c,f.

It is important that skyrmions are stabilized only if the values of antiferromagnetic exchange couplings are large enough, and can not be stabilized in a normal unfrustrated ferromagnet. At small values of $J_{2,3}$ skyrmions are shrinking to a radius comparable to the lattice constant. We calculated numerically the skyrmion stability region (for skyrmions on the FM background); the result is presented in Fig. 5.2b,c (for the details of the numerical calculations see Appendix). At the border of the stability region skyrmions have a radius of approximately one lattice spacing, outside of the stability region a skyrmion collapses into a point. The skyrmions can exist only for sufficiently small values of magnetic anisotropy (see Fig. 5.4) that

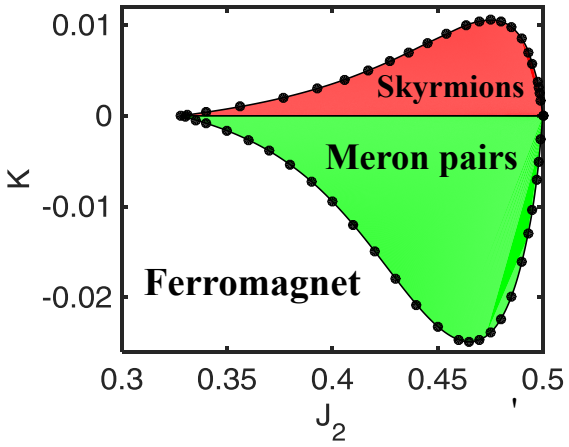

Figure 5.4: $J_2 - K$ stability diagram for skyrmions and meron pairs ($J_3 = 0$).

provides a limitation for potential candidates for the skyrmionic materials based on frustrated magnets. Interestingly skyrmions (and meron pairs) can exist in the spiral phase of a frustrated magnet, however in the present Chapter we do not discuss topological excitations on a spiral background.

According to Eq. (5.5) skyrmions are stabilized only if the condition $b_1 I_{b1} + (b_2 - 2b_1) I_{an} > 0$ is fulfilled, otherwise the energy (5.5) becomes unbounded from below at $R \to 0$ and the skyrmion shrinks to the radius comparable to the lattice constant. This condition provides a stability domain on the $J_2 - J_3$ diagram for isolated skyrmions in qualitative agreement with the "Skyrmion" region in Fig. 5.2b.

In Fig. 5.5 we present a comparison of numerical results for skyrmion energy obtained by full 2D simulations (blue line) with the results of the variational ansatz (5.5) (red line). We see a good agreement between the numerical and variational results. However, the accuracy of the variational ansatz (5.5) goes down with increasing K (Fig. 5.5, right panel), since the skyrmion size is decreasing as $R \propto 1/K^{1/4}$ and the continuous approximation (5.2) becomes less accurate.

We would like to stress, that the isolated skyrmions in a frustrated magnet can exist at zero magnetic field. Applying magnetic field along the z axis, on the contrary, will raise the energy of a skyrmion by $\Delta E \propto R^2 B_z$ and will decrease the size of the skyrmion. For sufficiently large values of the magnetic field the size of

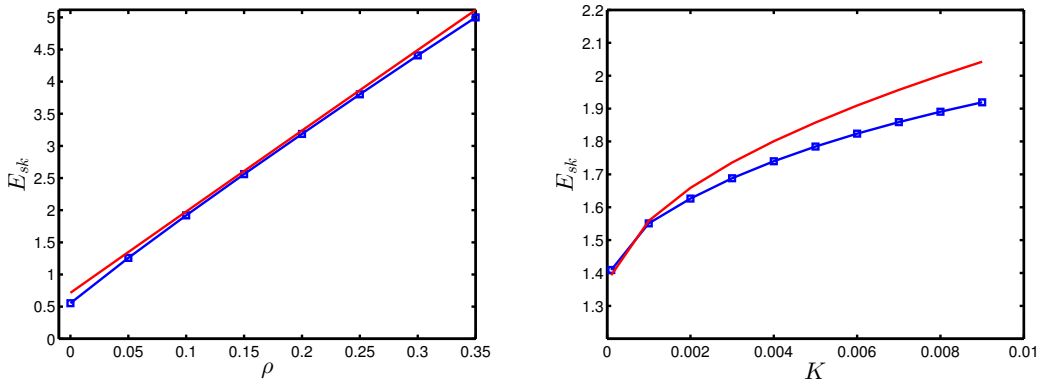

Figure 5.5: Energy of a skyrmion versus (left panel) spin stiffness $\rho = J_1 - 2J_2 - 4J_3$, (right panel) the strength of easy-axis anisotropy K. The energy is measured in units of J_1, we set $J_1 = 1$. The blue line in left and right panels corresponds to numerical solution of 2D Landau-Lifshitz-Gilbert equation. The red line corresponds to results of variational ansatz (5.5). The parameters of the model are (left panel) $J_3 = 0.05$, $K = 5 \cdot 10^{-3}$, (right panel) $J_2 = 0.45$, $J_3 = 0$.

a skyrmion becomes comparable to one lattice spacing and eventually shrinks to a zero radius.

5.4 Meron pairs and deconfinement of merons

In the present Section we consider topological excitations in the $J_1 - J_2 - J_3$ frustrated magnet in the presence of an easy plane anisotropy. In this case the vector of magnetization of the FM ground state lies in the $\{xy\}$ plane and the FM ground state spontaneously breaks the $O(2)$ inplane spin rotational symmetry of the system. Let us choose the direction of the uniform magnetization in the FM state to be along x-axis, $S_x = 1$. A topological defect in this case should obey the boundary condition $S_x(r \to \infty) \to 1$. A skyrmionic excitation on the top of the inplane FM background can be constructed by global rotaion of a skyrmion shown in Fig. 5.3 in the $\{xz\}$ plane on the angle $\pi/2$: $(S_x, S_y, S_z) \to (S_z, S_y, -S_x)$.

Typical spin configurations for such skyrmions, obtained numerically by solving Landau-Lifshitz-Gilbert equations for the lattice model (5.1), are presented in Fig. 5.6 (a,b,c). A skyrmion with topological charge $Q = 1$ in the case of an easy plane anisotropy is convenient to represent as a bound pair of two merons with the

topological charge $Q = 1/2$ per meron, see Fig. 5.6(a,b,c). The spin in the center of a meron is directed along z axis and the spin outside of the meron core is inplane.

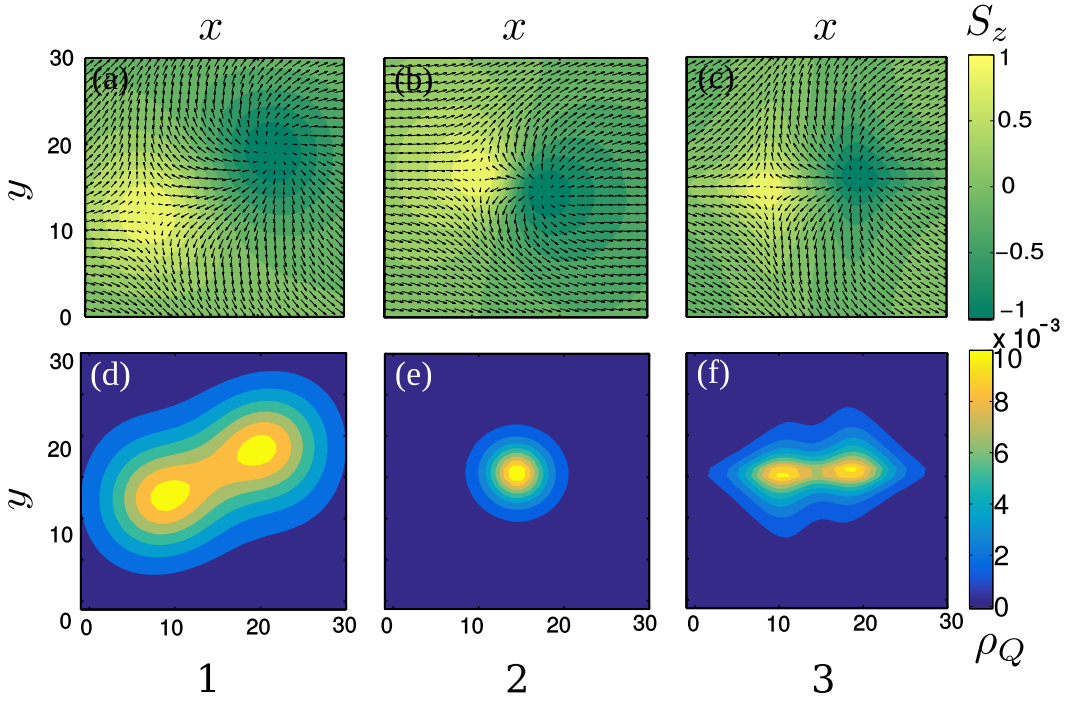

Figure 5.6: (a-c) Meron pairs in the frustrated magnet in the presence of easy plane anisotropy $K < 0$. The plots correspond to the $(1, 2, 3)$ points on the phase diagram in Fig. 5.2c. (d-f) Topological density ρ_Q for the spin configurations in (a-c). The frustrated magnet in panels (a,d) and (c,f) is close to the FM-spiral phase boundary, that results in the topological fractionalization and a spatial separation of merons.

A variational description for a round-shaped meron pair configuration with isotropic topological density profile (as the meron pair in Fig. 5.6(b,e)) can be developed by analogy with Sec. 5.3. The variational energy and the size of the meron pair coincide with the results for a skyrmion in Sec. 5.3 after the substitution $K \to |K|$ as discussed in Appendix 5.7.4. This explains why the $J_2 - J_3$ and $J_2 - K$ stability diagrams for skyrmions ($K > 0$) and meron pairs ($K < 0$) are quite similar, see Fig. 5.2b,c and Fig. 5.4.

In the vicinity of the phase transition between FM and spiral phases we observe a spatial splitting of merons, shown in Fig. 5.6 (a,d,c,f). The spatial splitting of merons results in the emergence of two peaks in the topological density profile, see Fig. 5.6 (d,f). Each meron has a topological charge 1/2, so this splitting can be

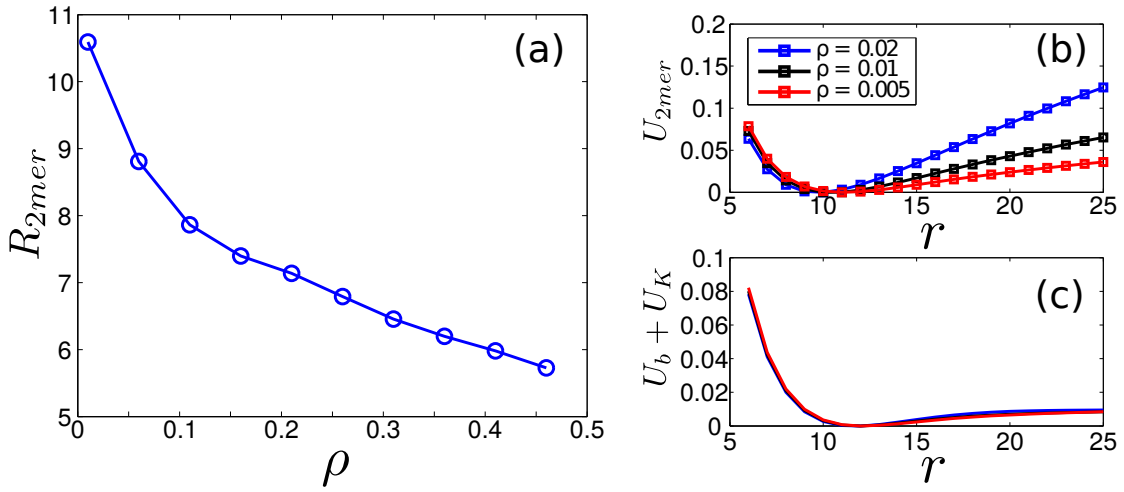

Figure 5.7: (a) Distance between the centers of merons R_{2mer} versus spin stiffness. The distance R_{2mer} increases while approaching the critical point $\rho = 0$, resulting in a "fractionalization" of a topological charge near the critical point. (b) The meron-meron interaction potential U_{2mer} versus the distance between merons. (c) The potential $U_b + U_K$ versus meron-meron distance. The model parameters are $K = -5 \cdot 10^{-3}$, $J_3 = 0.1$. The minimum of the potential energy curves is shifted to zero.

considered as a fractionalization of a skyrmion into a pair of half-skyrmions - merons.

The fractionalization of a meron pair near the critical line can be understood by analysing a meron-meron interaction potential. The confinement potential between merons at large meron-meron separations $r \gg r_0$ grows logarithmically

$$U_{2mer}(r) = 2\pi\rho \ln(r/r_0) + \mathcal{O}(1), \tag{5.7}$$

where r_0 is the radius of a meron core. The asymptotic formula (5.7) can be obtained using a method described in Ref. [113] and it coincides with the meron-meron potential in the $O(3)$ NLσ model [122].

The potential energy of meron-meron interaction $U_{2mer}(r)$ versus the distance between the centers of the merons is presented in Fig. 5.7(b). The potential energy has a hard core repulsion at short distances and logarithmically grows at large distances in agreement with Eq. 5.7. At small values of the spin stiffness $\rho \ll 1$ (near the phase boundary separating FM state and spiral states) the confinement potential becomes softened. The softening of the potential at $\rho \to 0$ leads to spatial

splitting of merons, shown in Fig. 5.6 (a,d,c,f).

The interaction potential U_{2mer} can be formally split in three components corresponding to the four terms in Eq. (5.2):

$$U_{2mer}(r) = U_\rho(r) + U_b(r) + U_K(r) - E_{2mer}, \tag{5.8}$$

where the contributing terms are

$$U_\rho = \frac{\rho}{2}\int d^2r(\partial_i S_\mu)^2, \quad U_b = \int d^2r\left(b_1\{(\partial_x^2 S_\mu)^2 + (\partial_y^2 S_\mu)^2\} + b_2\partial_x^2 S_\mu \partial_y^2 S_\mu\right),$$
$$U_K = -K\int d^2r(S_z)^2. \tag{5.9}$$

Here S_μ is the exact solution for the two-meron configuration separated by a distance r. In order to calculate the interaction potential we fix the spins in the centers of merons as $S_z = \pm 1$. In the definition of the potential U_{2mer} we subtract the energy E_{2mer} of the equilibrium two-meron configuration.

Since the confinement potential $U_\rho \propto 2\pi\rho \ln r$, vanishes as $\rho \to 0$, the only contribution to the meron-meron interaction potential in the vicinity of the critical line reads $U_{2mer}(r) \to U_b(r) + U_K(r)$. The potential at large distances $r \gg r_0$ scales as $U_b(r) \propto 1/r^2$. On the other hand the spin anisotropy component of the potential $U_K(r) \to const$ at $r \gg r_0$, since outside of the meron cores the spins lie within the $\{xy\}$ plane, the value of the *const* is determined by the contributions of meron cores. Moreover, the sum of the two contributions $U_b(r) + U_K(r)$ has a minimum in the vicinity of the critical line $\rho \to 0$, see Fig. 5.7c. The potential $U_b(r) + U_K(r)$ determines the size of a meron pair near the critical line.

In Fig. 5.7(a) we show how the distance between the centers of the merons grows while approaching a critical line $\rho \to 0$. The centers of each meron are defined as the positions $(x_0^\pm, y_0^\pm)$ of maxima (minima) in $S^z(x, y)$. In order to increase accuracy of calculation of R_{2mer} we perform a local polynomial interpolation of $S^z(x, y)$ near the points $(x_0^\pm, y_0^\pm)$ and find the extrema points of the interpolated function. The distance $R_{2mer}(\rho)$ does not diverge as $\rho \to 0$ and approaches to a finite value at the critical point.

Since the potential $U_{2mer}\big|_{\rho\to 0} \to U_b + U_K$ remains finite at large distances at the

critical line, the energy required to dissociate a meron pair is also finite (see Fig. 5.7(c)). Therefore exactly at the critical line the merons become "deconfined", meaning the absence of confinement at large distances. Note, that meron pairs do not break into individual merons even at the critical point. However pumping a relatively small amount of energy into the system, it is possible to separate merons on an arbitrary distance.

Note that the fractionalization/deconfinement of a skyrmion occurs only in the case of an easy-plane anisotropy. A skyrmion solution in the case of $K > 0$ has only a single peak in the topological charge density even when $\rho \to 0$ and does not split into a pair of merons. The difference between the cases of $K > 0$ and $K < 0$ is in the U_K contribution to a meron-meron interaction potential. In the case of an easy-plane anisotropy the "fractionalization" is possible because with increasing the distance $r \to \infty$ between merons ($S_z = \pm 1$ in the centers of merons) the potential $U_K(r) \to const$. It is possible separate the merons (at $\rho = 0$) on the large distances, because one can encompass a path around a meron, such that $\boldsymbol{S}$ is inplane along the path. On the other hand a spatial separation of merons in the case of an easy axis anisotropy (e.g. $S_x = \pm 1$ in the centers of merons) is energetically unfavourable due to the U_K term. The spin anisotropy energy U_K linearly grows with the distance r between the compact merons due to a "string" of nearly inplane spins. Along any path encompassing a meron the z projection of spin will change from $S_z = -1$ to $S_z = 1$ which will give rise to an increasing with r contribution to the energy U_K.

5.5 Skyrmion-skyrmion attraction and skyrmion (meron) rings

Interaction potential of two isolated skyrmions in a 2D frustrated magnet has been considered in Refs. [112, 113], where it was shown that the asymptotics for the interaction potential $U_{12}(r)$ between two skyrmions as a function of interskyrmion distance r reads

$$U_{12}(r) \propto \cos(\chi_1 - \chi_2) Re[\exp(-\sqrt{\kappa^2 + \mu^2} r) + i(\sqrt{\kappa^2 - \mu^2} r + \phi)]. \tag{5.10}$$

Here $\kappa^2 = 1/2\sqrt{K/b_1}$ and $\mu^2 = \rho/4b_1$, and $\chi_{1,2}$ are helicities of the first and the second skyrmion. The spatial anisotropy term $\propto (b_1 - 2b_2)$ presented in (5.2) is neglected in the interaction potential (5.10). If the spin stiffness ρ is negative the interaction potential $U_{12}(r)$ in Eq. (5.10) exhibits oscillations with r, which was numerically demonstrated in Refs. [112, 113]. The FM ground state for $\rho < 0$ was stabilized by an external magnetic field along z axis. The oscillating behaviour of $U_{12}(r)$ in this case leads to an overall repulsion between skyrmions.

In the present Section we show that skyrmions in frustrated magnets can also exhibit attraction. The r-oscillations of $U_{12}(r)$ are suppressed by the exponent in (5.10) in the case when $\rho > 0$. Moreover, in the regime $\rho > 2\sqrt{Kb_1}$ (or $\mu^2 > \kappa^2$) the exponent in (5.10) becomes real and the potential has a definite sign

$$U_{12}(r) \propto \cos(\chi_1 - \chi_2) \exp\left(-[\sqrt{\kappa^2 + \mu^2} - \sqrt{\mu^2 - \kappa^2}]r\right). \tag{5.11}$$

In the case of skyrmions with equal helicitles $\chi_1 = \chi_2$ the potential $U_{12}(r)$ is repulsive. For the case of skyrmions with "opposite" helicities $\chi_1 - \chi_2 = \pi$ the potential is attractive. We numerically calculate the interaction potential of two skyrmions (in the regime $\rho > 2\sqrt{Kb_1}$) with equal/"opposite" helicities, see Fig. 5.8. To calculate the interaction energy we fix the spins in the centers of the skyrmions, $S_z = -1$. The long distance behaviour of $U_{12}(r)$ in Fig. 5.8 qualitatively agrees with the prediction (5.11). The most interesting case is the case of "opposite" helicities, when $U_{12} < 0$ is attractive. The possibility of attractive interaction between skyrmions in frustrated magnets was also pointed out in Ref. [209].

At very short distances $r < R$ (R is the radius of a skyrmion) the cores of skyrmions start to overlap and the attraction changes to a repulsion. The skyrmions merge at $r < R$ and form a skyrmion-skyrmion bound state with topological number $Q = 2$.

The attractive nature of the interskyrmion potential $U_{12}(r)$ make possible a formation of stable giant skyrmions with large topological numbers. In Fig. 5.9(a) we plot spin configurations of skyrmions with topological charges $Q = 1, 2, 3$. The multi-Q skyrmions have been obtained by merging several elementary skyrmions with $Q = 1$. The energy of a multi-Q skyrmion is smaller then the total energy of

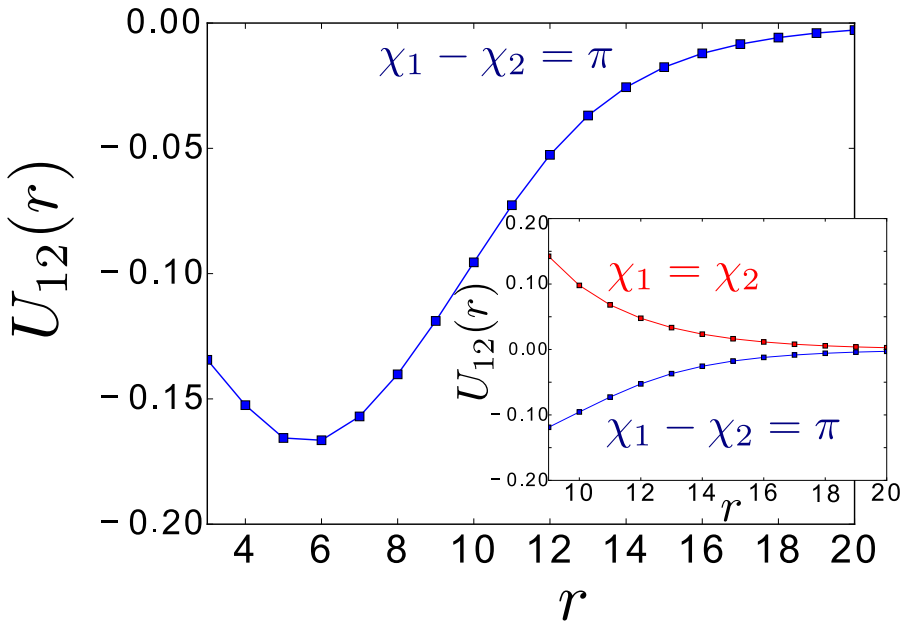

Figure 5.8: Potential energy $U_{12}(r)$ of interaction between two skyrmions as a function of distance between the centers of the skyrmions. The red line corresponds to the case of equal helicities $\chi_1 = \chi_2$, the blue line corresponds to $\chi_1 - \chi_2 = \pi$. We use following set of parameters $J_2 = 0.2$, $J_3 = 0.149$, $K = 0.01$.

Q isolated skyrmions and can be considered as their bound state. The energy of the multy-Q bound state per skyrmion $E_Q/|Q|$ decreases with $|Q|$ (see Fig. 5.9(b)) that indicates about a tendency of the skyrmions to aggregate in giant skyrmions with a large topological charge. The fact that $U_{12}(r)$ has minimum at $r = r_0$ (see Fig. 5.8) suggests that the skyrmion with a large Q occupies the area $\sim Q\pi r_0^2$, so that the skyrmion radius $R \sim r_0 Q^{1/2}$. Surprisingly, this is not the case: the topological charge and energy densities of the multi-Q skyrmion are concentrated in a ring of radius $R \sim r_0 Q$ (see Figs. 5.10(a,c)).

Figure 5.9b shows that the energy per skyrmion, E_Q/Q, decreases with increasing Q and approaches a constant, because the width of the ring and the length of the ring segment occupied by one skyrmion become Q-independent. The energy of skyrmion in the ring is significantly lower than that of the elementary skyrmion.

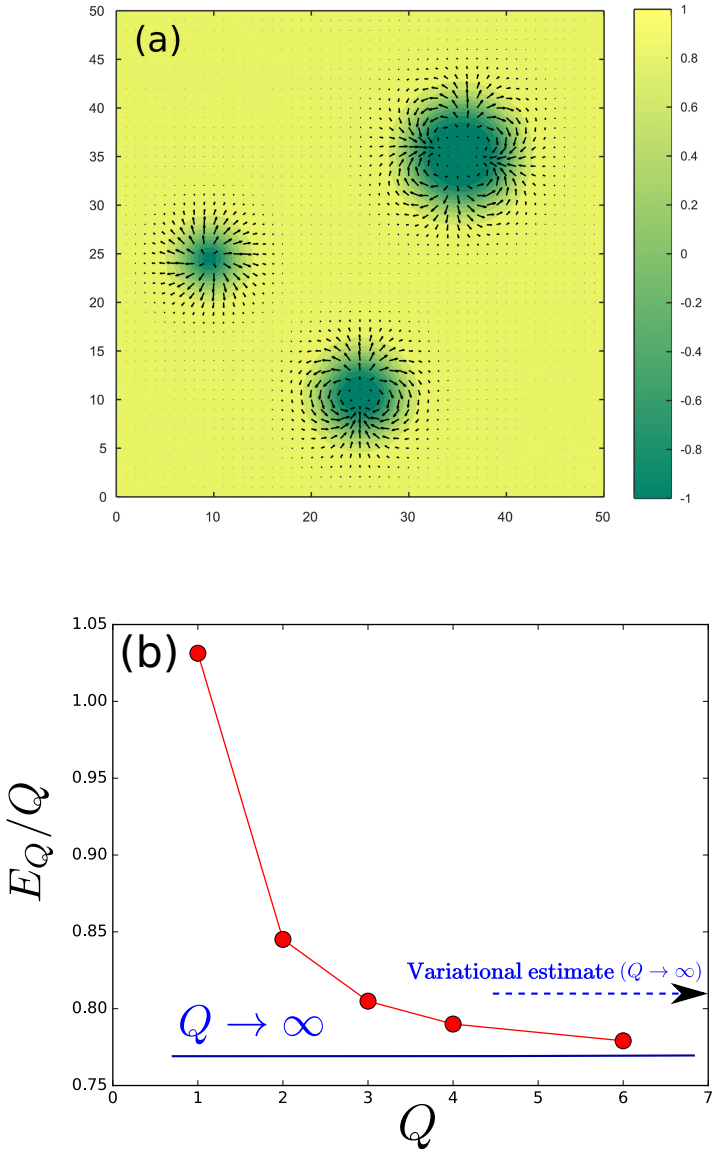

Figure 5.9: (a) Skyrmions with topological numbers $Q = 1, 2, 3$ in a frustrated magnet on the square lattice. (b) Energy of a skyrmion per topological charge E_Q/Q. Formation of multi-Q skyrmions is energetically favourable, because E_Q/Q decays with Q. Parameters J_2, J_3 and K are the same as in Fig. (5.8).

This "mass defect" drives the fusion of skyrmions, which increases the magnitude of the skyrmion magnetic moment, $M_z = \sum_i (S_i^z - 1) < 0$, counted from the positive magnetic moment of the FM state: for Q elementary skyrmions $M_z \propto -Q$, whereas for the ring with topological charge Q, $M_z \propto -Q^2$. A magnetic field applied in the positive z direction would lead to fission of multi-Q skyrmions into skyrmions with

smaller topological charges.

An example of a stable giant skyrmion with $Q = 6$ is presented in Fig. 5.10(a,c). The topological density of such a skyrmion is mainly concentrated at the perimeter of the skyrmion (see Fig. 5.10(c)), since the spins in the core of the skyrmions are uniformly polarized along the z-direction. Similarly the energy of the skyrmion is also localized at the perimeter of the skyrmion, hence the name "skyrmion rings"

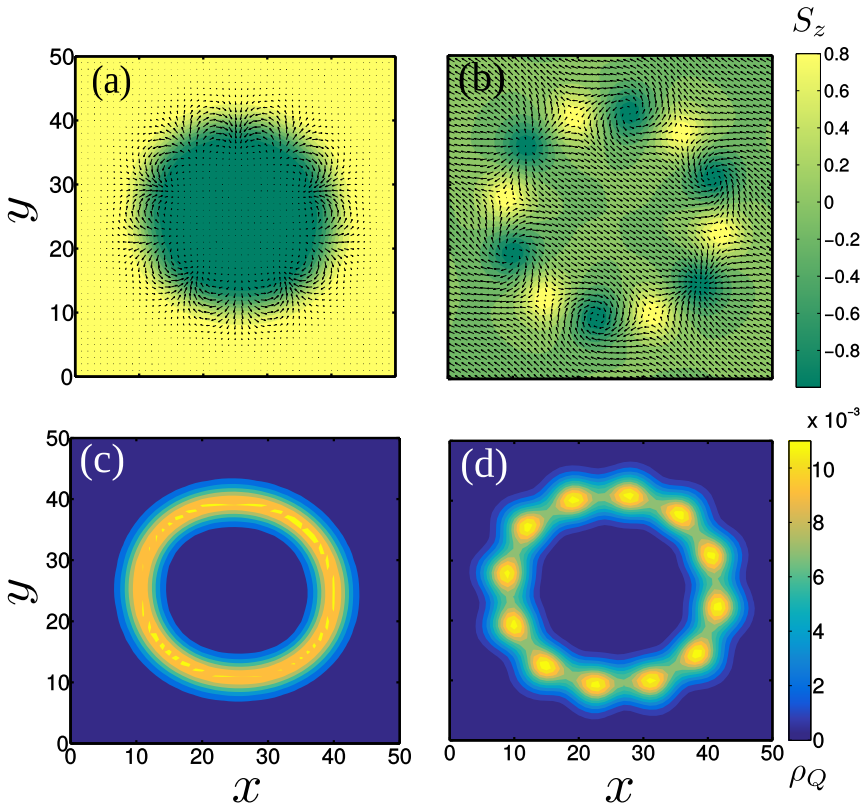

Figure 5.10: (a,c) A skyrmion ring with $Q = 6$ in the frustrated magnet with an easy axis anisotropy ($K = 0.01$). (b,d) A meron ring with the net topological charge $Q = 6$ (easy plane anisotropy, $K = -0.01$). Panels (a,b) show spin configuration, panels (c, d) represent the topological charge density $\rho_Q(x, y)$. Parameters of the simulations are $J_2 = 0.2$, $\rho = 3 \cdot 10^{-3}$.

The energy of a skyrmion ring can be evaluated using a variational approach, approximating the large skyrmion as a "domain wall" bent into a closed loop, which separates a FM state with $S_z = -1$ (inside of the skyrmion core, $r < R$) from the FM state with spin projection $S_z = 1$ (outside of the skyrmion core, $r > R$). Let us introduce a local coordinate system with the x-axis perpendicular to the domain

wall and the y-axis parallel to the domain wall. Substituting a variational ansatz $\cos\theta(x) = -\tanh(\varkappa x)$ ($\varkappa$ is the width of the domain wall) and $\phi(y) = qy$ (q is the wave vector describing rotation of $S_{x,y}$ spin projections along the domain wall boundary) into Eq.(5.2), we obtain

$$E_Q = \frac{L_s}{\varkappa}\left[\rho\left(q^2+\varkappa^2\right) + b_1\left(q^4+\varkappa^4\right) + \frac{b_2}{3}q^2\varkappa^2 + K\right], \tag{5.12}$$

where L_s is the perimeter of the skyrmion ring. Due to the periodicity condition the angle ϕ undergoes an integer number of rotations after following a closed loop on the skyrmion boundary $qL_s = 2\pi Q$. Minimization of the domain wall energy with respect to q and κ gives the energy per skyrmion for $|Q| \gg 1$:

$$E_Q/|Q| = 4\pi\left(\rho + \sqrt{K\left(2b_1 + \frac{1}{3}b_2\right)}\right). \tag{5.13}$$

Let us compare $E_Q/|Q|$ in Eq. (5.13) with the energy E_{sk} of a $|Q| = 1$ skyrmion, in Eq. (5.5). After substitution of the numerical values of the dimensionless integrals I_ρ, I_{b1}, I_{an}, I_K (Appendix 5.7.3) one can see that $E_Q/|Q| < E_{sk}$; this agrees with Fig. 5.9b and which explains why isolated skyrmions aggregate into the ring.

Let us remind that multi-skyrmion solutions for arbitrary Q exist in the usual $O(3)$ NLσ model. However, the binding energy of the multi-Q BP skyrmions is zero, since in this case $E_Q = 4\pi\rho_s|Q|$. Such skyrmions are not stable with respect to a decay on skyrmions with smaller Q, in the contrast with the multi-Q skyrmions in frustrated magnets.

Similar to multi-skyrmion rings there are also possible multi-meron configurations with a large topological charge. Meron pairs can form multi-meron bound states, in Fig. 5.10 (c,d) we show bound states of twelve merons with the total topological charge $Q = 6$.

As we have shown in the present Section, the attraction between skyrmions in frustrated magnets makes possible an existence of new exotic topological objects - skyrmion/meron rings. This unique feature of frustrated magnets tunes them into a potential platform for studying physics of skyrmions with large topological charges.

5.6 Discussion and conclusions

In the present Chapter we have studied skyrmions, meron pairs and skyrmion rings in frustrated magnets with an easy axis/easy plane anisotropy. Skyrmions and meron pairs can exist in these materials as excitations above a FM ground state. The balance between frustration and spin anisotropy stabilises the isolated topological defects even in the absence of an external magnetic field.

As a specific model we considered a $J_1 - J_2 - J_3$ Heisenberg model on the square lattice. However, in our analytical/variational analysis we used a continuum model (5.2); this allows most of our qualitative results to be generic and not specific for a particular choice of a lattice model of a frustrated magnet.

We found conditions for stability of the skyrmions/meron pairs and presented a stability phase diagram. We show that isolated skyrmions in frustrated magnets possess unusual properties: (i) the skyrmions attract each other and form skyrmions with a large topological charge (skyrmion rings). The energy and topological charge of a skyrmion ring is concentrated on its boundary. (ii) We showed that an elementary skyrmion with a unit topological charge becomes fractionalized in the presence of an easy plane anisotropy and exist as a bound state of two spatially separated merons with a topological charge 1/2 per meron. We demonstrated that the distance between the merons increases while approaching a phase transition to a spiral state and we showed that at critical line only finite amount of energy is needed to dissociate a meron pair allowing merons to become deconfined.

A very important task for future experimental work is to find a frustrated compound hosting skyrmions. One of the possible candidates is a wide class of vanadates (e.g. $VOMoO_4$ and $PbVO_3$) that correspond to $J_1 - J_2$ model with antiferromagnetic both J_1 and J_2. Another promising candidate is $(Pt_{1-x}Ir_x)Fe$ bilayer system on Pd (111) substrate [207], that has both Dzyaloshinsky-Morya and frustration Heizenberg exchange interactions on the interface of the bilayer. Meron pairs and meron rings can exist in the collinear phase of the easy-plane triangular antiferromagnet $NiBr_2$.[211] Search for novel frustrated compounds can open a new avenue for skyrmion studies.

5.7 Appendix

5.7.1 Phase diagram for the $J_1 - J_2 - J_3 - K$ model of a frustrated magnet on the square lattice

In the present section we analyse the phase diagram for a classical Heisenberg $J_1 - J_2 - J_3 - K$ ferromagnet. The phase diagram in the case of easy-plane anisotropy ($K < 0$) is identical to the phase diagram for $J_1 - J_2 - J_3$ Heisenberg model at $K = 0$. On the other hand, an easy axis anisotropy ($K > 0$) changes the phase diagram and impacts the boundary line separating FM state from spiral and CAF states. There are three phase boundaries we need to consider: (i) FM - 1D spiral, (ii) FM - 2D spiral, (iii) FM - CAF.

(i) FM-1D spiral

In this section we consider the phase boundary between FM and $(q, 0)/(0, q)$ spiral. To be specific we choose the wave vector of 1D spiral parallel to x-axis. One-dimensional spiral state can be parametrized in form

$$n_z(x) = \cos\theta(x), \quad n_x(x) = \sin\theta(x). \tag{5.14}$$

Substituting (5.14) in (5.2) we obtain energy of the spiral state

$$E[\theta] = \frac{L_y}{2}\int_{-\infty}^{\infty} dx \left[\rho(\theta')^2 + b_1\left\{(\theta'')^2 + (\theta')^4\right\} + K\sin^2\theta\right]. \tag{5.15}$$

Here L_y is the length of the domain wall in y-direction. The phase transition from FM to the spiral state is energetically favourable when the energy of the domain walls becomes negative. Proliferation of domain walls indicates a transition to a 1D spiral state, the normal to the domain wall is parallel to the x-axis. We are using the following ansatz for the domain wall solution

$$\cos\theta = \tanh(x/l), \tag{5.16}$$

where l is a variational parameter. Substituting the ansatz in (5.15) and calculating corresponding integrals over x, we obtain

$$E[l] = L_y \left[\frac{\rho}{l} + \frac{b_1}{l^3} + Kl \right]. \tag{5.17}$$

Minimizing energy (5.17) as a function of the parameter l, we obtain optimal width $l_0^2 = (\rho + \sqrt{\rho^2 + 12Kb_1})/2K$ and the energy of domain wall $E[l_0] = \frac{2L_y}{l_0^3}(\rho l_0^2 + 2b_1)$. Condition for the phase transition is $E[l_0] = 0$, that gives

$$\rho^2 = 2b_1 K \quad \Rightarrow \quad J_2 = 1/2 - 2J_3 + K/24 + \sqrt{(K/24)^2 + J_3 K/2}. \tag{5.18}$$

(ii) FM-2D spiral

In the present section we analyse the phase boundary between FM and $(q, \pm q)$ spiral phase. The domain walls separating $S_z = \pm 1$ regions will orient along one of the diagonals of the square lattice. Let us choose the wave vector of 2D spiral along $(1, 1)$ direction. Such two-dimensional spiral can be parametrized in the form

$$n_z(x, y) = \cos\theta(\xi), \quad n_x(x, y) = \sin\theta(\xi), \tag{5.19}$$

where $\xi = x + y$. Substituting parametrization (5.19) in (5.2), we obtain

$$E[\theta] = L_\perp \int_{-\infty}^{\infty} d\xi \left[\rho(\theta_\xi)^2 + (b_1 + b_2/2) \left\{ (\theta_{\xi\xi})^2 + (\theta_\xi)^4 \right\} + K \sin^2\theta/2 \right]. \tag{5.20}$$

Here $L_\perp$ is the length of the domain wall. Let us note that Eq. (5.20) takes the same form as Eq. (5.15) after the following substitution

$$b_1 \to b_1 + b_2/2, \quad K \to K/2. \tag{5.21}$$

That gives equation for the phase boundary

$$\rho^2 = (b_1 + b_2/2)K \quad \Rightarrow \quad 2J_2 + 4J_3 = 1 + K/6 + \sqrt{(K/6)^2 + K/4}. \tag{5.22}$$

Therefore, according to Eqs. (5.18), (5.22) the FM domain on the $J_2 - J_3$ phase diagram becomes extended in the presence of easy axis anisotropy (for $K \ll 1$ the value of spin stiffness at the FM-spiral boundary line $\rho = \mathcal{O}(\sqrt{K}) < 0$).

(iii) FM-CAF

The K-term does not affect the difference in energy between FM and CAF phases. Therefore, the point $(J_2, J_3) = (1/2, 0)$ separating FM and CAF phases remains unchanged for any K.

5.7.2 Details of the numerical procedure

We have performed a minimization of classical energy (5.1) using the Landau-Lifshitz-Gilbert (LLG) equation with a damping term. The LLG is solved using forth-order Runge-Kutta method on the 50×50 square grid with the periodic boundary conditions. The spin configuration is evolved until it converges to a time-independent solution. We use the value of damping coefficient $\eta = 1$, however the final result does not depend on the choice of η.

In order to obtain skyrmion solutions (Fig. 5.3) we use a uniform FM state ($S_z = 1$) with a single spin flipped ($S_z = -1$) in the center of the lattice. The constraint $S_z = -1$ is imposed in the process of solving the LLG equation.

To find the interaction potential of meron-meron (Fig. 5.7b) we impose constraints $S_z = -1$ and $S_z = 1$ in the centers of the merons. For the calculation of the skyrmion-skyrmion potential (Fig. 5.8) we impose constraint $S_z = -1$ in the centers of the skyrmions.

5.7.3 Variational description of fundamental skyrmions

In the present section we discuss a variational analysis of $Q = 1$ skyrmions in the case of easy axis anisotropy. Rewriting Eq. (5.2) in the form

$$E[S_\mu] = \frac{1}{2} \int d^2r \left[\rho(\partial_i S_\mu)^2 + b_1(\partial^2 S_\mu)^2 + (b_2 - 2b_1)\partial_x^2 S_\mu \partial_y^2 S_\mu + K(1 - S_z^2) \right], \quad (5.23)$$

we explicitly separate isotropic contribution to the elastic energy $\propto b_1(\partial^2 S_\mu)^2$ and anisotropic contribution $(b_2 - 2b_1)\partial_x^2 S_\mu \partial_y^2 S_\mu$. Substituting (5.3) the exponential ansatz $\theta(r) = \pi e^{-r/R}$ into Eq. (5.23) we obtain

$$E[S_\mu] = \mathcal{E}_\rho + \mathcal{E}_{b1} + \mathcal{E}_{an} + \mathcal{E}_K = \rho I_\rho + \frac{b_1}{R^2} I_{b1} + \frac{b_2 - 2b_1}{R^2} I_{an} + K R^2 I_K, \tag{5.24}$$

where the energy terms in (5.24) originate from the corresponding terms in (5.23). Dimensionless variational integrals I_ρ, I_{b1}, I_{an}, I_K can be calculated numerically

$$\begin{aligned}
I_K &= \frac{\pi}{2} \int_0^\infty dx x \sin^2\theta(x) \approx 3.96, \\
I_\rho &= \pi \int_0^\infty dx x \left[\frac{1}{x^2} \sin^2(\theta(x)) + (\theta'(x))^2 \right] \approx 13.17, \\
I_{b1} &= \pi \int_0^\infty dx x \left[\left(\Delta_x \sin\theta(x) - \frac{\sin\theta(x)}{x^2} \right)^2 + (\Delta_x \cos\theta(x))^2 \right] \approx 73.87, \\
I_{an} &= \frac{\pi}{8} \int_0^\infty \frac{dx}{x^3} \left[-3\sin^2\theta(x) + +x^2(\theta'(x))^2(2 - 5\cos 2\theta(x)) + x^4(\theta'(x))^4 + \right. \\
&\left. 3x^2(\sin 2\theta(x) - 2x\theta'(x))\theta''(x) + 3x\theta'(x)\sin 2\theta(x) + x^4(\theta''(x))^2 \right] \approx 9.23.
\end{aligned} \tag{5.25}$$

Here $\theta(x) = \pi e^{-x}$ and $\Delta_x = \partial_{xx} + \frac{1}{x}\partial_x$ is the 2D radial Laplacian.

The analytically tractable ansatz $\theta_0(r) = \pi(1 - r/R)$ at $r < R$ and $\theta_0(r) = 0$ at $r > R$ is sometimes used in literature for a variational description of skyrmions, see e.g. [78]. However this variational ansatz can not be applied to Eq. (5.2), because the first derivative of $\theta_0(r)$ has a discontinuity at $r = R$. This would result in a delta-function term in the second order derivatives in Eq. (5.2), therefore $(\theta'')^2$ will cause a divergence of integrals I_{b1} and I_{an}.

5.7.4 Variational description of meron pairs

A variational description for meron pairs with isotropic topological density profile ("round" meron pars, as in Fig. 5.6b,e) can be developed by analogy with Sec. 5.3. A variational skyrmion solution with a unit topological number can be constructed by performing a global rotation of S_μ parametrized as (5.3) in yz plane on the angle $\pi/2$: $(S^x, S^y, S^z) \to (S^x, -S^z, S^y)$. The simplest isotropic parametrisation for such meron pair reads $S_\mu = (\sin\theta(r)\cos\phi, -\cos\theta(r)\sin(\phi + \chi), \sin\theta(r)\sin(\phi + \chi))$

with the exponential variational function $\theta(r)$. Note, that the energy density terms in (5.2) excluding the spin anisotropy term $\propto K$ are invariant with respect to a global rotation in the spin space. This results in the same values of the variational integrals I_a, I_{b1} and I_{an} as in the case $K > 0$. The spin anisotropy term in (5.4) reads $-K/2 \int d^2r S_z^2(r) = -\pi K/2 \int dr r \sin^2\theta(r) = |K| I_K R^2$ (see Eqs. (5.24) and (5.25) in Suppl. Mater.). Therefore, the variational energy of the meron pair reads

$$E_{sk} = \rho I_\rho + 2\sqrt{b_1 I_{b1} + (b_2 - 2b_1) I_{an}} \sqrt{|K| I_K}. \tag{5.26}$$

The characteristic size of a meron pair is $R_0 = \left(\frac{b_1 I_{b1} + (b_2 - 2b_1) I_{an}}{|K| I_K}\right)^{1/4}$. The variational results for the meron pair energy and the radius coincide with the corresponding skyrmion energy and radius in Section 5.3 after the substitution $K \to |K|$.

5.7.5 Multi-Q skyrmions

As it shown in the main text, Section 5.5, skyrmion rings can be treated as domain walls enclosed in a loop. The energy of the domain wall is given by

$$E_Q = \frac{\pi Q}{q} \int dx \left[\rho\left(\theta'^2 + q^2 \sin^2\theta\right) + b_1\left(\theta''^2 + \theta'^4 + q^4 \sin^2\theta\right) + b_2 q^2 \cos^2\theta \theta'^2 + K \sin^2\theta\right], \tag{5.27}$$

Substituting the variational Ansatz,

$$\cos\theta = -\tanh(\kappa x), \tag{5.28}$$

where κ is the inverse width of the domain wall, into Eq.(5.27), we obtain

$$E_Q = \frac{2\pi Q}{q\kappa}\left[\rho\left(q^2 + \kappa^2\right) + b_1\left(q^4 + \kappa^4\right) + \frac{b_2}{3} q^2 \kappa^2 + K\right]. \tag{5.29}$$

Minimization of the domain wall energy (5.29) with respect to q and κ at fixed Q gives

$$\kappa = |q| = \left[\frac{K}{2b_1 + \frac{1}{3} b_2}\right]^{\frac{1}{4}}. \tag{5.30}$$

According to Eq.(5.30) the length per skyrmion is $l_s = \frac{2\pi}{q}$ is comparable to the

domain wall width $1/\kappa$. The energy per skyrmion reads

$$E_Q/|Q| = 4\pi\left(\rho + \sqrt{K\left(2b_1 + \frac{1}{3}b_2\right)}\right) \tag{5.31}$$

Importantly, $E_Q/|Q|$ is lower than the energy of an isolated skyrmion E_{sk} with $|Q| = 1$, Eq. (5.24). This explains why isolated skyrmions aggregate into the ring. The radius of the ring, R, is given by

$$2\pi R = |Q| l_{\mathrm{s}} \tag{5.32}$$

and the total spin projected carried by the ring skyrmion is

$$S_Q^z = -2\pi R^2 = -\frac{l_{\mathrm{s}}^2 Q^2}{2\pi}. \tag{5.33}$$

In Eq.(5.31) the first term is the Belavin-Polyakov lower bound on the skyrmion energy obtained in the conformal continuum model. The second term results from the interplay between the q^4 term in expansion of the exchange energy and the magnetic anisotropy, which also determines the width of the domain wall.

We would like to stress, that without longer range exchange interactions, skyrmions in the ferromagnetic Heisenberg lattice model are unstable. Thus the skyrmion domain wall is stable for $2b_1 + \frac{1}{3}b_2 > 0$ and the ferromagnetic state is stable for $\rho > 0$, which gives

$$2J_2 + 4J_3 < J_1 < 4J_2 + 16J_3. \tag{5.34}$$

In addition, validity of the continuum model requires $q \ll 1$ or

$$\left[\frac{6K}{-J_1 + 4J_2 + 16J_3}\right]^{\frac{1}{4}} \ll 1. \tag{5.35}$$

List of Figures

Bibliography

[1] S. Sachdev (1999) Quantum Phase Transitions (Cambridge: Cambridge University Press)

[2] E.M. Lifshitz and L.P. Pitaevskii, Staistical Physics, Part II (Butterworth-Heinmann, 1995)

[3] M. Vojta, Rep. Prog. Phys. **66**, 2069 (2003).

[4] N. D. Mermin, H. Wagner, Phys. Rev. Lett., **17**, 1133 (1966).

[5] J.Zinn-Justin, Quantum field theory and critical phenomena (3rd ed.), Oxford University Press, (1996).

[6] K. G. Wilson and J. Kogut, Phys. Rep. 12, **75** (1974).

[7] J. Goldstone, A. Salam, and S. Weinberg, Broken symmetries, Phys. Rev. **127**, 965 (1962).

[8] K. G. Wilson, Phys. Rev. B **4** 3174, (1971).

[9] M. E. Peskin, D. V. Schroeder, An Introduction to Quantum Field Theory, Addison-Wesley Publishing Company (1995).

[10] K. G. Wilson and M. E. Fisher, Phys. Rev. Lett. **28**, 240 (1972).

[11] P. A. Lee, N. Nagaosa, and X.-G. Wen, Rev. Mod. Phys. **78**, 17 (2006).

[12] M. R. Norman and C. Pepin, Rep. Prog. Phys. **66**, 1547 (2003).

[13] B. Keimer, S. A. Kivelson, M. R. Norman, S. Uchida and J. Zaanen, Nature **518**, 179–186 (2015).

[14] T. Shibauchi, A. Carrington, Y. Matsuda, Annu. Rev. Condens. Matter Phys. 5, **113** (2014).

[15] H. v. Löhneysen, A. Rosch, M. Vojta and P. Wölfle, Rev. Mod. Phys. **79**, 1015 (2007).

[16] P. Coleman, C. Pepin, Q. Si, R. Ramazashvili, J. Phys. Condens. Matter **13**, R723 (2001).

[17] E. Slooten, T. Naka, A. Gasparini, Y. K. Huang, and A. de Visser, Phys. Rev. Lett. **103**, 097003 (2009).

[18] G. Giovannetti, S. Kumar, J. van den Brink, Phys. B. **403**, 3653 (2008).

[19] R. A. Borzi , S. A. Grigera, J. Farrell, R. S. Perry, S. J. S. Lister *et al.*, Science **315** 214 (2007).

[20] S. L. Sondhi, S. M. Girvin, J. P. Carini and D. Shahar Rev. Mod. Phys. **69**, 315 (1997).

[21] S. V. Kravchenko, Whitney E. Mason, G. E. Bowker, J. E. Furneaux, V. M. Pudalov, and M. D'Iorio, Phys. Rev. B 51, 7038 (1995).

[22] Ch. Rüegg, N. Cavadini, A. Furrer, H.-U. Güdel, K. Krämer, H. Mutka, A. Wildes, K. Habicht, and P. Vorderwisch, Nature **423**, 62 (2003).

[23] Ch. Rüegg, B. Normand, M. Matsumoto, A. Furrer, D. F. McMorrow, K. W. Krämer, H.-U. Güdel, S. N. Gvasaliya, H. Mutka, and M. Boehm, Phys. Rev. Lett. **100**, 205701 (2008).

[24] K. Goto, M. Fujisawa, T. Ono, H. Tanaka, and Y. Uwatoko, J. Phys. Soc. Jpn. **73**, 3254 (2004).

[25] N. Kurita and H. Tanaka, Phys. Rev. B **94**, 104409 (2016).

[26] Y. Kulik, and O. P. Sushkov, Phys. Rev. B **84**, 134418 (2011).

[27] H.D. Scammell and O. P. Sushkov, Phys. Rev. B **92**, 220401(R) (2015).

[28] J. G. Bednorz and K. A. Müller, Z. Phys. B **64**, 189 (1986).

[29] M.R. Norman *et al*, Nature **392**, 157 (1998).

[30] A. Damascelli, Z. Hussain, and Z.-X. Shen, Rev. Mod. Phys. **75**, 473-541 (2003).

[31] C. Stock, W. J. L. Buyers, Z. Yamani, Z. Tun, R. J. Birgeneau, R. Liang, D. Bonn, and W. N. Hardy, Phys. Rev. B **77**, 104513 (2008).

[32] V. Hinkov, D. Haug, B. Fauqué, P. Bourges, Y. Sidis, A. Ivanov, C. Bernhard, C. T. Lin, and B. Keimer, Science **319**, 597 (2008).

[33] D. Haug, V. Hinkov, Y. Sidis, P. Bourges, N. B. Christensen, A. Ivanov, T. Keller, C. T. Lin and B. Keimer, New J. Phys., **12**, 105006 (2010).

[34] A. I. Milstein and O. P. Sushkov, Phys. Rev. B **78**, 014501 (2008).

[35] G. Ghiringhelli *et al.*, Science **337**, 821–825 (2012).

[36] A. J. Achkar *et al.* Phys. Rev. Lett. **109**, 167001 (2012).

[37] E. Blackburn *et al.*, Phys. Rev. Lett. **110**, 137004 (2013).

[38] R. Comin *et al.*, Science **343**, 390 (2014).

[39] J. Chang *et al.*, Nat. Phys. **8**, 871–876 (2012).

[40] J. Chang *et al.*, Nat. Comm. **7**, 11494 (2016).

[41] T. Wu *et al.*, Nature **477**, 191–194 (2011).

[42] T. Wu *et al.*, Nat. Commun. **4**, 2113 (2013).

[43] T. Wu *et al.*, Nat. Commun. **6**, 6438 (2015).

[44] K. Fujita *et al.*, Science **344**, 612 (2014).

[45] M. H. Hamidan *et al.*, Nature Physics **8**, 871 (2012).

[46] W. Tabis *et al.*, Nat. Commun. **5**, 5875 (2014).

[47] J. M. Tranquada, B. J. Sternlieb, J. D. Axe, Y. Nakamura, S. Uchida, Nature **375**, 561 (1995).

[48] P. Abbamonte *et al.*, Nat. Phys. **1**, 155 (2005).

[49] H. Alloul, J. Bobroff, M. Gabay, and P. J. Hirschfeld, Rev. Mod. Phys. **81**, 45 (2009).

[50] M. Takigawa, N. Motoyama, H. Eisaki, and S. Uchida, Phys. Rev. B **55**, 14129 (1997).

[51] J. Bobroff, N. Laflorencie, L. K. Alexander, A. V. Mahajan, B. Koteswararao, and P. Mendels, Phys. Rev. Lett. **103**, 047201 (2009).

[52] A. V. Mahajan, H. Alloul, G. Collin, and J. F. Marucco Phys. Rev. Lett. 72, 3100 (1994).

[53] J. Bobroff, W. A. MacFarlane, H. Alloul, P. Mendels, N. Blanchard, G. Collin, and J. F. Marucco, Phys. Rev. Lett. 83, 4381 (1999).

[54] M.-H. Julien, T. Feher, M. Horvatic, C. Berthier, O. N. Bakharev, P. Segransan, G. Collin, and J.-F. Marucco, Phys. Rev. Lett.**84**, 3422 (2000).

[55] S. Ouazi, J. Bobroff, H. Alloul, M. Le Tacon, N. Blanchard, G. Collin, M. H. Julien, M. Horvatic, and C. Berthier, Phys. Rev. Lett. **96**, 127005 (2006).

[56] H. Imamura, T. Ono, K. Goto, and H. Tanaka, Phys. Rev. B **74**, 064423 (2006).

[57] T. Suzuki, I. Watanabe, F. Yamada, Y. Ishii, K. Ohishi, Risdiana, T. Goto, and H. Tanaka, Phys. Rev. B **80**, 064407 (2009).

[58] T. Suzuki, M. Yamada, Y. Ishii, I. Watanabe, T. Goto, and H. Tanaka, K. Kubo, Phys. Rev. B **83**, 174436 (2011).

[59] G. B. Martins, M. Laukamp, J. Riera, and E. Dagotto, Phys. Rev. Lett. 78, 3563 (1997).

[60] S. Eggert, O. F. Syljuasen, F. Anfuso, and M. Andres, ibid. 99, 097204 (2007).

[61] A. Lüsher and O. Sushkov, PRB **71**, 064414 (2005).

[62] R. K. Kaul, R. G. Melko, M. A. Metlitski, and S. Sachdev, Phys. Rev. Lett. 101, 187206 (2008).

[63] A. Polkovnikov, S. Sachdev, and M. Vojta, Phys. Rev. Lett. **86**, 296 (2001).

[64] M. Vojta, C. Buragohain, and S. Sachdev, Phys. Rev. B **61**, 15152 (2000).

[65] O. P. Sushkov, Phys. Rev. B **62**, 12135 (2000).

[66] K. H. Höglund, A. W. Sandvik, and S. Sachdev, Phys. Rev. Lett. **98** 087203 (2007).

[67] T. Roscilde and S. Haas, Phys. Rev. Lett. **95**, 207206 (2005).

[68] Rong Yu, Omid Nohadani, Stephan Haas, and Tommaso Roscilde Phys. Rev. B **82**, 134437 (2010).

[69] R. Yu *et al.*, Nature **489**, 379 (2012).

[70] N. Ma, A. W. Sandvik, and D.-X. Yao, Phys. Rev. B **90**, 104425 (2015).

[71] J. Kondo, Progress of Theoretical Physics **32**, 37 (1964).

[72] T. H. R. Skyrme, Nucl. Phys. **31** 556 (1962).

[73] N. Nagaosa and Y. Tokura, Physica Scripta **2012** 146 (2012).

[74] N. Nagaosa, Y. Tokura, Nat. Nanotechnol. **8**, 899 (2013).

[75] S. E. Barrett, G. Dabbagh, L. N. Pfeiffer, K. W. West, and R. Tycko, Phys. Rev. Lett. **74**, 5112 (1995).

[76] T. Ho, Spinor Bose Condensates in Optical Traps, Phys. Rev. Lett. **81**, 742 (1998).

[77] J. Fukuda and S. Zumer, Nature Communications **2** 246 (2011).

[78] N. Bogdanov and D. A. Yablonskii, Sov. Phys. JETP **68**, 101 (1989).

[79] U. K. Roβler, A. N. Bogdanov, and C. Pfleiderer, Nature **442**, 797 (2006).

[80] S. Muhlbauer, Science **323**, 915 (2009).

[81] R. Rajamaran: Soltons and Instantons (Noth Holland, 1987).

[82] A.M. Kosevich, B.A. Ivanov and A.S. Kovalev, Physics Reports **1**94 117-238 (1990).

[83] A. A. Belavin and A. M. Polyakov, JETP Lett. **22**, 245 (1975).

[84] X. Z. Yu *et al.*, Nature **465**, 901 (2010).

[85] W. Munzer *et al.*, Phys. Rev. B **81**, 041203 (2010).

[86] X. Z. Yu, N. Kanazawa, W. Z. Zhang, T. Nagai, T. Hara, K. Kimoto, Y. Matsui, Y. Onose, and Y. Tokura, Nature Materials **10**, 106 (2011).

[87] F. Jonietz *et al.*, Science 330, 1648 (2010).

[88] X. Z. Yu, N. Kanazawa, W. Z. Zhang, T. Nagai, T. Hara, K. Kimoto, Y. Matsui, Y. Onose, and Y. Tokura, Nat. Commun. **3**, 988 (2012).

[89] S. Seki, X.Z Yu, S. Ishiwata, and Y. Tokura, Science **330**, 1648 (2012).

[90] S. Woo *et al.*, Nature Materials **15**, 501 (2016).

[91] C. Moreau-Luchaire *et al.*, Nature Nanotechnology **11**, 44 (2016).

[92] Y. Tokunaga *et al.*, Nature Commun. **6**, 7238 (2015).

[93] R. Wiesendanger, Nature Review Materials **1**, 16044 (2016).

[94] A. Fert, P. M. Levy, Phys. Rev. Lett. **44**, 1538 (1980).

[95] S. Heinze *et al.*, Nature Physics **7** 713 (2011).

[96] U. K. Roβler, A. A. Leonov and A. N. Bogdanov, J. Phys. Conf. Ser. **303**, 012105 (2011).

[97] A. O. Leonov, T. L. Monchesky, N. Romming, A. Kubetzka, A. N. Bogdanov and R. Wiesendanger, New Journal of Physics **1**8, 065003 (2016).

[98] N. Romming, C. Hanneken, M. Mentzel, J. E. Bickel, B. Wolter, K. von Bergmann, A. Kubetzka, and R. Wiesendanger, Science **114**, 177203 (2013).

[99] N. Romming, A. Kubetzka, C. Hanneken, K. von Bergmann and R. Wiesendanger, Phys. Rev. Lett. **114**, 177203 (2015).

[100] L. Kong and J. Zhang, Phys. Rev. Lett **111**, 067203 (2013).

[101] M. Lee, W. Kang, Y. Onose, Y. Tokura and N.P. Ong, Phys. Rev. Lett. **102**, 186601 (2009).

[102] A. Neubauer *et al.*, Phys. Rev. Lett. **102**, 186602 (2009).

[103] J. Zang, M. Mostovoy, J. H. Han, and N. Nagaosa, Phys. Rev. Lett. **107**, 136804 (2011).

[104] W. Jiang *et al.*, Nature Physics (2016).

[105] F. Jonietz *et al.* Science **330**, 1648–1651 (2010).

[106] A. Fert, V. Cros and J. Sampaio, Nat. Nanotechnol. **8**, 152 (2013).

[107] J. Iwasaki, M. Mochizuki and N. Nagaosa, Nat. Nanotechnol. **8**, 742 (2013).

[108] X. Zhang, M. Ezawa and Y. Zhou, Scientific Reports **5**, 9400 (2015).

[109] Y. Zhou and M. Ezawa, Nat. Nanotechnol. **5**, 4652 (2014).

[110] E. M. R. Tomasello, R. Zivieri, L. Torres, M. Carpentieri and G. Finocchio, Sci. Rep. **4**, 6784 (2014).

[111] T. Okubo, S. Chung, H. Kawamura, Phys. Rev. Lett. **108**, 017206 (2012).

[112] A. O. Leonov and M. Mostovoy, Nature Comm. **6**, 8725 (2015).

[113] S. Z. Lin and S. Hayami, Phys. Rev. B **93**, 064430 (2016).

[114] I. Zahed and G.E. Brown, Phys. Rept. **142**, 1 (1986).

[115] R.A. Battye, N.S. Manton and P.M. Sutcliffe in *The Multifaceted Skyrmions* (World Scientific, Singapore, 2016) ed. M. Rho and I. Zahed.

[116] I.R. Klebanov, Nucl. Phys. B **262**, 133 (1985).

[117] A.S. Goldhaber and N.S. Manton, Phys. Lett. B **198**, 231 (1987).

[118] M. Kugler and S. Shtrikman, Phys. Rev. D **40**, 3421 (1989).

[119] A. Actor, Reviews of Modern Physics, **51** (3) 461 (1979).

[120] V. de Alfaro, S. Fubini and G. Furlan, Phys. Lett. 65B (1977) 1631.

[121] C. Callan, R. Dashen and D. Gross, Phys. Lett. **6**, 6B (1977).

[122] D. Gross, Nucl. Phys. B **132**, 439 (1978).

[123] L. Brey, H. A. Fertig, R. Cote, and A. H. MacDonald, Phys. Scr. 1996, **154** (1996).

[124] R. Cote, W. Luo, B. Petrov, Y. Barlas, and A. H. MacDonald, Phys. Rev. B **82**, 245307 (2010).

[125] M. Ezawa, Phys. Rev. B **83**, 100408(R) (2011).

[126] R. M. Wilson, B. M. Anderson, and C. W. Clark, Phys. Rev. Lett. **111**, 185303 (2013).

[127] S.Z. Lin, A. Saxena and C. Batista, Phys. Rev. B **91**, 224407 (2015).

[128] C. Phatak, A. K. Petford-Long, and O. Heinonen Phys. Rev. Lett. **108**, 067205 (2012).

[129] S. Wintz *et al.*, Phys. Rev. Lett. 110, 177201 (2013).

[130] A. Tan, J. Li, A. Scholl, E. Arenholz, A. T. Young, Q. Li, C. Hwang, and Z. Q. Qiu Phys. Rev. B **94**, (2016).

[131] M. A. Hossain , J. D. F. Mottershead, D. Fournier, A. Bostwick, J. L. McChesney, E. Rotenberg, R. Liang, W. N. Hardy, G. A. Sawatzky, I. S. Elfimov, D. A. Bonn, and A. Damascelli, Nat. Phys. **4**, 527 (2008).

[132] R-H He *et al.*, New J. Phys. **13**, 013031 (2011).

[133] H.-B. Yang, J. D. Rameau, Z.-H. Pan, G. D. Gu, P. D. Johnson, H. Claus, D. G. Hinks, and T. E. Kidd, Phys. Rev. Lett. **107**, 047003 (2011).

[134] N. Doiron-Leyraud, C. Proust, D. LeBoeuf, J. Levallois, J. B. Bonnemaison, R. Liang, D. A. Bonn, W. N. Hardy, and L. Taillefer, Nature **447**, 565 (2007).

[135] B. Vignolle, A. Carrington, R. A. Cooper, M. M. J. French, A. P. Mackenzie, C. Jaudet, D. Vignolles, C. Proust and N. E. Hussey, Nature, **455**, 952 (2008).

[136] Z. Liu and E. Manousakis, Phys. Rev. B **45**, 2425 (1992).

[137] D. J. Scalapino, Phys. Rep. **250**, 329 (1995); P. Monthoux and D. Pines, Phys. Rev. B **47**, 6069 (1993); A. Abanov, A. V. Chubukov, and J. Schmalian, Adv. Phys. **52**, 119 (2003).

[138] M. Yu. Kuchiev and O. P. Sushkov, Physica C **218**, 197 (1993); V. V. Flambaum, M. Yu. Kuchiev, O. P. Sushkov, Physica C **227**, 267 (1994).

[139] Y. Wang and A. V. Chubukov, Phys. Rev. B **88**, 024516 (2013).

[140] P. Krotkov and A. V. Chubukov, Phys. Rev. Lett., **96**, 107002 (2006).

[141] E. G. Moon and S. Sachdev, Phys. Rev. B **80**, 035117 (2009).

[142] M. Holt, J. Oitmaa, W. Chen, and O. P. Sushkov, Phys. Rev. Lett. **109**, 037001 (2012); Phys. Rev. B **87**, 075109.

[143] H.B.C. Casimir, D. Polder , Phys. Rev. 73, 360 (1948).

[144] J. R. Schrieffer, X. G. Wen, and S. C. Zhang, Phys. Rev. Lett. **60**, 944 (1988).

[145] L. P. Pryadko, S. Kivelson, and D. W. Hone PRL **80**, 5651 (1998).

[146] A. Chodos, R. L. Jaffe, K. Johnson, and C. B. Thorn, Phys. Rev. B **10**, 8 (1974).

[147] G.E. Brown, M. Rho, Phys. Lett. B **82**, 177-180 (1979).

[148] A. W. Sandvik and D. J. Scalapino, Phys. Rev. Lett. **72**, 2777 (1994).

[149] A. W. Sandvik, A. V. Chubukov, and S. Sachdev, Phys. Rev. B **51**, 16483 (1995).

[150] Z. Weihong, Phys. Rev. B **55**, 12267 (1997).

[151] V. N. Kotov, O. Sushkov, ZhengWeihong , and J. Oitmaa, Phys. Rev. Lett. **80**, 5790 (1998).

[152] M. Vojta and K. W. Becker, Phys. Rev. B **60**, 15201 (1999).

[153] Y. Matsushita, M. P. Gelfand, and C. Ishii, J. Phys. Soc. Jpn. **68**, 247 (1999).

[154] D. K. Yu, Q. Gu, H. T. Wang, and J. L. Shen, Phys. Rev. B **59**, 111 (1999).

[155] C. Jurecka and W. Brenig, Phys. Rev. B **63**, 094409 (2001).

[156] R. Eder, Phys. Rev. B **57**, 12832 (1998).

[157] Y. Saito, A. Koga, and N. Kawakami, J. Phys. Soc. Jpn **72**, 1208 (2003).

[158] A. V. Chubukov, JETP Lett. **47**, 129 (1989); S. Sachdev and R. N. Bhatt, Phys. Rev. B **41**, 9323 (1990).

[159] I. E. Dzyaloshinsky, JETP **30**, 1152 (1956).

[160] C. Itzykson, J.-B. Zuber, Quantum Field Theory, McGraw-Hill International Book Co. (1980).

[161] S. Sachdev, M. Troyer and M. Vojta, Phys. Rev. Lett. **86**, 2617 (2001).

[162] S. Sachdev and B. Keimer, Phys. Today **64** (2), 29 (2011).

[163] H. Tanaka, K. Goto, M. Fujisawa, T. Ono, Y. Uwatoko, Physica (Amsterdam) **329–333B**, 697 (2003).

[164] A. Oosawa, M. Fujisawa, K. Kakurai, and H. Tanaka, Phys. Rev. B **67**, 184424 (2003).

[165] A. W. Sandvik, E. Dagotto, and D. J. Scalapino, Phys. Rev. B **56**, 11701 (1997).

[166] Y. Saito, A. Koga, and N. Kawakami, J. Phys. Soc. Jpn. **72**, 1208 (2003).

[167] V. Barzykin and I. Affleck, Phys. Rev. B **57**, 432 (1998).

[168] K. Ingersent and Q. Si, Phys. Rev. Lett. **89**, 076403 (2002).

[169] S. Florens, L. Fritz, and M. Vojta, Phys. Rev. Lett. **96**, 036601 (2006).

[170] S. I. Tomonaga, Prog. Theor. Phys. **5**, 544 (1950).

[171] J. M. Luttinger, J. Math. Phys. **4**, 1154 (1963).

[172] M. Haase, I. Terasaki, Y. Sasago, K. Uchinokura, and H. Obara, Phys. Rev. Lett. **71**, 4059 (1993).

[173] W. O. Putikka, R. L. Glenister, R. R. P. Singh, and H. Tsunetsugu, Phys. Rev. Lett. **73**, 170 (1994).

[174] Y. C. Chen, A. Moreo, F. Ortolani, E. Dagotto, and T. K. Lee, Phys. Rev. B **50**, 655 (1994).

[175] T. Tohyama, S. Maekawa, J. Phys. Soc. Jap. **65**, 1902 (1996).

[176] G B. Martins, R. Eder, and E. Dagotto, Phys. Rev. B **60**, R3716 (1999).

[177] M. Holt, J. Oitmaa, W. Chen, and O. P. Sushkov, Phys. Rev. B **87**, 075109 (2013).

[178] O. Nohadani, S. Wessel, and S. Haas, Phys. Rev. B **72**, 024440 (2005).

[179] S. Jin and A. Sandvik, Phys. Rev. B **85**, 020409(R) (2012).

[180] A. I. Milstein, O. P. Sushkov, Phys. Rev. B **84**, 195138 (2011).

[181] Y. A. Kharkov, O. P. Sushkov, to be published.

[182] S. A. Brazovskii and I. A. Luk'yanchuk, Zh. Eksp. Teor.Fiz. **96**, 2088 (1989) [Sov. Phys. JETP **69**, 1180 (1989)].

[183] R. R. Ramazashvili, Phys. Rev. Lett. **101**, 137202 (2008); Phys. Rev. B **79**, 184432 (2009).

[184] V. Yu. Irkhin, A. A. Katanin, and M. I. Katsnelson, Phys. Rev. B **60**, 14779 (1999).

[185] G. D. Mahan, Many-particle physics, Kluwer Academic/Plenum Publishers, New York, p. 218-247 (2000).

[186] D. LeBeouf *et al.*, Nat. Phys. **9**, 79–83 (2013).

[187] J. Xia *et al.*, Phys. Rev. Lett. **100**, 127002 (2008).

[188] S. Gerber *et al. Science* **350**, 949–952 (2015).

[189] E. M. Forgan, *et al.*, Nat. Comm. **6**, 10064 (2015).

[190] R. Comin *et al.*, Nat. Mater. **14**, 796–800 (2015).

[191] M. H. Hamidian *et al.*, Nat. Phys. **12**, 150-156 (2015).

[192] Haase, J., Sushkov, O. P., Horsch, P. & Williams, G. V. M., Phys. Rev. B **69**, 094504 (2004).

[193] M. Le Tacon *et al.*, *Nat. Phys.* **10**, 52–58 (2014).

[194] M.-H. Julien, Data for ortho-II YBCO in magnetic field $B = 12 - 15$T, *private communication.*

[195] R. Comin, *et al.*, Science **347**, 1335–1339 (2015).

[196] B. V. Fine, Science **351**, 235 (2016).

[197] R. Comin *et al.*, Science **351**, 236 (2016).

[198] Y. Wang and A. Chubukov, Phys. Rev. B **90**, 035149 (2014).

[199] P. A. Volkov and K. B. Efetov, Preprint at http://arxiv.org/abs/1511.01504v1 (2015).

[200] B. Renker, *et al.*, Phys. Rev. Lett., **30**, 1144 (1973).

[201] M. Johannes, & I. Mazin, Phys. Rev. B **77**, 165135 (2008).

[202] M. Hoesch, *et al.*, Phys. Rev. Lett. **102**, 086402 (2009).

[203] W. L. McMillan, Phys. Rev. B **12**, 1187-1196 (1975).

[204] L. Seabra, P. Sindzingre, T. Momoi, N. Shannon, Phys. Rev. B **9**3, 085132 (2016).

[205] A. Milstein and O. Sushkov, Phys. Rev. B **84**, 195138 (2011).

[206] R. Nath, A. A. Tsirlin, H. Rosner, and C. Geibel, Phys. Rev. B **78**, 064422 (2008).

[207] B. Dupé, G. Bihlmayer, M. Böttcher, S. Blügel and S. Heinze, Nature Communications **7**, 11779 (2016).

[208] L.D. Landau and E.M. Lifshitz, Phys. Z. Sowietunion **8** 153 (1953).

[209] L. Rózsa, A. Deák, E. Simon, R. Yanes, L. Udvardi, L. Szunyogh, and U. Nowak, Phys. Rev. Lett. 117, 157205 (2016).

[210] G.H. Derrick, J. Math. Phys. **5**, 1252 (1964).

[211] P. Day, A. Dinsdale, E.R. Krausz, and D.J. Robbins, J. Phys. C **9**, 2481 (1976).